This deliverable has not yet been externally reviewed and approved by the European Commission.

Project no.:	101095738		
Project full title:	6G SHort range extreme communication IN Entities		
Project Acronym:	6G-SHINE		
Project start date:	01/03/2023	Duration	30 months

D5.2 – FIRST IMPLEMENTATION AND EVALUATION OF POCS

Due date	31/12/2024	Delivery date	30/12/2024
Work package	WP5		
Responsible Author(s)	Hannes Ellinger (FHG)		
Contributor(s)	Wei Liu (IMEC), Spilios Giannoulis (IMEC), XianJun Jiao (IMEC), Hannes Ellinger (FHG), Jürgen Hupp (FHG), Oliver Haala (FHG), Usman Virk (Keysight Technologies), Timo Sarkkinen (Keysight Technologies), Pedro Maia de Sant Ana (Robert Bosch GmbH), Anastasios Grammenos (COGN), Christos Tsakos (COGN), Filipe Conceição (IDE), Sebastian Robitzsch (IDE)		
Version	V1.0		
Reviewer(s)	Baldomero Coll Perales (UMH), Gilberto Berardinelli (AAU)		
Dissemination level	Public		

Co-funded by the European Union

Horizon Europe Grant Agreement No. 101095738. Views and opinions expressed are however those of the author(s) only and do not necessarily reflect those of the European Union or SNS JU. Neither the European Union nor the granting authority can be held responsible for them.

VERSION AND AMENDMENT HISTORY

Version	Date (DD/MM/YYYY)	Created/Amended by	Changes
0.1	20/10/2024	Hannes Ellinger	TOC finalization
0.2	08/11/2024	Hannes Ellinger	Initial contributions from partners
0.3	15/11/2024	Hannes Ellinger	Editor revision and feedback
0.4	18/11/2024	Hannes Ellinger	Editor review done
0.5	29/11/2024	Hannes Ellinger	Refined contributions
0.6	06/12/2024	Hannes Ellinger	Final version ready for internal review
0.7	13/12/2024	Hannes Ellinger	Feedback from the internal reviewers
0.9	23/12/2024	Berit H. Christensen	Final proofreading and layout check
1.0	30/12/2024	Spilios Giannoulis	Submitted version

TABLE OF CONTENTS

FIGURES

TABLES

ABBREVIATIONS

Acronym	Description
AAL	Antenna array-like
AD	Analog devices
ADC	Analog-to-digital converter
AI	Artificial intelligence
ALLR	Approximated log likelihood ratio
AO	Alternate optimization
AP	Access point
BACKCOM	Backscatter communication
BCD	Block coordinate descent
BLER	Block Error Rate
BS	Base station
BW	Bandwidth
CCA	Clear Channel Assessment
CIR	Channel Impulse Response
CN	Core Network
COT	Channel Occupancy Time
CR	Constraint relaxation
CRC	Cyclic redundancy code
CSI	Channel state information
CSMA	Carrier Sense Multiple Access
CW	Continuous wave
DAC	Digital-to-analog converter
DC	Dual connectivity
DDC	Digital down-converter
DMA	Dynamic metasurface antenna
DSP	Digital signal processor
DUP	Digital up-converter
DUT	Device-under-test
EM	Electromagnetic
EPA	Equal Power Allocation
EQU	Equalization
ETSI	European Telecommunications Standards Institute
EW	Electronic warfare
FDMA	Frequency division multiple access
FPGA	Field programmable gate array
FSM	Finite State Machine
GCM	Geometric channel modelling
gNB	gNodeB
GNN	Graph Neural Network
HC	High Capability device

HW	Hardware
IEEE	Institute of Electrical and Electronics Engineers
IO	Indoor office
IOT	Internet-of-things
ISAC	Integrated Sensing and Communications
ISM	Industrial, Scientific and Medical
KKT	Karush-Kuhn-Tucker
KPI	Key Performance Indicator
LA	Latency Aware
LAD	Latency Aware Deconfliction
LBT	Listen Before Talk
LLC	Logical Link Control
LLR	Log-likelihood ratio
LOS	Line-of-sight
MAC	Medium Access control
MCS	Modulation and Coding Scheme
MIMO	Multiple-input multiple-output
MISO	Multiple input single output
ML	Machine learning
MLP	Multi-Layer Perceptron
MSE	Mean square error
NLOS	Non-line-of-sight
NOMA	Non orthogonal multiple access
OFDM	Orthogonal frequency division multiplexing
O-RAN	Open Radio Access Network
PDP	Power-delay profile
PDSCH	Physical Data Shared Channel
PER	Packet Error rate
PoC	Proof of Concept
PPS	Packets per second
QoS	Quality of Service
RF	Radio Frequency
RIS	Reconfigurable Intelligent Surface
RRM	Radio Resource Management
SDR	Software defined radio
SINR	Signal to Interference plus Noise Ratio
SISO	Single-input Single-output
SNC	Subnetwork Controller
SNE	Subnetwork element
SNR	Signal-to-noise ratio
SoTA	State of the art
SS	Synchronization Signal
SSB	Synchronization Signal Block

SW	Software
TC	Technology Component
TCF	Temporal correlation function
TDD	Time Division Duplex
TDMA	Time Division Multiple Access
UE	User Equipment
USRP	Universal Software Radio Peripheral
UWB	Ultra wideband
VNA	Vector network analyser

1 EXECUTIVE SUMMARY

The 6G-SHINE project addresses the challenges of next-generation short-range wireless communication and subnetworks by developing and validating innovative technology components (TCs) to enhance latency, reliability, and interference management. This deliverable highlights proof-of-concept (PoC) demonstrations that showcase advancements for industrial, vehicular, and consumer applications for subnetworks. Key innovations include low-latency channel emulation, latency-aware MAC mechanisms, jamming-resilient PHY layers, centralized radio resource management (RRM), jamming detection and avoidance and AI-driven distributed interference management.

These PoCs demonstrate significant improvements, such as reduced latency, enhanced coexistence in shared bands, robust performance under jamming conditions, and dynamic interference mitigation. Each PoC integrates with the broader 6G-SHINE framework, connecting to work packages focused on channel modelling, MAC design, and system-level optimization. By bridging theoretical models with real-world validation, the project demonstrates its solutions' feasibility and effectiveness.

This deliverable also maps results to relevant use cases, emphasizing their alignment with stringent industrial and vehicular requirements but also to consumer applications. Challenges encountered during implementation are critically analysed, with recommendations for refinement and extended applicability. The 6G-SHINE technologies outlined here offer a transformative approach to wireless communications, paving the way for next-generation connectivity solutions and future networks integration.

2 INTRODUCTION

The evolution of wireless communication technologies has steered unprecedented advancements in connectivity, enabling innovative applications across industrial, vehicular, and consumer domains. The 6G-SHINE project, designed to address the critical demands of emerging in-X subnetworks for short-range wireless communications, focuses on the development, demonstration, and evaluation of innovative technology components (TCs) to enhance performance in key areas such as latency, reliability, and interference management. This deliverable presents a comprehensive overview of the proof-of-concept (PoC) demonstrations that validate the technological advancements envisioned in the project, including initial performance results.

The integration of advanced wireless communication mechanisms is pivotal for addressing the unique challenges posed by next-generation applications. The PoC demonstrations detailed in this deliverable span across a wide range of technology components researched in this project, including low-latency channel emulation, latency-aware medium access control (MAC) mechanisms, jamming-resilient physical (PHY) layers, and centralized radio resource management (RRM). These initiatives align with the overarching goals of the 6G-SHINE project, which include achieving ultra-low latency, enhanced reliability, and seamless co-existence in shared spectrum environments.

Each PoC is designed with a focus on a specific technology component, validated through rigorous testing scenarios that emulate real-world operational environments. The demonstrations aim to provide tangible evidence of the feasibility and effectiveness of the proposed solutions, showcasing measurable improvements in critical performance indicators such as latency, throughput, power-delay profiles, and robustness against interference.

This deliverable is structured to offer insights into the connection of these TCs with the larger framework of work packages WP2, WP3, and WP4, which focus on channel modelling, PHY and MAC design, and system-level optimization, respectively. By synthesizing theoretical models, simulation results, and real-world validations, the 6G-SHINE project bridges the gap between conceptual innovation and practical deployment.

The key highlights of the deliverable include:

1. **Low Latency Channel Emulator (Keysight):** Validates channel modelling for vehicular, industrial, and consumer applications, achieving a significant reduction in the latency of their PROPSIM channel emulator.
2. **Latency-Aware MAC (IMEC):** Demonstrates improved coexistence in shared bands, offering deterministic medium access for latency-sensitive applications.
3. **Jamming-Resilient PHY (IMEC):** Enhances receiver sensitivity to maintain robust performance under wideband jamming conditions.
4. **Intra-subnetwork macro-diversity (FHG):** Leverages network coding and cooperative mechanisms to improve reliability and latency in industrial subnetworks.
5. **Centralized RRM (Bosch):** Introduces dynamic resource allocation mechanisms for interference mitigation in vehicular and industrial environments.
6. **Distributed Interference Management (COGN):** Explores AI-driven, decentralized techniques to optimize transmission power and channel usage in overlapping subnetworks.
7. **Jamming Detection Using Anomaly Detection Methods (IDE):** Diving into anomaly detection solutions that can support recognition, and therefore trigger triggering mitigation techniques, of malicious jammers in the domain of subnetworks.

This deliverable also maps the achieved results to relevant use cases identified in WP2, highlighting how the proposed solutions align with or exceed the stringent requirements of industrial, consumer and vehicular applications. Furthermore, challenges encountered during the PoC implementations are critically analysed, with recommendations for future improvements to refine the solutions and extend their applicability.

In the following sections, a detailed description of each PoC, including its architecture, functionality, demonstration scenarios, and initiative quantitative results, is presented. These insights underscore the potential of the 6G-SHINE technologies to revolutionize wireless communication paradigms and provide a roadmap for further research and development in the field.

This is the second deliverable of WP5, aiming to present the initial implementation details and evaluate performance gains from the proposed technology components. A third and final deliverable will present the final PoC results.

3 WP5 CONNECTION WITH WP2-3-4

The main objective of WP5 in 6G-SHINE is to implement and evaluate selected relevant TCs defined in the project on software and/or hardware platforms. The TCs are developed in the work packages 2, 3, and 4. WP2 delivers scenarios, use cases and requirements. PHY layer and MAC layer enablers are developed in WP3. WP4 examines radio resource and operation management techniques. The results of WP5 shall also provide feedback for the WP2-3-5 development process, in the form of real performance gains able to be delivered with today's SW/HW available components while also pinpoint implementation hurdles that could limit the feasibility of realisation of systems supporting the proposed TCs. Table 1 lists the relevant TCs with their appropriate WP that will be implemented as a PoC in WP5, as it has been decided so far within the project.

TABLE 1. LIST OF 6G-SHINE POCS.

#	Lead partner	Title	TC	WP
1	Keysight	Low latency channel emulator	TC2	WP2
2	IMEC	Latency Aware MAC access	TC11	WP3
3	IMEC	Jamming resilient PHY	TC6	WP3
4	FHG	Intra-Subnetworks macro-diversity	TC8	WP3
5	Bosch	Centralized RRM	TC13	WP4
6	COGN	Centralized/Distributed interference management	TC12, TC13	WP4
7	IDE	Jamming detection using Anomaly detection methods	TC15	WP4

4 PROOF OF CONCEPT PRESENTATION

The seven PoC being developed by the project partners are presented in this section, along with their early results.

4.1 LOW LATENCY CHANNEL EMULATOR

4.1.1 GENERAL DESCRIPTION

Wireless communication systems face significant challenges due to propagation effects such as attenuation, shadowing, fast fading, variable delays, Doppler effects, noise, and interference, which degrade transmission quality. Traditional field-testing of these systems is labour-intensive, time-consuming, expensive, and often yields non-repeatable results due to environmental uncertainties. To address these issues, radio channel emulators have become essential for rigorous, repeatable, and cost-effective testing in controlled laboratory environments.

This PoC focuses on the low-latency emulation of channel models for short-range communication links developed in WP2. These models cater to vehicular, industrial, and consumer use cases. Leveraging Keysight's PROPSIM radio channel emulator, the PoC replicates real-world wireless channel effects, including multipath propagation, fast fading, delays, noise, and interference. PROPSIM supports diverse wireless standards and applications such as beamforming, massive MIMO, software-defined radio (SDR), and aerospace communication.

PROPSIM is independent of transmitter and receiver technologies and provides a flexible, file-based emulation approach ensuring repeatability. Users can create or modify channel models using built-in tools, and the platform supports up to 128 fading channels for complex test scenarios. Its intuitive GUI minimizes manual setup effort, making it accessible for both basic and advanced use.

As part of the 6G SHINE project, Keysight aims to enhance PROPSIM's latency performance to support in-X subnetwork short-range communication models. This work aligns with the radio channel characterization and modelling efforts outlined in WP2 Task 2.2a and Task 2.2b, facilitating robust testing and validation of emerging 6G applications under stringent latency requirements. In the previous deliverable 5.1, we presented a comprehensive plan outlining the initial implementation and evaluation criteria for the low-latency channel emulation PoC. This deliverable focuses on the actual implementation and validation of the PoC, following the plan established in the previous deliverable.

A radio channel emulator simulates real-world physical distances between a transmitter and receiver by introducing corresponding propagation delays. For example, a 1 µs delay represents 300 m distance, while a 10 µs delay equates to 3 km distance in free space. Propagation delays are typically implemented using pipeline registers or memory for longer delays. As modern wireless systems adopt smaller cell sizes and higher RF frequencies, communication ranges are shrinking, with some systems, such as the ones under investigation in 6G-SHINE, supporting only very short ranges. This trend demands extremely low minimum propagation delays in channel emulators. If the minimum delay is too long, time synchronization can fail, rendering the emulator unsuitable for such applications. Thus, minimizing emulator latency is critical for supporting current and future wireless technologies.

FIGURE 1. TYPICAL CHANNEL EMULATION SETUP FOR PERFORMANCE TESTING OF DEVICES.

4.1.2 ENHANCED FUNCTIONALITY

Before the optimization effort prior to the 6G-SHINE project, the PROPSIM channel emulator platform had an insertion delay of approximately 2.2 microseconds. This latency specs do not fully align with the requirements of the in-X subnetworks outlined in the 6G-SHINE project. The goal for this phase was to reduce the latency to ~ 1.0 microseconds in the initial proof-of-concept (PoC). In the subsequent phase, the target is to achieve a latency of ~ 0.5 microseconds for the final PoC demonstration. However, reaching this target is contingent upon the availability of required hardware components, which could potentially delay the final implementation.

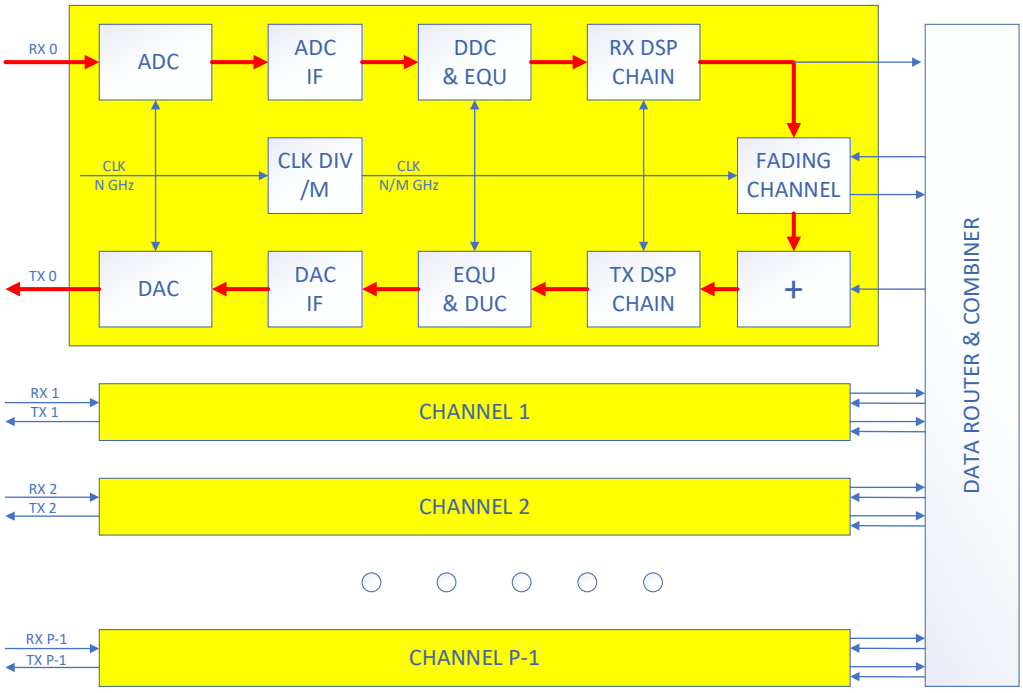

FIGURE 2. BASEBAND ARCHITECTURE OF RADIO CHANNEL EMULATOR

The architecture of a radio channel emulator is shown in Figure 2. It includes an RF front end, ADC/DAC, baseband DSP, and routing and combining blocks. Signals traverse all these blocks, with the majority of the latency arising

from the ADC/DAC and baseband DSP, which can introduce delays in the microsecond range without optimizations. Consequently, the work in WP5 focuses on reducing the latency of these components. The RF front end has a negligible delay, typically in the nanosecond range, and is not a target for optimization. The routing and combining block, responsible for multi-channel signal management, adds a typical delay of several hundred nanoseconds. Efforts to minimize the latency of critical components will ensure compatibility with evolving wireless communication requirements.

Latency optimization in a radio channel emulator involves improving the performance of all functional blocks in the system (see Figure 2). While some optimizations are straightforward and can be achieved without hardware modifications, others may require significant changes in hardware, system architecture, or component configurations. The optimization tasks are divided into the following five key categories. However, items 3–5 fall outside the scope of this deliverable and are planned for the next phase, specifically in D5.3, which involves complex architectural and hardware level changes. The latency optimization conducted as part of D5.2, and detailed in this deliverable, is focused exclusively on items 1 and 2.

1. **Modifications in component settings**: Adjusting component settings is the simplest optimization method, requiring no changes to hardware. However, care must be taken to ensure that the settings do not introduce unnecessary delays. Non-optimal configurations, such as inappropriate clock rates or buffering policies, can add unwanted latency. Special attention to these settings ensures baseline improvements with minimal effort.
2. **Modifications in programmable Logic (FPGA/SoC)**: The majority of digital signal processing (DSP) in the emulator is implemented within the FPGA block, as illustrated in Figure 2. This makes programmable logic an ideal area for latency reduction through software-level adjustments. Changes in FPGA code, such as optimizing the Digital Down Converter (DDC), Equalization (EQU), Digital Up Converter (DUC), or fading channel modules, can yield significant latency reductions without altering the physical hardware. This flexibility in programmable logic allows rapid iteration and implementation of enhancements.
3. **Component changes**: Swapping existing components for faster, pin-to-pin-compatible alternatives can improve performance but may also necessitate hardware adjustments. For example, upgrading the ADC/DAC to devices with lower conversion times or improved interfaces can reduce overall system latency. This approach, while effective, involves more complexity than adjustments limited to programmable logic.
4. **Hardware modifications**: Hardware redesigns provide opportunities to incorporate advanced components, reduce signal routing complexity, and introduce new high-performance interfaces. For instance, modifying the ADC/DAC interface blocks or replacing outdated routing buses in critical paths can eliminate significant bottlenecks. These changes, while impactful, are complex and prone to errors, requiring detailed validation to ensure system stability and compatibility.
5. **System architecture modifications**: Overhauling the system architecture is essential to achieve optimal latency. This involves rethinking the data flow, reducing the number of buses in the critical path, and taking full advantage of modern programmable logic devices (e.g., FPGAs). For example, the architecture in Figure 2 highlights areas like the RX DSP chain, TX DSP chain, and data router/combiner, where architectural changes could streamline signal processing and minimize delay.

In this deliverable, latency improvements were focused on the modifications to FPGA and software. These changes target the programmable logic blocks, such as the DDC/EQU, fading channel, and DSP chains, without requiring any hardware modifications. This phase ensures quick wins and immediate enhancements with relatively low effort and risk.

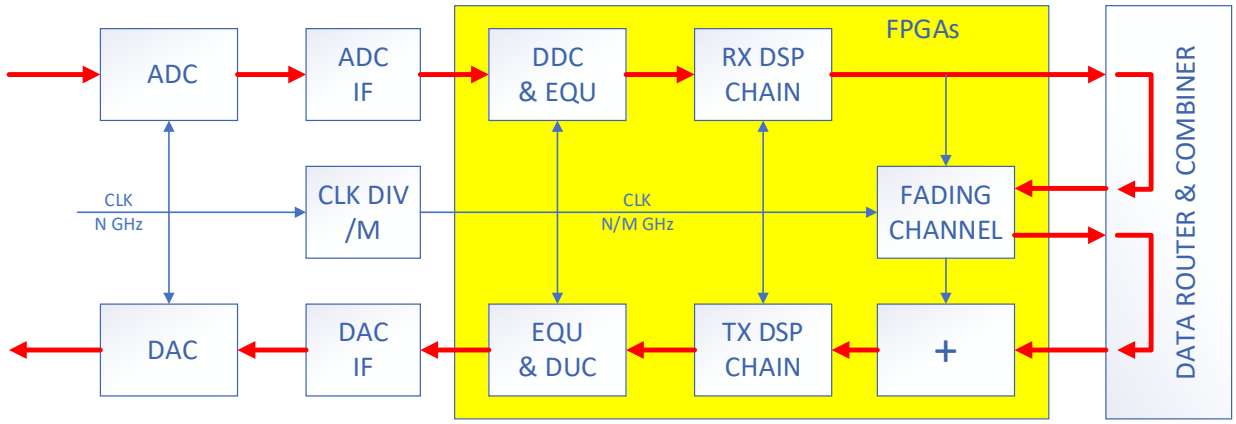

FIGURE 3. HIGH-LEVEL OPTIMIZED ARCHITECTURE OF THE CHANNEL EMULATOR

Figure 3 provides a detailed view of the high-level optimized architecture of the emulator, showing the signal flow through various functional blocks:

- The **ADC/DAC blocks** handle ADC and DAC conversion, which can contribute to latency depending on the conversion speed.
- The **FPGA section** includes the RX and TX DSP chains, fading channel, and EQU/DDC blocks, which are the main focus of FPGA-level optimizations.
- The **Data Router & Combiner block** manages the final signal routing, with a latency of a few hundred microseconds. Further reduction in latency is possible only through hardware and architectural redesigns.

Through these optimization steps, the goal is to achieve the target latency of ~ 1 microsecond while ensuring the emulator remains versatile and compatible with modern and future wireless communication systems. This structured approach balances quick improvements without long-term architectural enhancements, ensuring both immediate impact and sustained performance gains. The long-term architecture-based optimization is planned in the next phase of the project.

4.1.3 HIGH-LEVEL ARCHITECTURE OF THE IMPLEMENTED POC DEMONSTRATOR

To demonstrate TC2 using the PoC demo low-latency channel emulator platform, the following KPIs are critical for validating performance and ensuring the platform meets low-latency requirements. Quantitative comparisons between measured and reference results will determine if the PoC delivers the expected outcomes.

4.1.3.1 KEY PERFORMANCE INDICATORS (KPIS)

1. **Insertion delay:** Insertion delay represents the time taken for the RF signal to travel from the input port to the output port of the emulator device. It quantifies the electrical delay added by the emulator, contributing to overall system latency.
2. **Power-delay profile (PDP):** PDP describes the average received power as a function of delay, showcasing the power decay of multipath components over time. It is calculated by spatially averaging the squared magnitude of the channel impulse response across multiple observations.
3. **Doppler spectrum:** Doppler spectrum reflects frequency shifts caused by user movement, resulting in uncorrelated fading between multiple received signal paths.
4. **Temporal correlation function (TCF):** TCF measures how quickly the channel changes over time, offering insights into channel stability.

These KPIs collectively validate the emulator's capability to meet low latency demands while accurately simulating real-world wireless conditions.

The PoC testbed is divided into two parts to validate the targeted KPIs, as outlined below:

4.1.3.2 INSERTION DELAY AND POWER DELAY PROFILE (PDP) VALIDATION

The performance of the Keysight PROPSIM channel emulator is benchmarked in terms of insertion delay and PDP in this validation. The standard procedure for measuring insertion delay, applicable to any device under test (DUT), is employed. The test setup for validating these parameters is depicted in Figure 4.

Keysight PNA-X is used to measure the S21 parameter of the Keysight PROPSIM channel emulator, which represents the ratio of output to input voltage across a range of frequencies. The PNA-X captures both the magnitude and phase of the signal. For devices with non-zero electrical delay, the phase shift between input and output varies with signal frequency. Lower-frequency signals, having longer wavelengths, exhibit fewer phase cycles through the DUT compared to higher-frequency signals. The phase component of the S21 trace is analysed to calculate the electrical delay. Using an "unwrapped" phase format, the PNA-X displays phase trends that extend beyond ±180 degrees. This approach preserves long phase shifts, enabling precise measurement of insertion delay caused by the DUT. This methodology ensures accurate benchmarking of the PROPSIM's insertion delay and PDP performance, which are critical KPIs for low-latency channel emulation platforms.

FIGURE 4. MEASUREMENT SETUP FOR VALIDATING INSERTION DELAY AND POWER DELAY PROFILE (PDP).

The PDP is also measured using the S21 traces obtained from the Keysight PNA-X. This process involves loading and emulating the channel model in the Keysight PROPSIM channel emulator. The Keysight PNA-X records the frequency responses, $H(t, f)$, which are saved for post-processing and analysis using software such as MATLAB. The PDP measurement workflow is as follows:

1. **Frequency response capture**: The Keysight PNA-X transmits frequency sweep signals through the system under test. Multiple frequency response traces $H(t, f)$ are measured and saved for analysis.
2. **Post-processing in MATLAB**:
    - Each frequency response trace is processed using a Fourier Transform to calculate the corresponding impulse response $h(t, f)$.
    - The power of each impulse response is averaged over time, as defined by:

$$P(\tau) = \frac{1}{T}\sum_{t=1}^{T}|h(t,\tau)|^2$$

    - The resulting PDP is adjusted in delay so that the first tap aligns with zero delay.

3. **Measurement setup**: The setup for PDP measurements, shown in Figure 4, ensures accurate frequency response recordings. During these measurements, fading conditions in the emulator are kept "frozen" to maintain consistency. Fading is allowed to proceed only between measurement traces to avoid discrepancies.
4. **Parameter settings**: Measurement settings, including the specific parameters for the channel model and VNA configurations, are detailed in Table 2. These settings ensure the accuracy and repeatability of the PDP evaluation.

TABLE 2. KEYSIGHT PNA-X PARAMETERS SETTINGS.

Item	Unit	Value
Center frequency	MHz	11000
Span	MHz	200
Number of traces	MHz	1000
Number of points		1601
Averaging		10

This method validates the PDP performance of the Keysight PROPSIM channel emulator by comparing the measured results to the loaded channel model. The process highlights the emulator's capability to accurately reproduce predefined channel conditions while maintaining low-latency performance.

4.1.3.3 DOPPLER SPECTRUM AND TEMPORAL CORRELATION FUNCTION (TCF) VALIDATION

The second part of the PoC demonstration focuses on measuring the Doppler spectrum and temporal correlation of the in-X subnetwork channel emulation in PROPSIM. The setup, illustrated in Figure 5, uses a Keysight Signal Generator or Keysight PNA-X to transmit a continuous wave (CW) signal to the PROPSIM emulator, which processes and outputs the signal. The output is then analysed using the Keysight UXA signal analyser, and the measured spectrum is compared to the target spectrum.

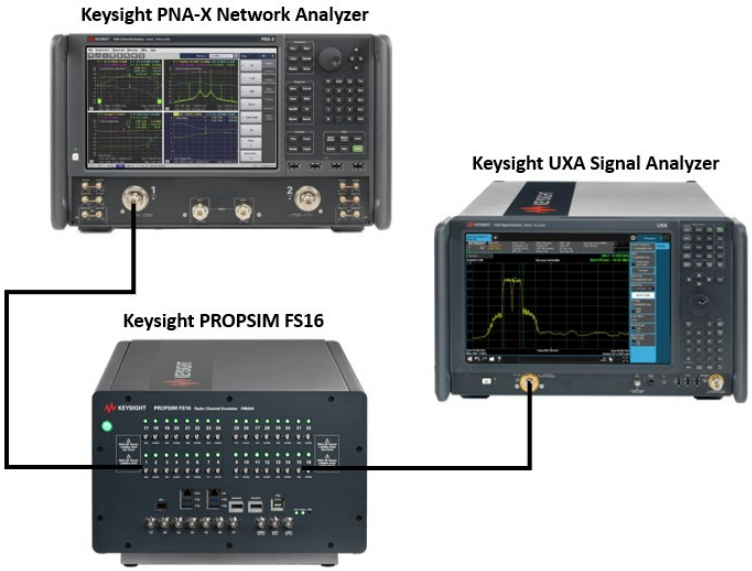

FIGURE 5. MEASUREMENT SETUP FOR VALIDATING DOPPLER SPECTRUM AND TEMPORAL CORRELATION.

The Doppler power spectrum data is saved and further processed in MATLAB. The analysis includes performing a Fourier transformation to obtain the temporal correlation function, which is then normalized. Irrelevant values, such as those beyond the maximum and after a specified number of periods (e.g., seven), are removed to finalize the results. Parameter settings for the Keysight UXA are detailed in Table 3. This streamlined process ensures accurate validation of the Doppler spectrum and temporal correlation.

TABLE 3. KEYSIGHT UXA PARAMETERS SETTINGS.

Item	Unit	Value
Center frequency	MHz	11000
Minimum Span	KHz	4
RBW	Hz	1
VBW	Hz	1
Number of points		160002
Averaging		100

4.1.4 DEMONSTRATOR SCENARIO

The demonstration scenario is related to the channel model derived for an industrial lab environment depicted in Figure 6. The large-scale propagation channel parameters (LSPs), including PDP, K-factor, and pathloss, derived from the FR3 measurements in WP2 Task2.2b, were combined with the spatial parameters of the indoor factory dense clutter (InF-DL) channel model from for the specified link geometries (i.e., The large-scale propagation channel parameters (LSPs), including PDP, K-factor, and pathloss, derived from the FR3 measurements in WP2 Task2.2b, were combined with the spatial parameters of the indoor factory dense clutter (InF-DL) channel model from [26] for the specified link geometries (i.e., TX-RX locations). These parameters were applied to the TX-RX trajectory transitioning from LOS to NLOS conditions, as shown in Figure 7, using the Keysight Channel Studio Geometric Channel Modelling (GCM) tool, as shown in Figure 7. This process generated a spatially consistent, time-continuous dynamic channel model following the implementation methodology in [26].

FIGURE 6. SMART PRODUCTION LAB – INDUSTRIAL ENVIRONMENT MEASUREMENTS AT AALBORG UNIVERSITY

The resulting channel model was emulated on the Keysight FR3 low-latency PROPSIM channel emulator. Key channel characteristics, such as the PDP and Doppler spectrum, were validated using the Keysight PNA-X Network Analyzer and Keysight UXA Signal Analyzer according to the validation setups described in Figure 8.

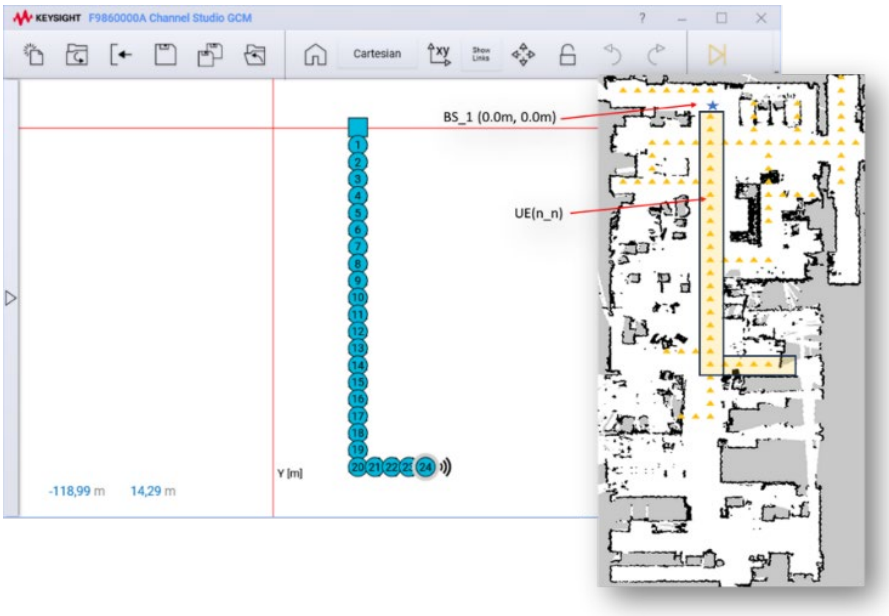

FIGURE 7. CHANNEL MODEL IMPLEMENTATION IN F9860000A KEYSIGHT CHANNEL STUDIO GCM.

4.1.5 RESULTS

The PoC demonstrator setup for validating the key KPIs is shown in Figure 8 and has been described in detail in the preceding Section 4.1.3. It includes the RF connectivity between the Keysight PROPSIM channel emulator and measurement equipment, i.e., Keysight PNA-X and Keysight UXA Signal Analyzer.

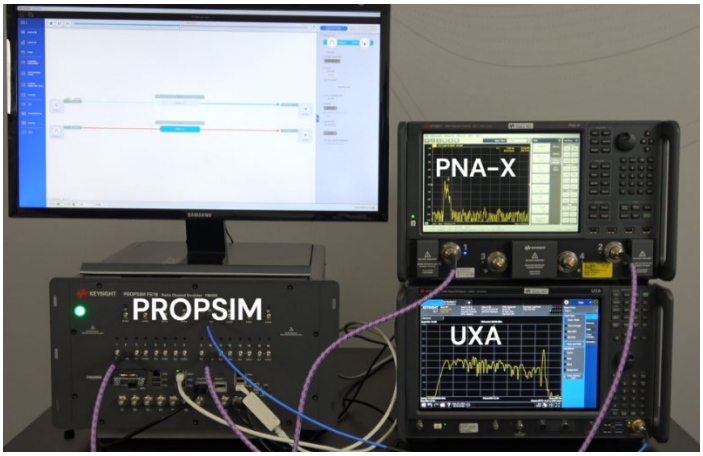

FIGURE 8. EMULATING IMPLEMENTED CHANNEL MODEL WITH KEYSIGHT LOW-LATENCY F8820B PROPSIM CHANNEL EMULATOR AND VALIDATING MODEL CHARACTERISTICS WITH KEYSIGHT N5247B PNA AND N5247B UXA.

FIGURE 9. INSERTION DELAY MEASUREMENTS FOR THE IMPLEMENTED CHANNEL MODEL

Figure 9 presents the insertion delay measurements for the Keysight PROPSIM channel emulator on Keysight PNA-X through S21 measurements and displays the time-domain channel impulse response (CIR) utilizing the time-domain transformation feature of the Keysight PNA-X. It demonstrates the achievement of the target latency where the insertion delay of ~0.9 microseconds are observed.

The validation results for PDP and Temporal Autocorrelation Function are illustrated in Figure 11 to Figure 13 where the measured and modelled characteristics perfectly match. This demonstrates the measurement and modelling accuracy of the Keysight software and hardware. The Doppler spectrum for the derived channel model over the UE route is also shown in Figure 13.

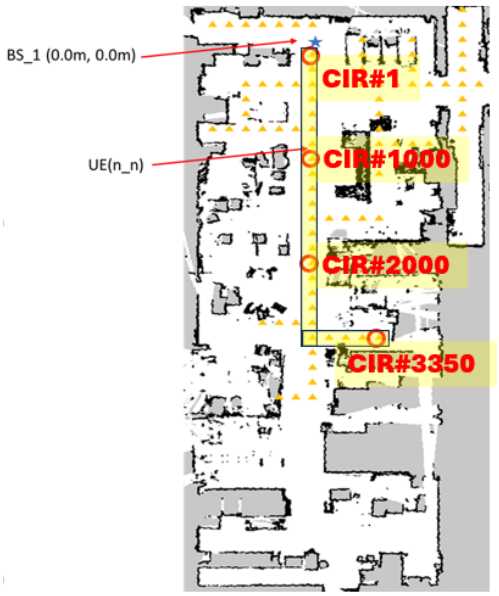

FIGURE 10. RX/UE ROUTE IN THE INDUSTRIAL LAB ENVIRONMENT AND SELECTED POSITIONS FOR PDP VALIDATION

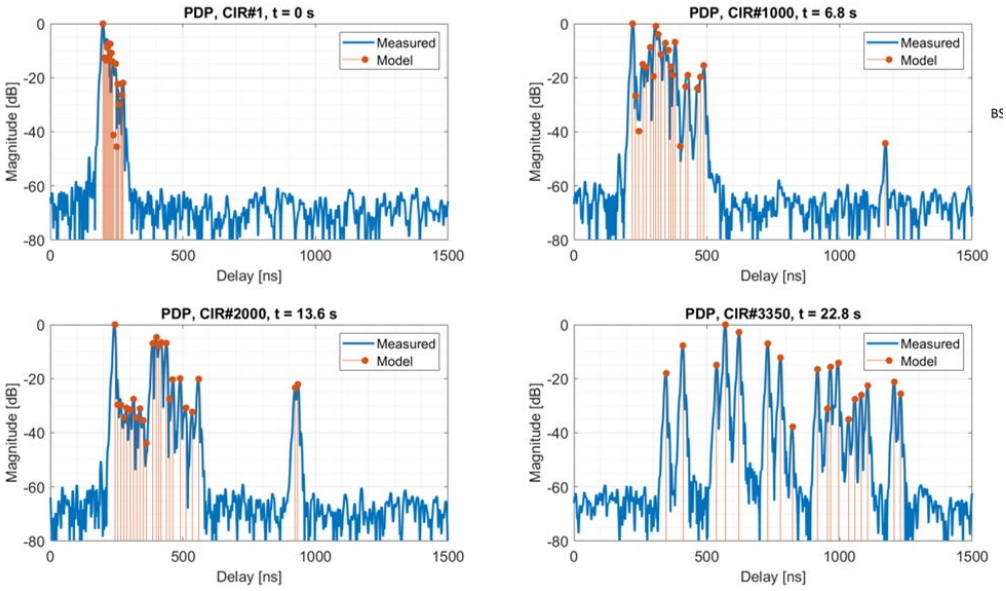

FIGURE 11. POWER-DELAY PROFILE (PDP) VALIDATION RESULTS FOR THE SELECTED POSITIONS OVER THE RX/UE ROUTE

Figure 10 illustrates the measurement scenario, where the RX/UE follows a defined trajectory transitioning from Line-of-Sight (LOS) to Non-Line-of-Sight (NLOS) conditions. The selected exemplary Channel Impulse Response (CIR) points, namely CIR#1, CIR#1000, CIR#2000, and CIR#3350, are highlighted along the route to represent significant channel characteristics at different time intervals and positions. Figure 11 presents the measured and modelled Power PDPs. The measured PDPs, represented by blue lines, capture the multipath delay structure at each CIR point, with distinct peaks corresponding to major multipath components. The modelled PDPs, indicated by orange markers, align closely with the measured data, particularly in LOS conditions, but show slight deviations in magnitude or position for weaker components, especially in NLOS scenarios.

In terms of delay spread, the progression from CIR#1 to CIR#3350 shows an increase as the RX transitions from LOS to NLOS. This reflects the growing complexity of the propagation environment, with CIR#3350 exhibiting a broader range of delays compared to CIR#1. The modelled PDPs accurately capture the power levels of dominant multipath components. The LOS scenario (CIR#1) demonstrates a close match between the model and measured data, while deviations are more pronounced in NLOS conditions, where the multipath structure becomes more diffuse. Overall, the model shows strong qualitative and quantitative agreement with the measured data. It is highly accurate in LOS scenarios and retains acceptable performance in NLOS conditions, successfully capturing the key trends and characteristics of the propagation environment. These results validate the channel model's capability to emulate realistic propagation conditions across both LOS and NLOS scenarios.

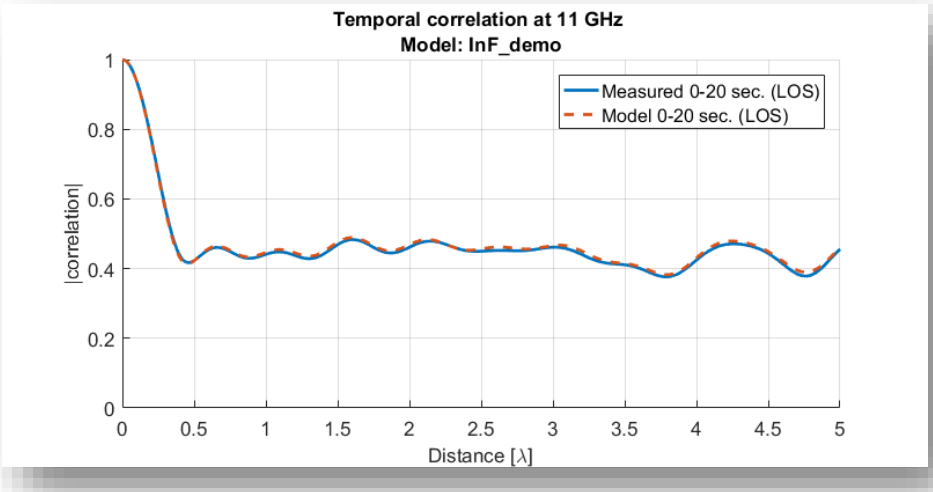

FIGURE 12. MODEL AND MEASURED TEMPORAL AUTOCORRELATION FUNCTION (TCF) FOR THE IMPLEMENTED CHANNEL MODEL OVER THE RX/UE ROUTE.

Figure 12 illustrates the temporal correlation at 11 GHz for the indoor factory dense clutter (InF) channel model LOS conditions. It compares the measured temporal correlation (solid blue line) with the modelled temporal correlation (dashed orange line) across a distance range normalized to the wavelength (λ). A rapid decline occurs within the first 0.5λ, reflecting the natural decorrelation of the signal over short distances due to changes in multipath components.

Beyond 0.5λ, the temporal correlation stabilizes, fluctuating around a mean value of approximately 0.4 to 0.6. These fluctuations are consistent with the multipath propagation characteristics in an LOS environment, where reflected and scattered components contribute to the observed correlation pattern. The modelled correlation closely matches the measured data, effectively capturing both the rapid initial decorrelation and the stable behaviour at longer distances. Overall, the figure confirms the accuracy of the InF channel model in replicating temporal correlation characteristics at 11 GHz for LOS scenarios.

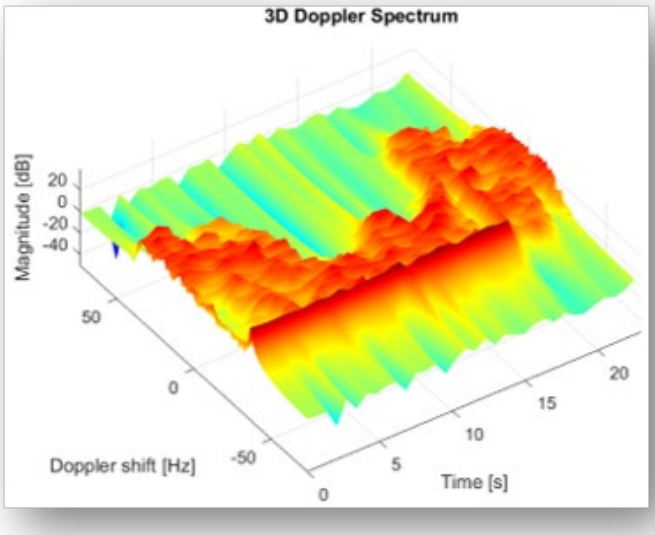

FIGURE 13. MEASURED DOPPLER SPECTRUM FOR THE IMPLEMENTED CHANNEL MODEL OVER THE RX/UE ROUTE.

Figure 13 depicts a 3D Doppler spectrum, illustrating the variation in signal magnitude (in dB) as a function of Doppler shift (Hz) and time (s). The spectrum reveals the dynamic nature of the channel, with strong signal components concentrated near zero Doppler shift until about 20 sec when LOS still exists. The broader spread of energy at higher Doppler shifts after 20 sec without the presence of a dominant LOS component corresponds to the NLOS.

4.1.5.1 CONCLUSION

This work demonstrates the critical role of low-latency channel emulation in addressing the stringent requirements of modern wireless communication systems, particularly for 6G applications. The PoC implementation on the Keysight PROPSIM channel emulator successfully achieves significant latency reductions, meeting the initial target of ~1 microsecond and showcasing its capability to emulate real-world propagation effects with high accuracy and repeatability. Key performance indicators such as insertion delay, PDP, Doppler spectrum, and TCF validate the emulator's ability to replicate complex channel conditions for both LOS and NLOS scenarios.

The results underscore the feasibility of integrating latency-optimized emulators into advanced wireless system testing frameworks, providing a robust platform for evaluating emerging technologies in vehicular, industrial, and consumer domains. The planned architectural and hardware-level optimizations in future project phases aim to further enhance the emulator's performance, supporting the development and validation of next-generation wireless networks. Additionally, the next phase of the PoC will incorporate channel emulation capabilities for Reconfigurable Intelligent Surfaces (RIS), enabling the channel emulator to simulate advanced propagation scenarios and further expand its versatility for next-generation wireless communication systems.

4.2 LATENCY AWARE MAC

4.2.1 GENERAL DESCRIPTION

The proposed LAD MAC scheme in WP3 is aiming to be an enabler for latency sensitive networking in situations where multiple technologies are present in the same spectrum, for example in ISM bands. As 6G is aiming to use multiple spectrum bands, the ability to coexist in shared bands with other technologies and harness capacity, without the disadvantage of deteriorating QoS because of the shared nature of these bands, is very interesting and the impact of such a solution can be very high. In the case of subnetworks specifically, the use of shared spectrum bands can provide significant capacity that could be used to maximize offered QoS and minimize latency specifically.

In deliverable D5.1 a general description and high-level architecture was presented, along with the overall framework that would allow for performance comparison. In the following subchapters the implementation of the proof of concept of the latency aware LAD MAC and the performance results acquired from testing under relevant conditions is presented.

4.2.2 ENHANCED/NEW FUNCTIONALITY

The implemented demonstrator is able to present the ability of the proposed LAD technology component to offer stable QoS communication over shared bands, not being impacted from the presence of other wireless technologies that also use the same spectrum resources.

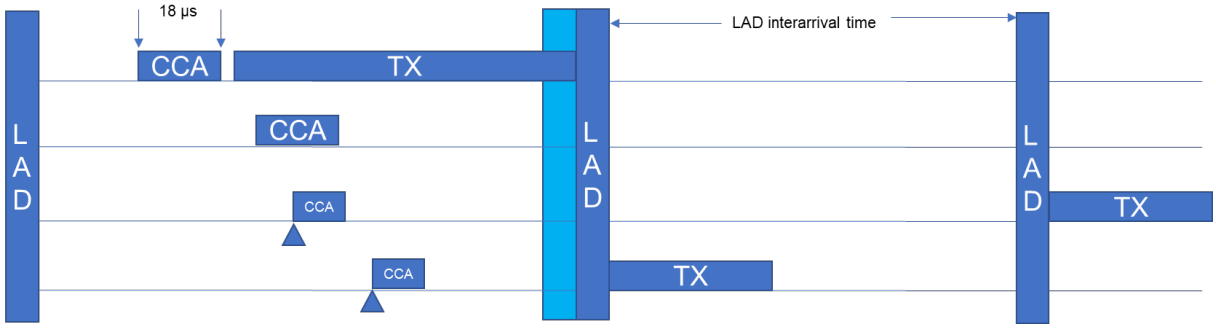

FIGURE 14. LATENCY AWARE DECONFLICTION PERIOD STRUCTURE AND TIMINGS

The proposed MAC scheme introduces a periodical unsynchronized session that will be used strictly for high priority traffic. In that sense, a subnetwork could utilize this MAC access scheme to access ISM bands and harvest capacity but still be able to keep very high QoS. This is possible based on the design of the LAD access scheme, specifically being able to take access of the medium with smaller basic CCA times vs what is used today based on the ETSI related standards [2]. For instance, in Figure 14 we can see what is enforced for 2.4 GHz ISM band; each node trying to get access to the medium needs to do carrier sensing for at least 18 µs before starting to transmit in any case. CSMA variants and all other MAC protocols used in ISM bands build on top of this basic access requirement. LAD period comes into play and grants access to LAD enabled nodes without harming other active transmissions. As an example, the second LAD period in Figure 14 slides in time until the active transmission is finished before trying to get access to the medium. Due to the design and hard priority access of LAD based on the smaller CCA times used for LAD access, it will surely take hold of the medium before any other ETSI compliant MAC protocol does so, hence proving that hard priority-based access to the medium is possible if multiple duration of CCA is allowed/foreseen from the relevant ETSI standards. Once the LAD TX finished, then any other technology can take hold of the medium and transmit its traffic as well. For more details on the proposed LAD MAC technology component and its design we kindly refer you to WP3 related D3.1 deliverable [3] where the proposed scheme is analysed in detail and its performance evaluated in small, medium and large density and scale deployments using NS3 simulation tool [4] .

As it has been seen already in WP3 theoretical and simulated results for the proposed LAD TC, it is possible to offer significantly lower MAC access delay and as a result also lower Application layer end-to-end latency, especially in high density topologies were more than 16 or even 32 nodes are present in the same collision domain. The

implemented PoC aims to verify and complement the theoretical results and show what is possible today with currently available HW and SW platforms, but also to pinpoint what needs to be further enhanced such that the proposed TC can show its true potential and offer significant QoS enhancements.

4.2.3 HIGH LEVEL ARCHITECTURE OF THE IMPLEMENTED POC DEMONSTRATOR

The architecture of the implemented demonstrator is show in Figure 15. It is comprised of 2 LAD enabled devices that are based on a ZYNQ platform from AMD/Xilinx, namely the ZCU-102 development kit [1] equipped with Analog Devices FMCOMMS 2 RF frontend card [6], and 4 Intel NUC devices equipped with AX-200 Wi-Fi cards [7] that act as the ISM incumbent technology that compete with the proposed LAD equipped devices for access in the same channel. The components of the demonstrator can be seen in Figure 16.

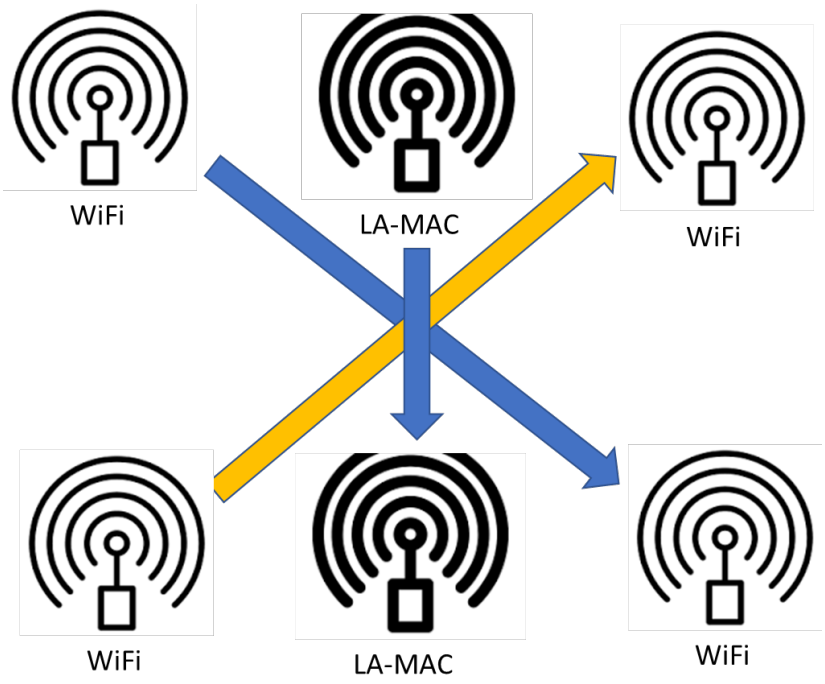

FIGURE 15. LAD-MAC DEMONSTRATOR TOPOLOGY AND STRUCTURE

All 6 nodes are placed close to each other in order to all reside in the same wireless collision domain. The transmission power of all wireless nodes is calibrated to deliver equal transmission power and avoid any PHY dominance effect where even packets colliding with other packets can still be decoded from their respective receivers. Using the implemented topology, traffic flows are pushed through the active links and measurements based on Application and MAC layer KPIs are taken to determine the performance of the proposed LAD MAC but also its impact on incumbent technologies.

FIGURE 16. XILINX ZCU-102 DL AND INTEL NUC MINI PC

On top of the hardware infrastructure deployed, a software traffic flow generator is used to generate IP traffic as application layer traffic in order to be able to measure relevant KPIs on an end-to-end basis, namely KPIs like end-to-end latency, packet success ratio, packet interarrival time and throughput. The traffic generator used is called MGEN and more details can be found in the relevant reference [8].

Overall, the implemented prototype architecture allowed us to test the proposed LAD MAC against a typical shared access SoTA CSMA based MAC employed in ISM bands using off-the-self devices and compare performance between the two in varied network load conditions. More technical details on the setup of the demonstrator and the relevant software and traffic flows employed can be found in the section below.

4.2.4 DEMONSTRATOR SCENARIO DESCRIPTION

The technical setup of the demonstrator, each wireless technology as well as the demonstration typical scenario are presented here in detail.

Starting by the LAD hosting HW/SW platform, the implementation is based on the openwifi system [9] , where we have stripped the CSMA based MAC and added the implementation of the proposed LAD MAC. The employed PHY layer waveform is OFDM, and the channel width is 10 MHz. A 20 MHz channel was not possible to be used due to limitations of the baseband implementation in our platform. This is planned to be supported in the next iteration of this proof of concept. We also chose to fix the MCS to MCS3 to avoid any MCS adaptation algorithm that could impact the available capacity of the PHY layer, as our task is mainly to measure MAC performance under static PHY settings. With the mentioned PHY settings the available raw PHY capacity in the LAD platform was 9 Mbps.

A new Finite State Machine (FSM) was implemented in FPGA for the support of the new LAD scheme, as a software solution on the driver would not be possible to achieve the µs accuracy needed for the LAD MAC to function properly and do CCA in the wireless medium. The complete FSM of the transmit chain is shown in Figure 17.

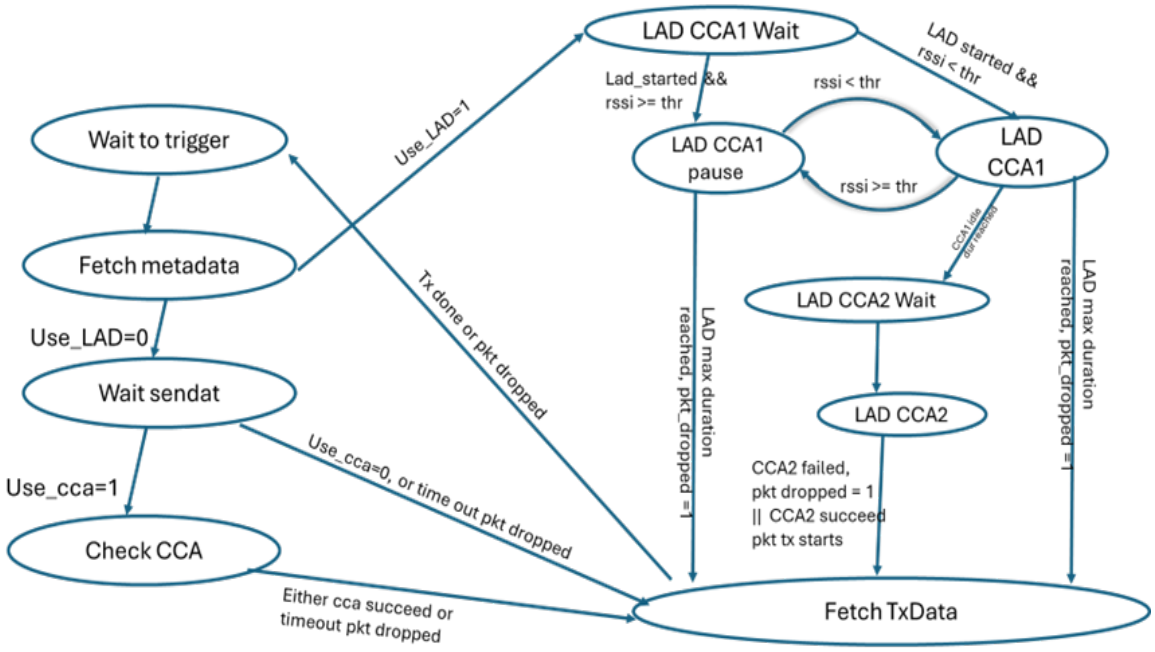

FIGURE 17. LAD FSM ON THE TRANSMITTER

As it can be seen, the altered FSM is adding a new way to transmit a packet opposed to the old CCA based approach. Now if the flag *Use_LAD* signal is set to ON, the packet will be transmitted only if the LAD logic allows it following the defined LAD access scheme presented in detail in D3.1 [3]. We will not go into a detailed presentation of the LAD mechanisms here, but we do refer the reader to the D3.1 and upcoming D3.3 for more information on the LAD design.

In order to verify the function of the FSM, we have inserted a logical analyser in the FPGA, through which we are able to visualize the real-time value of the measured RSSI as well as the state of the FSM. For example, we wanted to check if the LAD CCA1 wait period for free channel would indeed go to LAD CCA1 when power in the air will be below a threshold, and we run a test to verify that. The result of this test showed indeed that LAD stayed in CCA1-Wait while power in the channel was high (a transmission was ongoing) and went to low when the packet was finished, allowing LAD to take over and do its CCA and then transmit. In Figure 18, the second row shows the FSM state, and the 3rd row shows the RSSI value, the horizontal axis denotes time. We can see the state of the HW transmission chain to be in *LAD_CCA1_WAIT* state and only when the RSSI measurement drops below the threshold at sample time 175 (yellow line) the status of the HW transmission chain switches to *LAD_CCA1* state in order to

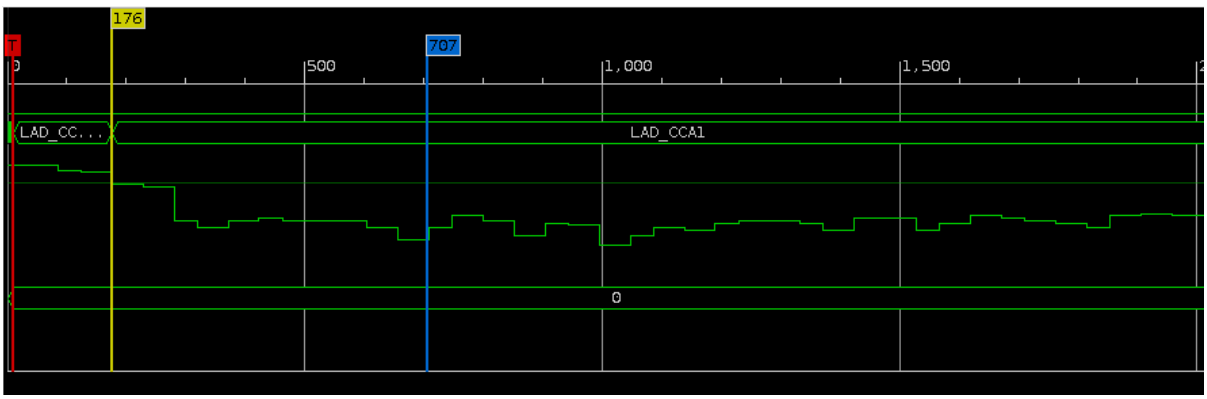

FIGURE 18. VERIFICATION TESTS FOR LAD HW IMPLEMENTATION

CCA for 10 μs. We could also measure the response time of our RSSI implementation to be in the order of 80 to 280 samples (200 samples duration with a clock of 100 MHz), equal to a response time to the event of packet finished transmission of 2 μs.

The frequency used for our LAD link had to be in the range of channel 13 of Wi-Fi in the 2.4 GHz ISM band in order to coexist with the 2 Wi-Fi links that were also using channel 13, more precisely in the 2462 to 2482 MHz range; therefore, we chose as centre frequency of our LAD link the 2477 MHz.

Regarding the Wi-Fi nodes, as mentioned already we used Intel AX200 Wi-Fi cards that can support up to IEEE 802.11ax but are also backwards compatible to IEEE 802.11b/g/n/ac. We set 2 access points and 2 clients nodes all using the same channel, channel 13 in the 2.4 GHz band operating in IEEE 802.11g mode, naming one link as Wi-Fi_P and the other as Wi-Fi_B. The PHY rate used was 48 Mbits per second, corresponding to MCS 6. As the 2 Wi-Fi links are meant to act as typical Wi-Fi devices available today, we decided not to lower their data rate to be comparable with the LAD link, but to allow them to have more than 5 times capacity compared to the LAD link and measure the QoS performance since we are focusing on latency and jitter which is the main issue for industrial control applications. We argue that it is not ample bandwidth that is the solution for industrial control applications, but rather more carefully designed MAC access protocols, that provide hard prioritization of traffic and stable medium access latency and jitter.

As it has been shown in WP2, a typical robotic link control flow requires no more than a few Mbps, but it has very strict latency and jitter requirements in order for the link to be stable. To mimic a robotic arm control flow, we choose our 2 flows (one in LAD link and one in Wi-Fi_P link) to be a representation of a typical 2 ms control loop implemented in a PLC-slave robot industrial setup. In Table 4 the settings of the incoming flows in the demonstrator are presented.

TABLE 4. TRAFFIC FLOW SETUP

LAD robotic arm control link		**Wi-Fi 1 robotic arm control link**		**WiFi2 background traffic**	
PPS	**Packet size**	**PPS**	**Packet size**	**PPS**	**Packet size**
500	300 bytes	500	300 bytes	500-2500	1400
1.2 Mbps		1.2 Mbps		Varying 5.6 to 28 Mbps	

The target of the demonstrator is to showcase the QoS offered from the 2 robotic links, one from typical Wi-Fi based COTS device and the other from the proposed LAD MAC scheme as the load of the network increases. WiFi2 link will vary its application layer load from 5.6 Mbps up to 28 Mbps saturating the capacity of the wireless medium in the latter case, as the PHY rate is only 48 Mbps but that translates to approximately a bit lower than 30 Mbps of application layer traffic if MAC and PHY headers and other protocol overhead is considered.

An image of how the spectrum looks like on the maximum load setting of the demonstration scenario is presented in Figure 19. What is presented, is a typical spectrogram, where X axis denotes time and Y axis frequency. Based on the detected power in the frequency-time space, the pixel colour is changing (see signal power to colour map on the right of the figure) to depict signal power detected. Hence, it becomes clear that the orthogonal figures in light blue are packet transmissions of ~64dBm power that are registered in the spectrogram. Since only Wi-Fi was transmitting at that time in the specific frequency range, we easily deduct that this is the Wi-Fi packet flow. We can see that indeed the channel is saturated, and Wi-Fi packets are coming continuously, leaving little space for anything else to be transmitted. We have hence concluded that our test is indeed designed correctly to evaluate the LAD MAC from low to very high load settings and the scene is ready to execute our series of experiments and evaluate the baseline, that is performance of the Wi-Fi_P link while Wi-Fi_B varying load vs the LAD link in the same conditions.

Hence, 2 series of experiments were executed, one with only the Wi-Fi_P and Wi-Fi links active and one with all 3 links active so we can compare the performance of both robotic arm control links vs the load. Each series is comprised of 5 experiments with a duration of 1000 seconds each, based on the varying background traffic from 500 to 2500 packets per second with a step of 500 packets increase per experiment.

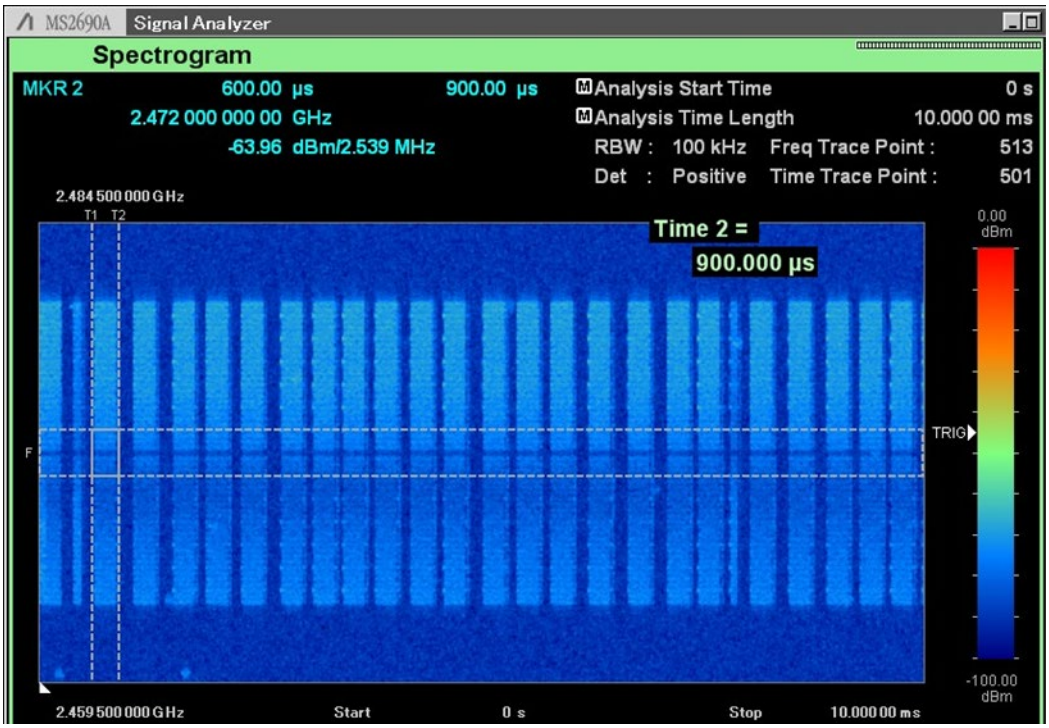

FIGURE 19. SPECTRUM STATUS WHEN BACKGROUND TRAFFIC IS SET AT 28 MBPS

4.2.5 RESULTS

The results of the experiments conducted using our implemented PoC are going to be presented. First the baseline results are going to be presented to show what SoTA devices can offer today and then we will move to the results with the proposed LAD MAC to compare against the baseline and come finally to conclusions about the performance and provided QoS in general of the proposed scheme.

Before presenting quantitative results, we would like to offer also some interesting findings that occurred during our PoC experiments execution. For instance, we were able to visually identify that the proposed scheme offers hard prioritization of accessing the medium with a very small probability of collision that is relevant to the max steps selected for deconfliction between LAD devices. As IEEE 802.11g slot time in the 2.4 GHz is 9 µs, that means that after the medium is free, there is a possibility every 9 µs that some nodes backoff counter reaches zero and might try to get medium access. In order to minimize this probability, the LAD maximum sensing time must be minimized to the smallest possible multiples of 9 µs. As a result, we have chosen in our experiments to use 3 steps of 3 ms each as the deconfliction randomization LAD setting, with an initial CCA time of 10 µs and a subsequent CCA period of 3-5 µs after the deconfliction period, offering a maximum medium access scheme from time that LAD starts sensing the medium until first sample is in the air of only 24 µs. As LAD is periodic, the starting time of LAD is always the start of the LAD period unless there is an active transmission. In Figure 20 we present an LAD packet getting access to the medium 24 µs after a Wi-Fi packet and its ACK finished transmission. The figure depicts two-time markers, T1 and T2 (vertical time marking lines), that denote the end of a packet ACK and the start of the LAD packet. The markers time is shown in the upper left of the figure. As T1 is at 824us and T2 is at 848us, the difference between them is calculated as 24us of interpacket time. This is in line with our design and within the expected boundaries of LAD MAC access delay, taking into account that we are not sure in this image if LAD started after Wi-Fi packet ended transmission of if it started during Wi-Fi packet transmission and the random step selection was set to 3.

The wider packets in Y axis (denoting frequency) are 20 MHz Wi-Fi packets while the LAD packet is 10 MHz and clearly visible with its main packet and ACK in the image. In multiple images like this we measured the period

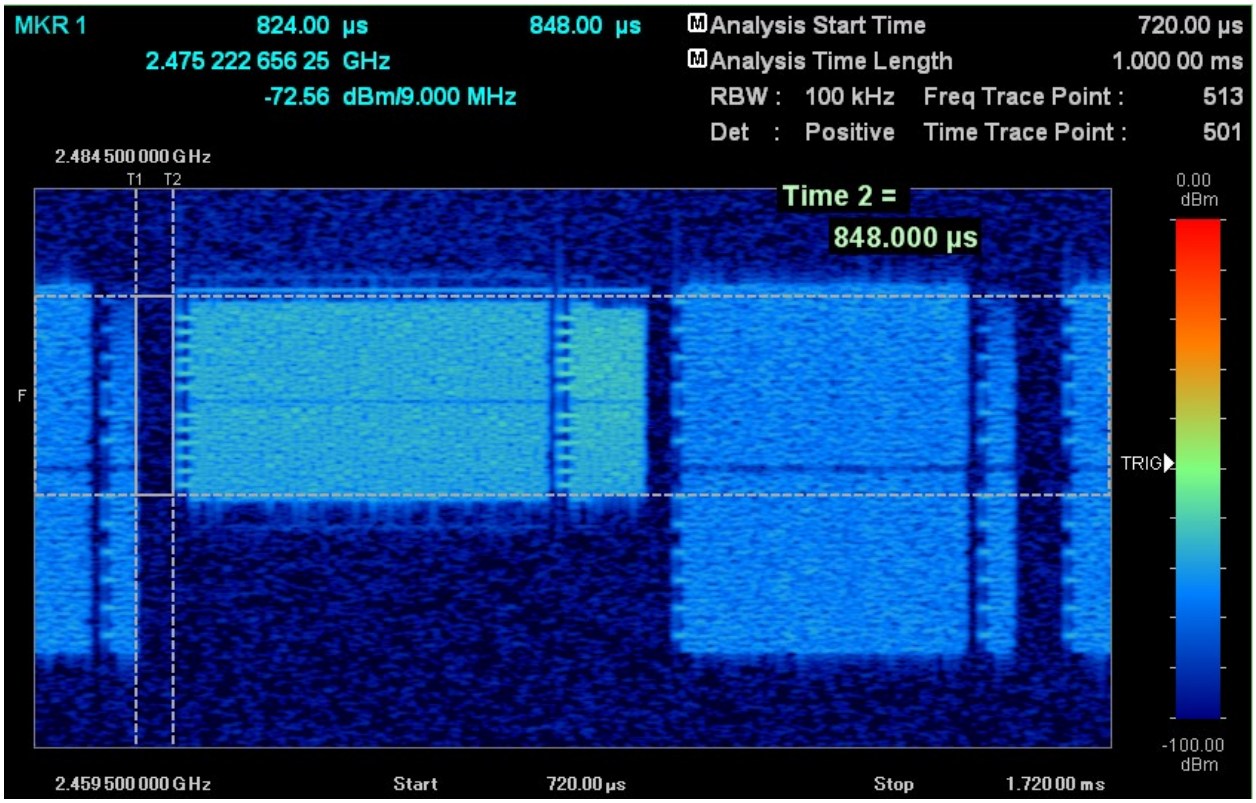

FIGURE 20. LAD ACCESS SCHEME IN ACTION

between the previous packet and the LAD packet and found them to be in line with the LAD design in all cases, that is between 18 and 24 µs for a 3 steps x 3 µs randomization step.

4.2.5.1 BASELINE RESULTS

After execution of the series of 5 experiments of only Wi-Fi1 and Wi-Fi2 links active, there were some initial conclusions. Packet loss was 0 at all times, meaning a retransmission of 1 was more than enough to accommodate any PHY packet loss in our demonstrator setup. That makes sense as the devices are located close by, and external interference was minimized by using channel 13 in the 2.4 MHz band that most devices do not support. We also run the experiments overnight when our laboratory is not used and there are no other wireless devices accessing the air in the vicinity of our demonstrator. Hence graphs of packet loss have no information to show, and throughput was almost stable unless a retransmission happened beyond a second measured period, inducing a small variation in throughput.

A typical throughput graph is shown in Figure 21. We will use quantitative analysis of throughput results to ascertain impact on background throughput from the LAD link presence.

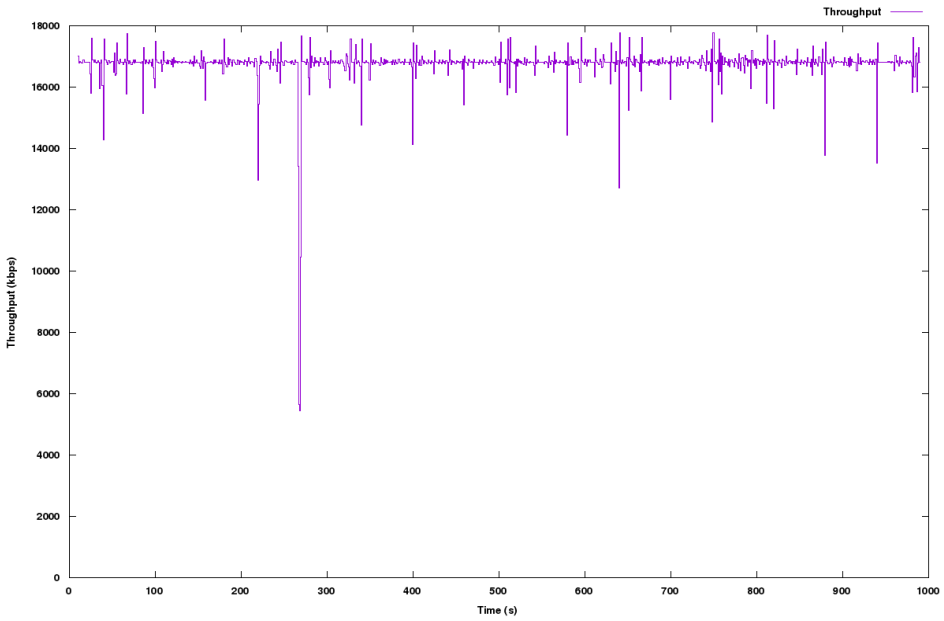

FIGURE 21. 16.8 MBPS WI-FI BACKGROUND TRAFFIC THROUGHPUT

One first straightforward conclusion is that, although we expected a more stable 16.4 Mbps throughput graph as we have not saturated yet the medium, just the presence of the Wi-Fi1 link is enough to create various spikes in the achieved throughput of the background link.

The quantitative analysis for throughput is shown in Figure 22 for the entirety of the 5 experiments of the baseline series were only Wi-Fi1 (priority robotic arm control traffic) and Wi-Fi2 (background traffic) is present in the wireless collision domain.

A quick conclusion is that, for the 2 lower background traffic experiments, both background and robotic arm control traffic (denoted in the figure as Wi-Fi_P for priority and Wi-Fi_B for background together with their PPS setting) are perfectly stable as far as throughput is concerned as their min and max is almost equal to the average and expected value of 1200 kbps for the Wi-Fi_P traffic and 5600 and 11200 for the Wi-Fi_B 500 and Wi-Fi_B 1000 traffic, respectively. After that point the background traffic is fluctuating significantly while the Wi-Fi_P 500 traffic keeps stable across all times. It seems that after a 15 Mbps load, CSMA starts to show its disadvantages as load is

	WIFI_P-500	WIFI_B-500	WIFI_P-500	WIFI_B-1000	WIFI_P-500	WIFI_B-1500	WIFI_P-500	WIFI_B-2000	WIFI_P-500	WIFI_B-2500
AVG	1200,0	5598,2	1200,0	11200,0	1199,8	16746,5	1200,0	18887,9	1200,0	19339,2
MIN	1053,6	4648,0	1147,2	10897,6	957,6	5443,2	1120,8	13540,8	1147,2	15881,6
MAX	1356,0	6059,2	1252,8	11491,2	1411,2	17774,4	1291,2	21067,2	1248,0	20742,4

FIGURE 22. BASELINE THROUGHPUT RESULTS

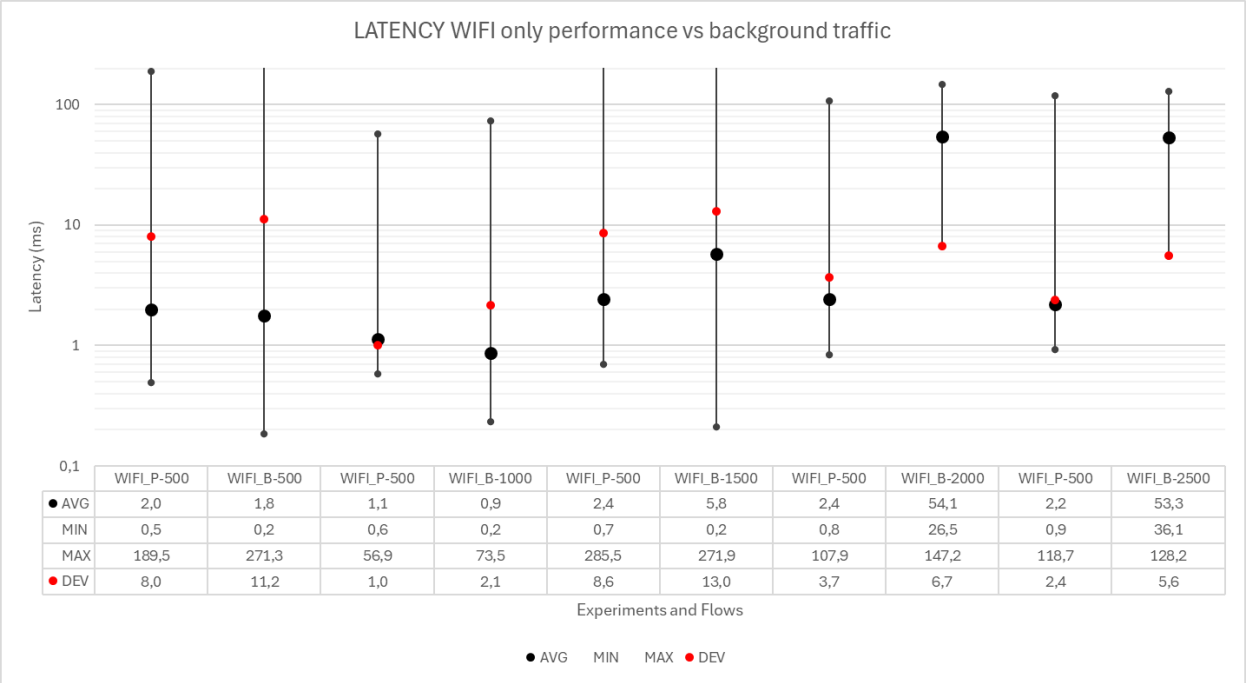

	WIFI_P-500	WIFI_B-500	WIFI_P-500	WIFI_B-1000	WIFI_P-500	WIFI_B-1500	WIFI_P-500	WIFI_B-2000	WIFI_P-500	WIFI_B-2500
AVG	2,0	1,8	1,1	0,9	2,4	5,8	2,4	54,1	2,2	53,3
MIN	0,5	0,2	0,6	0,2	0,7	0,2	0,8	26,5	0,9	36,1
MAX	189,5	271,3	56,9	73,5	285,5	271,9	107,9	147,2	118,7	128,2
DEV	8,0	11,2	1,0	2,1	8,6	13,0	3,7	6,7	2,4	5,6

FIGURE 23. BASELINE LATENCY RESULTS

now close to 50% capacity. And this is why throughput is no longer stable and also not close to its theoretical output for the 2 higher load experiments (18,8 and 19.3 Mbps versus the expected 22.4 and 28 Mbps). Regarding latency, we present in Figure 23 the relevant baseline results in a similar manner, including also the deviation of latency that is very important for the stability of an industrial control loop.

It is again clear that latency is stable in a relatively low average of 1-3 ms for the 3 lower load experiments (Wi-Fi_P and Wi-Fi_B flows presented per single experiment in Figure 23 but then increases significantly for the 4th and 5th experiment as far as background traffic is concerned. The Wi-Fi Priority traffic, that represents the robotic arm control flow, although it manages to keep its average below or equal to 4 ms for all cases, it exhibits very high maximum latency across the board of experiments. This instability of CSMA based access MAC schemes is well known and one of the main reasons why Wi-Fi has not been adopted for industrial applications except where bounded latency is not needed, or a percentile of packets lost or late can be tolerated. Minimum latency is kept extremely low in most cases except the 2 higher load experiments where Wi-Fi B flow is saturated and backoff algorithm has settled in high condition window values to try to mitigate the saturation of the channel. A deviation from 1 to 8.6 ms is also reported for the Wi-Fi_P flow, showing once more that even a low load traffic flow based on CSMA suffers from latency instability and jitter.

4.2.5.2 LAD MAC RESULTS VS THE BASELINE

Moving forward, the next series of experiments were executed including now an LAD enabled flow, same settings as the Wi-Fi_P robotic arm control flow. This setup will allow us to compare LAD vs Wi-Fi_P QoS, as they have the same flows working under the same network conditions but with a different MAC scheme enabled, while in parallel will also allow us to see the impact of the LAD flow presence to the background traffic.

Firstly, we present the latency and throughput average, max and min graphs of the entire series for some initial conclusions. Then, we will dive deeper on why some effects take place and try to provide an explanation and a possible way forward.

The throughput graphs show a fairly stable condition of both LAD and Wi-Fi_P traffic while the background suffers a deterioration in performance from the 3rd experiment and above, meaning from loads of 50% of channel capacity, which is expected for a 48 Mbits capacity channel. It is difficult to notice any differences in performance between LAD and Wi-Fi_P flows as they both seem stable. One thing that can be noticed is that LAD remains fairly stable

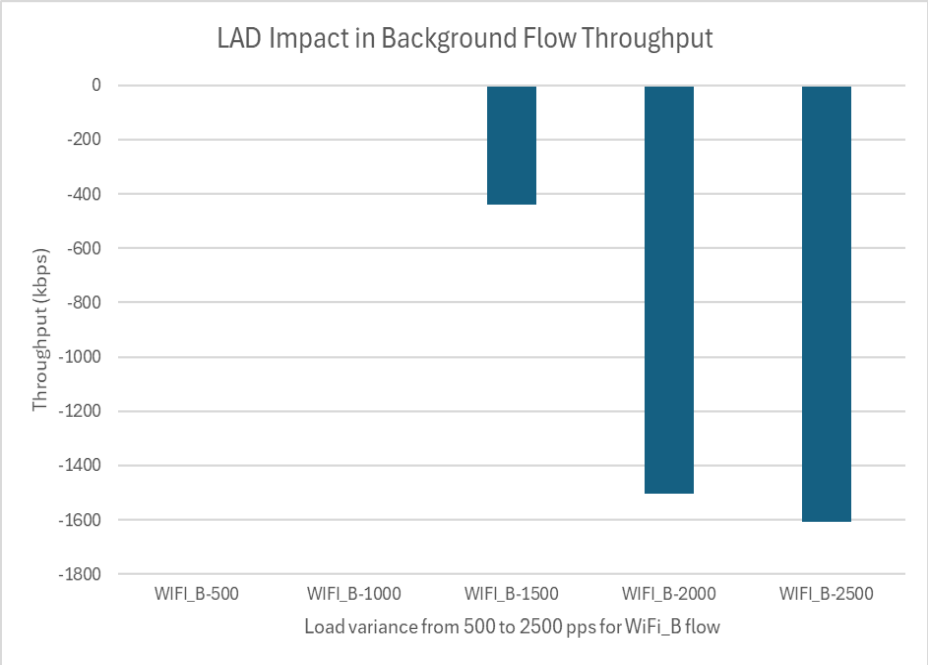

FIGURE 24. IMPACT OF LAD PRESENCE TO BASELINE WI-FI BACKGROUND TRAFFIC (WI-FI_B)

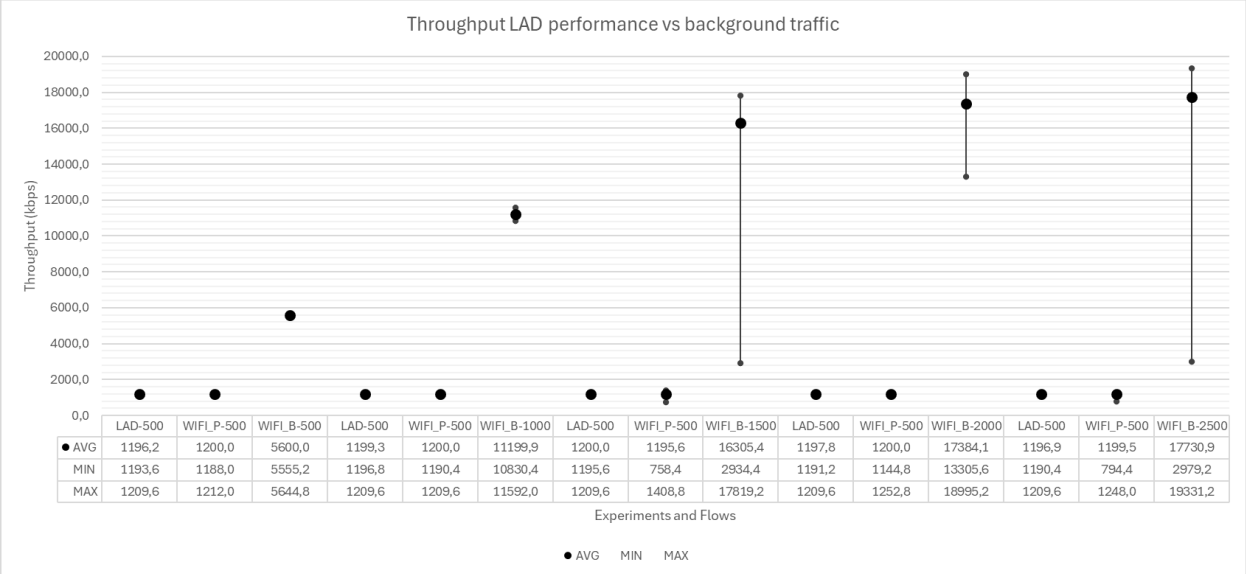

	LAD-500	WIFI_P-500	WIFI_B-500	LAD-500	WIFI_P-500	WIFI_B-1000	LAD-500	WIFI_P-500	WIFI_B-1500	LAD-500	WIFI_P-500	WIFI_B-2000	LAD-500	WIFI_P-500	WIFI_B-2500
AVG	1196,2	1200,0	5600,0	1199,3	1200,0	11199,9	1200,0	1195,6	16305,4	1197,8	1200,0	17384,1	1196,9	1199,5	17730,9
MIN	1193,6	1188,0	5555,2	1196,8	1190,4	10830,4	1195,6	758,4	2934,4	1191,2	1144,8	13305,6	1190,4	794,4	2979,2
MAX	1209,6	1212,0	5644,8	1209,6	1209,6	11592,0	1209,6	1408,8	17819,2	1209,6	1252,8	18995,2	1209,6	1248,0	19331,2

FIGURE 25. LAD, WI-FI_P AND WI-FI_B THROUGHPUT RESULTS

across all scenarios while Wi-Fi_P does seem to suffer from time to time from some local instability in throughput based on its max and min values, in accordance to what we have seen also for its latency. Probably, retransmissions are used in a broader aspect in higher load scenarios and in conjunction with high range of contention window impacts also the throughput per second min max measurement although the average remains very close to the theoretical 1200 kbps.

The impact of LAD flow presence on throughput of background flow Wi-Fi_B is shown in Figure 24, comparing achieved throughput in baseline vs what was achieved with the LAD traffic also in the air. We can see that there

was some drop in throughput in the third scenario of around 400 kbps out of an aimed 16.8Mbps (2.6% lower than what was achieved in baseline), while for the 2 higher load scenarios the drop vs the baseline is larger and around 1500-1600 kbps which happens to be a bit more than the actual traffic added to the scenario with the LAD flow link introduction on top of the 2 Wi-Fi links in the baseline. It is indeed expected to lose around 1200 kbps of traffic throughput so LAD flow can claim that and access the medium to serve its own needs. As LAD is designed to take precedence in accessing the medium vs other CCA based access schemes like CSMA, this was the desired result.

Looking at these results the need for one more series arises, to run also a standalone LAD – Wi-Fi_B only series of runs that could give us more insight and allows us to measure the impact of LAD when it replaces the Wi-Fi_P flow and not when it is simply added on top in the collision domain. This would be one of our next steps for the near future, and it would be far more important and useful in order to ascertain correctly the throughput and surely also the latency impact of LAD on background traffic in equal terms with the Wi-Fi_P flow.

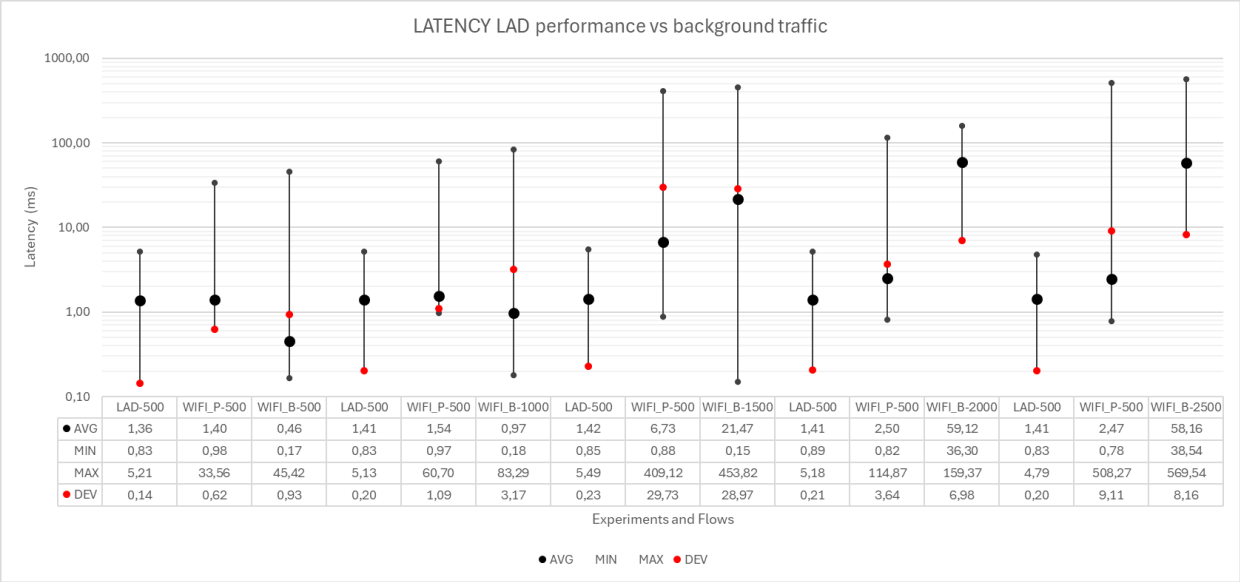

	LAD-500	WIFI_P-500	WIFI_B-500	LAD-500	WIFI_P-500	WIFI_B-1000	LAD-500	WIFI_P-500	WIFI_B-1500	LAD-500	WIFI_P-500	WIFI_B-2000	LAD-500	WIFI_P-500	WIFI_B-2500
AVG	1,36	1,40	0,46	1,41	1,54	0,97	1,42	6,73	21,47	1,41	2,50	59,12	1,41	2,47	58,16
MIN	0,83	0,98	0,17	0,83	0,97	0,18	0,85	0,88	0,15	0,89	0,82	36,30	0,83	0,78	38,54
MAX	5,21	33,56	45,42	5,13	60,70	83,29	5,49	409,12	453,82	5,18	114,87	159,37	4,79	508,27	569,54
DEV	0,14	0,62	0,93	0,20	1,09	3,17	0,23	29,73	28,97	0,21	3,64	6,98	0,20	9,11	8,16

FIGURE 26. LAD, WI-FI_P AND WI-FI_B LATENCY RESULTS

Moving forward to latency related results, we present in Figure 26 the overall latency statistics of the LAD enabled series and then compare the achieved latency against the baseline to get a proper indication not only of LAD MACs performance advantages, but also of the impact on other incumbent traffic flows in shared bands.

An initial observation is that the LAD link achieves remarkable stability as far as latency is concerned across the range of experiments, all the way to the highest load of Wi-Fi_B-2500 that saturates the wireless channel. The average latency remains stable from 1.36 ms to 1.42 ms while the max/min remain similar across all runs. The maximum that is very important for industrial applications remains stable as well and only ranges from 3.29 to 5.08 ms while the max of the Wi-Fi_P similar traffic flow ranges from 33 all the way to more than 500 ms. The deviation of the LAD scheme also shows clearly the same picture as it remains stable from 0.14 ms to 0.23 ms across all scenarios, providing an excellent latency profile.

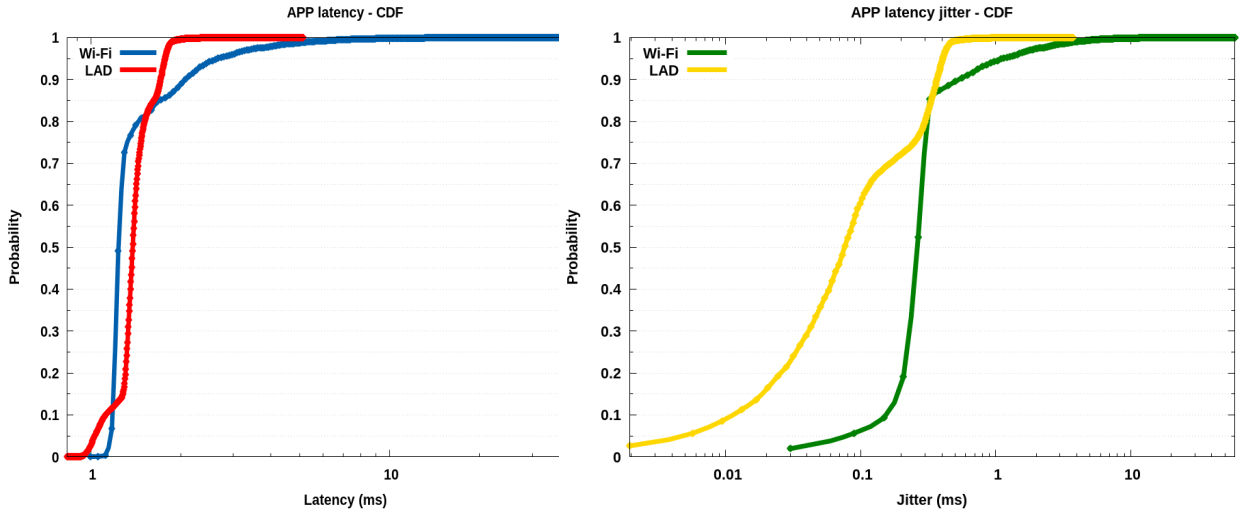

FIGURE 27. CDF OF LAD, WI-FI_P FLOWS APP LATENCY AND JITTER IN 1000 PPS BACKGROUND TRAFFIC SCENARIO.

To see more details and make sure the numbers do not lie, we dive into specific runs to check specific delay measurements and compare directly Wi-Fi_P and LAD latency and jitter raw values, PDF and CDFs. The resulted graphs paint clearly the same image, LAD delivers excellent latency profile and outperforms the similar Wi-Fi_P traffic flow in every KPI, offering extreme improvements in QoS.

Choosing an average load scenario, for example the 1000 PPS in Wi-Fi_B, the achieved PDF latency and jitter of LAD vs Wi-Fi_P flow is presented in Figure 27 . Please take note that the X axis is logarithmic as the Wi-Fi maximum latency reaches values of around 73 ms while LAD MAC caps at 3.4 ms which is an astonishing difference, a 20 times lower LAD max experienced latency than the Wi-Fi_P flow. The Wi-Fi_P latency profile shows clearly that many packets are delivered very fast, but unfortunately more than 17% of packets are delivered considerably

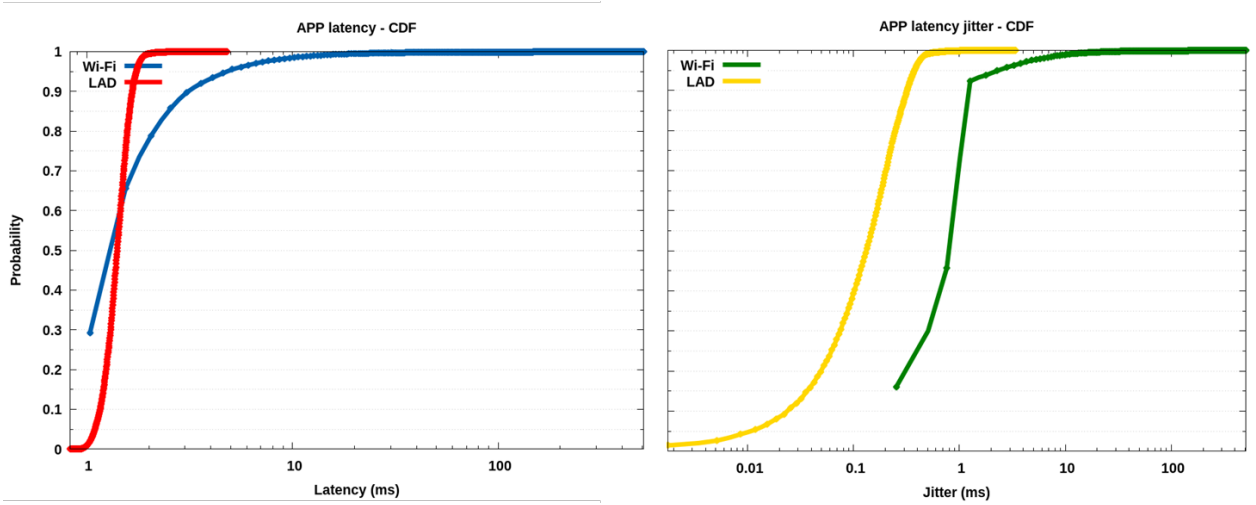

FIGURE 28. CDF OF LAD, WI-FI_P FLOWS APP LATENCY AND JITTER IN 2500 PPS BACKGROUND TRAFFIC SCENARIO.

slower than LAD which has only 9 Mbps PHY rate while Wi-Fi has a 48 Mbit PHY rate. This proves once more that although average latency is relative to channel capacity, bounded latency is mainly a matter of correct MAC design,

and capacity can help but cannot guarantee deterministic operation especially under medium and high network loads.

The comparison of the achieved jitter paints the same picture, as LAD jitter starts at almost 0 and caps at ~2 ms while Wi-Fi_P jitter CDF profile starts at 0.03 ms and caps at more than 40 ms.

One more similar comparison is made in the highest load scenario and the results again clearly draw the same picture with even wider differences between the Wi-Fi and LAD access schemes, as it can be seen in Figure 28.

To conclude with the presentation of results, a comparison of Wi-Fi_B achieved latency when LAD flow is active is also presented to ascertain the impact of LAD addition in the topology, bringing 1 more node competing to get medium access and 1.2 Mbps traffic into the collisions domain. In Figure 29 we can see that there is some impact in the three higher load scenarios, as far as latency is concerned, to the Wi-Fi-B traffic while the high priority Wi-Fi-P traffic remains slightly affected mainly in the middle load scenario of Wi-Fi_B-1500. It appears as the deterioration point of CSMA was pushed to the left from the baseline as CSMA started to suffer in the Wi-Fi_B-2000 scenario in the baseline scenarios. This could be attributed to the additional 1.2 Mbps of load that the LAD link brought to the channel as well as to a third contester that is trying to get access to the medium. Overall, the impact is minimal, but some deeper insight is needed on the middle scenario impact in order to make sure that this is indeed the saturation point of CSMA talking and not some incompatibility of the LAD mechanism that impacts CSMA under specific conditions. It has been observed also in the baseline scenario a big jump in latency from 5.8 ms average to 54 ms between scenario Wi-Fi_B-1500 and Wi-Fi_B 2000, because load exceeds 60% of available channel capacity with the added load.

To dive deeper to the heart of this issue and understand better what is the reason behind this latency deterioration of the background traffic flow, we must execute more experiments and try to recreate this scenario in the NS3 simulator to see if we can pinpoint any design decision that is the cause of this. We will execute in a later phase one more series of experiments with 2 Wi-Fi_P flows to see if the same situation arises and one series with only 1 LAD link and the Wi-Fi_B. These additional experiments will provide us the needed insight to explain without any doubt that the observed local maximum of impact on latency in our current experiments is coming from CSMA saturation. Depending on the results we will decide for our next steps, adapting the design of LAD to mitigate possible issues identified, aiming to maximize performance gains while minimizing impact to other CSMA/CCA bases MAC schemes.

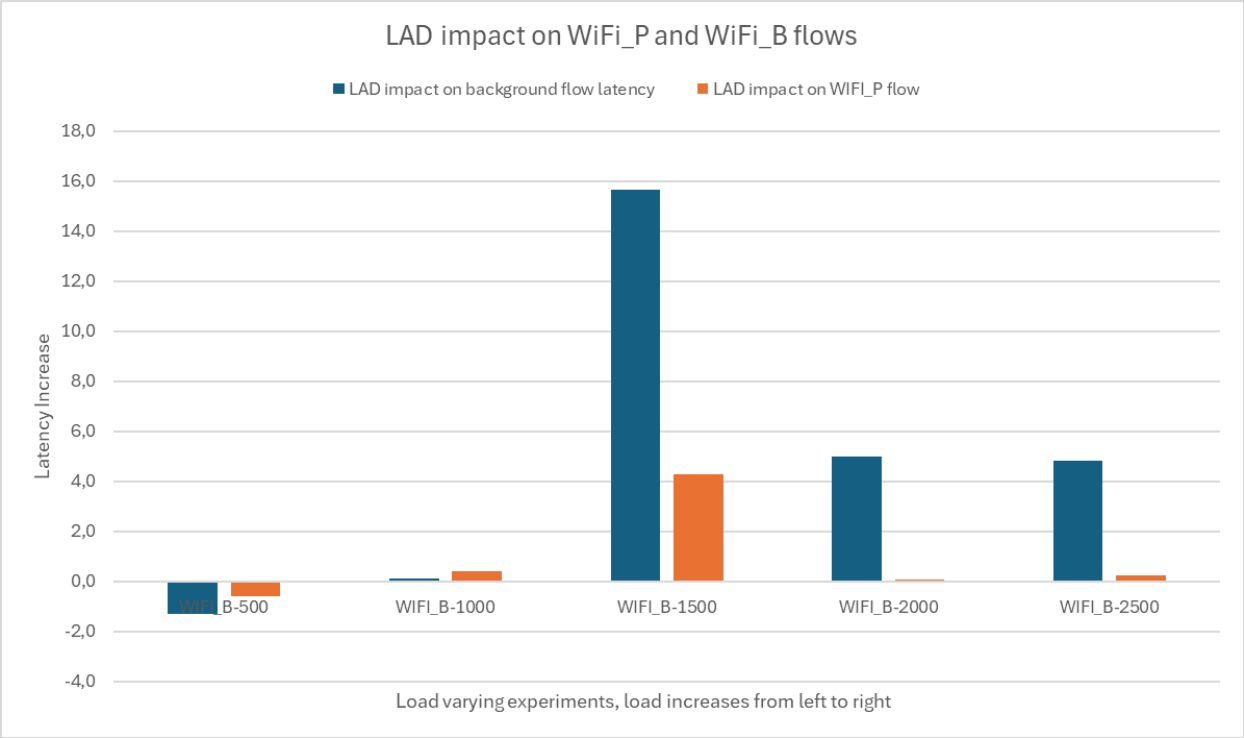

FIGURE 29. LAD FLOW ADDITION IMPACT IN WI-FI BACKGROUND LATENCY VS BASELINE

4.2.5.3 USE CASE MAPPING OF ACHIEVED RESULTS

The PoC demonstrator was used to evaluate the performance of the proposed LAD MAC scheme while implementing a Robotic arm control traffic flow, according to the findings of WP2 related to the packet size and packet interarrival time profile of such a control loop [5]. We chose to model our robotic arm control traffic flow based on the WP2 model and put it to the test. The scenario of our demonstrator clearly depicts an industrial site where multiple wireless devices offer connectivity and there are different traffic profiles. Some have a profile with high priority and importance like a robotic arm control loop traffic flow and others with lower priority like a visualization data link or telemetry of non-critical components.

In this typical environment we have proven that the proposed LAD MAC can offer significant advantages as far as QoS is concerned and offer very stable latency profile with bounded latency as low as 4 ms and jitter down to 200 µs with just a 10 MHz PHY rate channel, 1 ms LAD periodicity and low MCS SISO OFDM based PHY implementation. These results clearly empower us to move forward and test further LAD MAC in higher PHY rates. We would like to notice here that in WP3 it is identified that such robotic control arm applications require more than 100-200 MHz channel BW with MIMO setup of 4x4 or 8x8 to be viable with today's MAC schemes and solutions, while in our PoC we proved that we could support such an application with just 10MHz of channel BW in SISO mode. This clearly indicates that deterministic networking is not enabled by just higher BW channels and overall larger capacity but mainly from appropriate MAC design.

4.2.5.4 CONCLUSION

We have presented the PoC demonstrator of the proposed in WP3 technology component LAD MAC for latency aware access in shared frequency bands. The demonstrator was used to evaluate in real life experiments the performance and advantages theory showcased in WP3 where it was evaluated with simulations. Based on our results, LAD MAC outperforms greatly any CSMA/CCA based scheme in terms of latency profile (latency, jitter) and can be a very important enabler in order to harvest the unused potential of shared access bands in the 6G era and allow subnetworks to tap to unused capacity keeping the QoS hard requirements imposed from industrial applications. These findings are aligned with the simulation results of LAD, presented initially in D3.1 [3] , although the LAD design has been slightly altered during the continuous R&D process in the last year in order to mitigate specific performance degradation factors identified in D3.1.

We have identified next steps in our research, moving forward to further evaluate the proposed solution and enhance its performance taking new design elements from the theoretical related work in WP3 from our group, like the ability to strobe multiple LAD packets in a row after an LAD period activates, to further support lower periodicity of LAD than just 1 ms and be able to go down to less than 300 µs LAD slot size and higher RSSI sensing accuracy in order to further tighten the timings of the proposed scheme for even higher performance gains and advantages. These design enhancements and their respective impact in performance will be evaluated and presented in the final deliverable D5.3 of WP5.

4.3 JAMMER RESILIENT PHY

4.3.1 GENERAL DESCRIPTION

This PoC demonstrates the technology component related to TC6 “Jamming-aware native PHY design”, which is also described in D3.1 Section 2.4.2 i.e. the approximated log likelihood ratio (ALLR) based de-mapper. We aim to show that the improved demapper in an OFDM based receiver can effectively improve receiver’s sensitivity, reduce packet error rate when a wide band jammer is being present. In this PoC demonstrator, we first show that the impact of a wide band jammer is equivalent to AWGN noise. We then show that by using the ALLR based de-mapper, the receiver sensitivity is significantly improved, especially in multi-path environment. It is also worth to mention that the resilience against a narrow band jammer will be offered by another technology component which will be covered by future work in both WP3 and WP5.

4.3.2 ENHANCED/NEW FUNCTIONALITY

As discussed in D5.1, this technology component enhances the robustness of decoder in a multi-path environment especially when an external interference is present. In order to ease the comparison, the threshold based demapper and LLR based demapper is put side by side into the same FPGA design, and can be switched dymamically by software control, this is highlighted in Figure 18 of D5.1. During the course of 6G-SHINE, the demapper has been revised in a few iterations. In comparison with earlier versions, the FPGA footprint has been reduced but the functionality is not affected. The architecture is simplified, and the search of the best soft bits is now more robust and efficient.

4.3.3 HIGH LEVEL ARCHITECTURE OF THE IMPLEMENTED POC DEMONSTRATOR

The demonstrator consists of an R&S CMW 270 tester, a combiner and an openwifi board (Zynq 7000 zc706 with FMCOMMS2 frontend). The openwifi receiver can be configured to either use the hard bit demapper, or the default soft bit demapper, or the new ALLR based soft bit demapper. The real-life experiment setup is shown in Figure 30, and the corresponding diagram is shown in Figure 31.

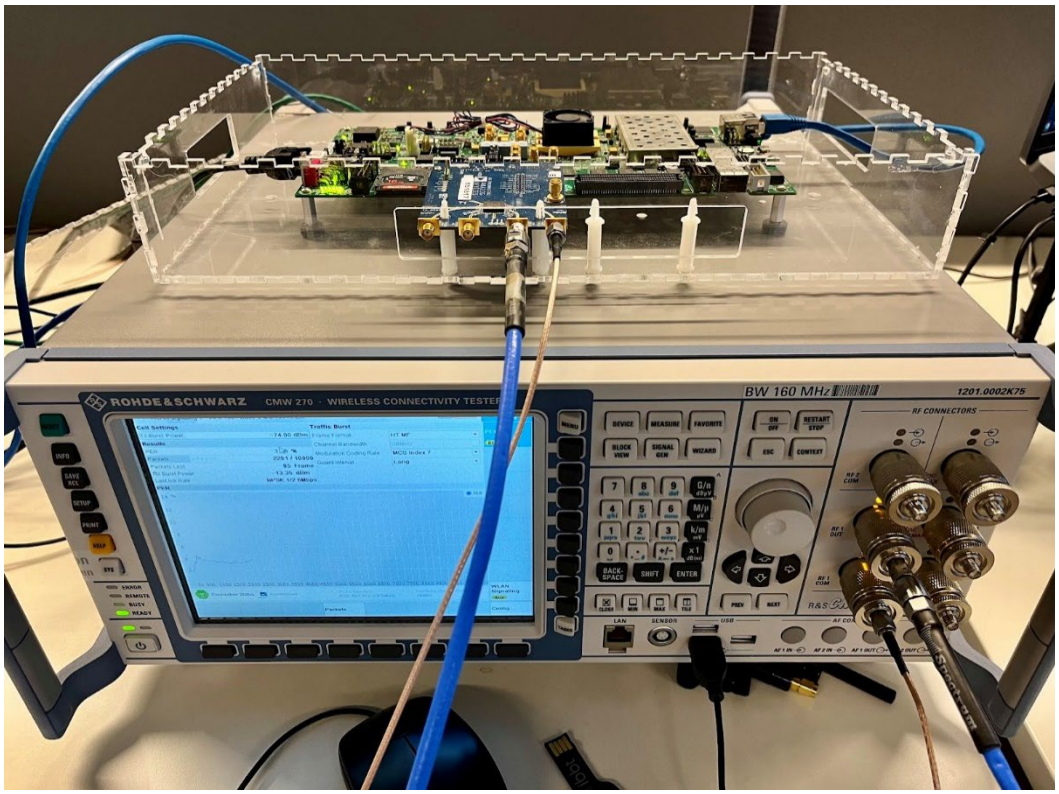

FIGURE 30. REAL-LIFE EXPERIMENT PICTURE

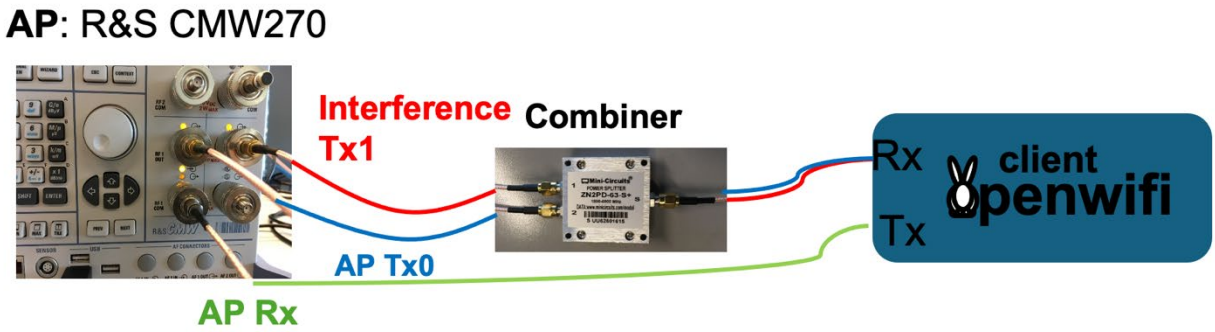

FIGURE 31. POC OF ALLR DEMONSTRATOR

The CMW 270 acts both as Wi-Fi access point (AP) and jammer. The Wi-Fi packets are transmitted by its RF port marked as Tx0, and the jammer's interference signal is generated by port Tx1. The two signals are combined and then fed to the openwifi, which acts as Wi-Fi client. The openwifi Tx port is connected back to another RF port on the Wi-Fi tester. In this way packet error rate between the AP and client can be measured.

4.3.4 DEMONSTRATOR SCENARIO DESCRIPTION

To clarify the scope of this PoC, we define two types of jammers, first type of jammer is that it occupies wider bandwidth than our communication system, hence termed as the 'wideband jammer', the second type of jammer occupies narrower bandwidth than our system, hence referred to as the 'narrowband jammer'.

The first set of experiment is designed to prove wideband jammer's impact on PER is equivalent as increased noise. At first the receiver sensitivity is measured when the jammer is disabled.

As seen in the screenshot of CMW 270, from the top left side of Figure 32, the sensitivity for MCS7 is around -61.6 dBm when no transmission is enabled on TX1.

Then the TX1 port is used to add AWGN noise, and in order to keep the PER around 10%, the TX0 power has to be increased from -61.6 to -51 dBm, as depicted in top right of Figure 32.

Thirdly, TX1 is used to transmit Wi-Fi signal, which acts as jammer, though with standard Wi-Fi packets as jammer, the PER is increased to 59.3% even after adjusting TX0 power. This is because if the receiver already started decoding the jammer's packet, it will miss the Wi-Fi packet from TX0, causing much worse PER performance than expected.

Finally, the jammer signal is replaced by Wi-Fi packets but without the short preamble part. It is necessary to remove the short preamble, as otherwise the jamming signal would capture the attention of the Wi-Fi receiver, causing worse PER performance as seen in the previous test. The reason we chose modified Wi-Fi packets is that then the Jammer's signal has the same bandwidth as the Wi-Fi system, hence it is considered wideband Jammer. We observe from the lower right side of Figure 32, after wideband interference is enabled, when adapting Tx Burst Power is to -51 dBm, the tester measures similar PER as when noise is transmitted on TX0. This proves that the impact of the wideband jammer can be regarded as increased noise floor.

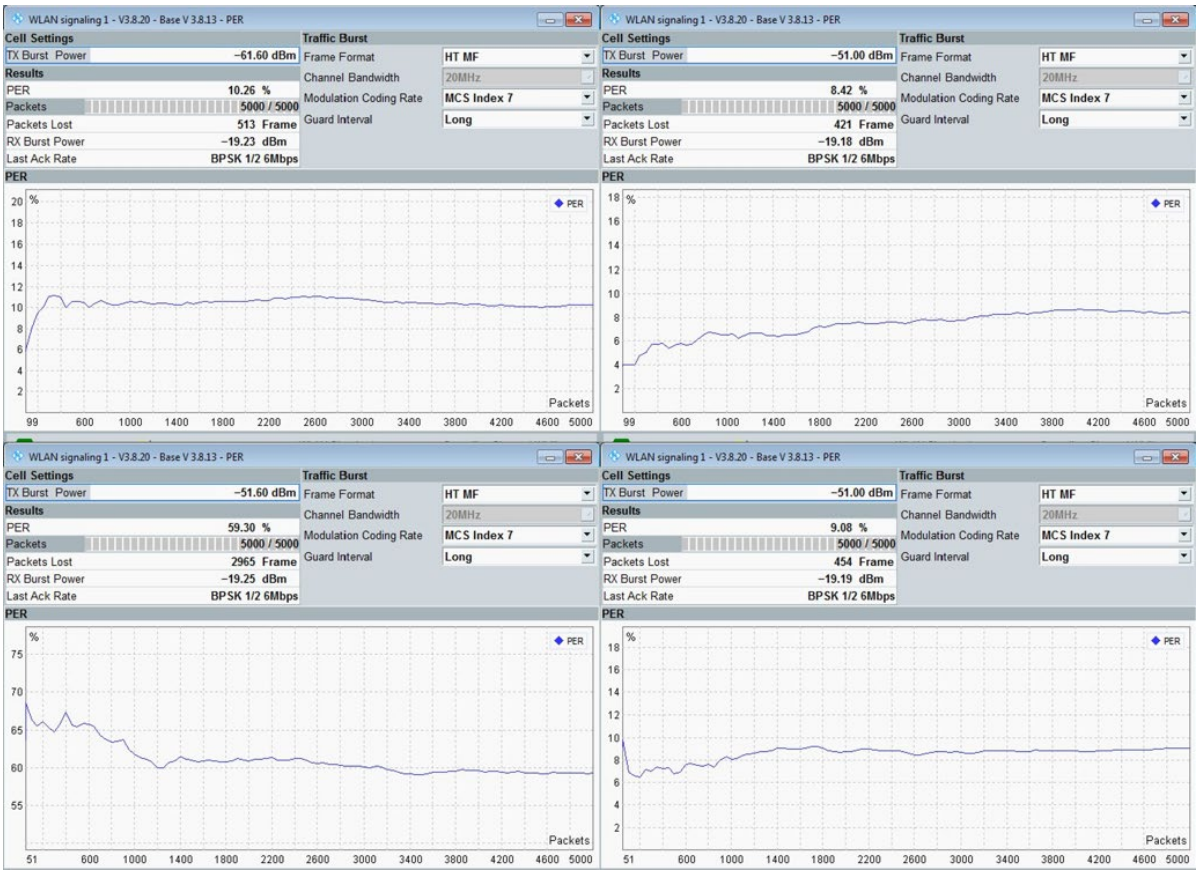

FIGURE 32. IMPACT OF WIDEBAND JAMMER IN TERMS OF RX SENSITIVITY.

The second set of the experiment is designed to prove the improvement of PER or receiver sensitivity when the ALLR based demapper is enabled, the results are shown in Table 5 and Figure 33. The experiment records the receiver sensitivity, which is defined as the received signal strength at which the PER is around 10%. The demonstrator includes measurement for different types of demapper, under different MCS configurations.

The PER is measured for 10000 packets with 1400 Byte payload size, at 2550MHz.

The introduction of multi-path channel effect is achieved by prefiltering the IQ samples with different realization of the channel Model-D, which is the channel model defined by IEEE 802.11 tgn work group for office environment [27]. Then load the filtered IQ samples into the CMW Wi-Fi tester. In total we selected 400 channel responses, which are repeated during the PER measurement.

The most dominant improvement is observed when ALLR demapper is used for packets with MCS 7 and are experiencing multi-path effect, up to 14 dB improved receiver sensitivity is observed when comparing ALLR and the original soft bit demapper, as shown in Table 5.

4.3.5 RESULTS

4.3.5.1 POC RESULTS VS THE BASELINE

The baseline of this demonstrator is the performance of the original threshold based soft bit demapper. The sensitivity is obtained by the TX power at the output of CMW 270 tester with calibration of the used coaxial cable (1.3 dB) in channel-D. Unfortunately, it is hard to achieve the exact 10% PER in real-life measurement, hence the openwifi PER at which the sensitivity is recorded is also recorded. For ease of comparison the performance of ALLR based demapper is listed side by side with the original demapper in the table below.

TABLE 5. THRESHOLD VS ALLR BASED DEMAPPER IN TERMS OF RX SENSITIVITY

	Original soft bit demapper		ALLR based demapper	
	Rx sensitivity (dBm)	Openwifi PER	Rx sensitivity (dBm)	Openwifi PER
MCS0	-90.1	9.89%	-92.3	7.48%
MCS1	-87.5	9.66%	-89.6	8.77%
MCS3	-82.3	9%	-84.8	9.21%
MCS5	-71.8	9.35%	-76.9	7.66%
MCS7	-53.5	9.66%	-67.3	8.1%

We observe from Table 5 that for lower MCS the improvement of ALLR based demapper against original soft bit demapper is not obvious. For instance, to compare the sensitivity for MCS0 between the LLR and the soft bit demapper, we substract -90.1 dBm from -92.3 dBm, only 2.2 dB is measured for MCS0. But for MCS7 the difference is enlarged to 14 dB. Meaning that at -53.5 dBm received signal power, the old demapper still results in 9.66% packet error, while the ALLR based demapper can already achieve 8.1% PER when the signal is received at -67.3 dBm. Additionally, we also plot the PER vs SNR for MCS7 in Figure 33, for both the ALLR base demapper and the original soft bit demapper. Note that the SNR in this figure is a measurement of energy received by the openwifi receiver, when CMW is transmitting packet (strength of signal) and when it is idle (strength of noise). It is worth mentioning that in Figure 25 of D3.1, we simulated the LLR demapper should have sensitivity around 28 dB for MCS7. And here we observe the measured Rx sensitivity for MCS7 is around 29 dB, so simulation and measurement are closely aligned.

For completeness, also the performance of the hard bit based demapper is included in the plot. The plot clearly shows that the hard bit based demapper will never achieve 10% PER, the original demapper did achieve 10% PER, at SNR around 39 dB, but for ALLR based demapper, SNR of less than 30 dB is sufficient.

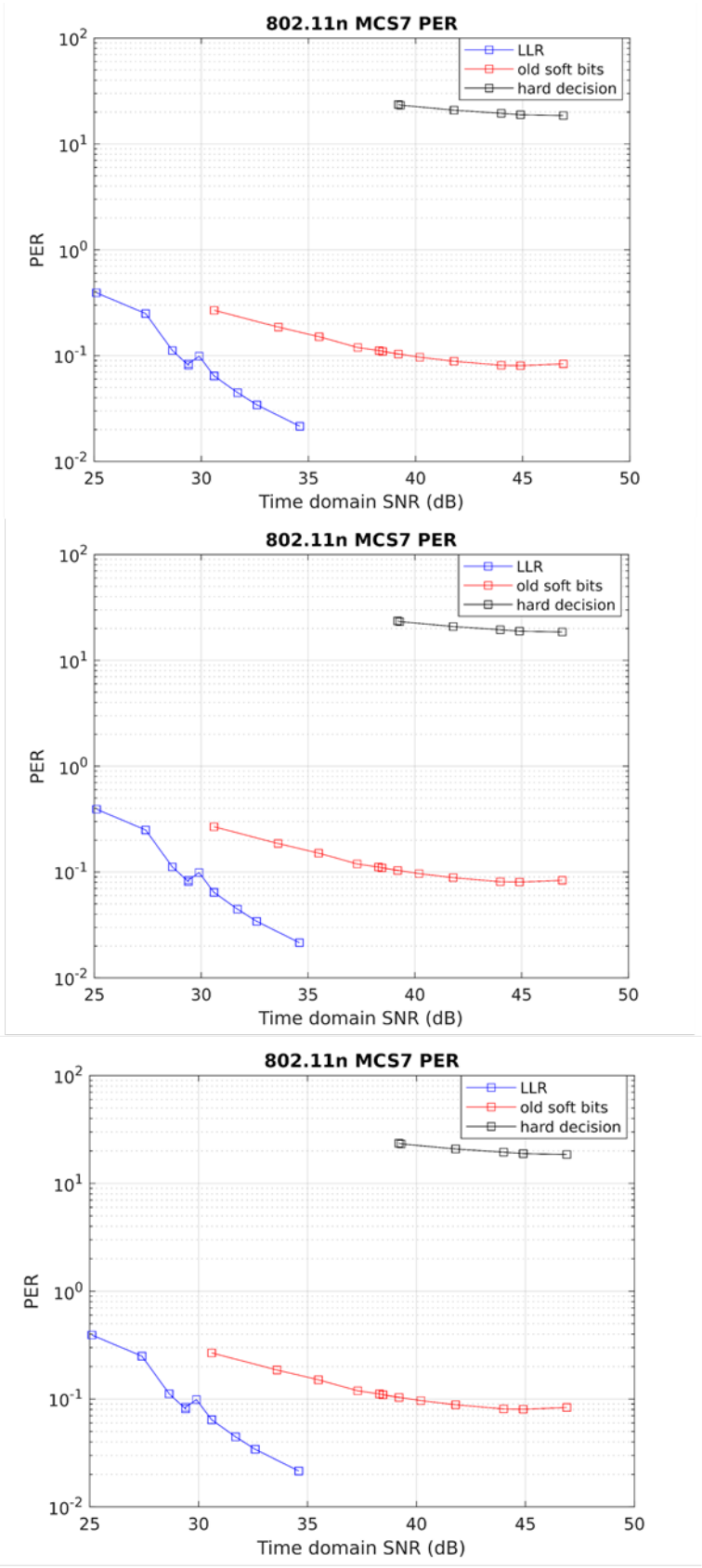

FIGURE 33. PER VS SNR PER DEMAPPER

4.3.5.2 MAPPING OF ACHIEVED RESULTS TO RELEVANT USECASE

This technology component is mainly linked to the robot control use case. When receiver sensitivity is improved, the link is naturally more robust, and range is extended accordingly since the required SNR is lowered for the same modulation scheme, hence the chances of packet reception is increased. Overall speaking we boost the PHY robustness for all kinds of traffic classes, but the most benefit is observed for the sensitive traffic class such as robot control, where they have the lowest tolerance of bad PHY reliability.

4.3.5.3 CONCLUSION

In this PoC we proved that the wide band jammer has similar impact as increased noise floor, and we showed that, with the ALLR based demapper, RX sensitivity can be improved up to 14 dB, and hence can also better stand wide band jammer. In the future work, we will work towards solution that can also cope with narrow band jammer, the detailed methodology and implementation will be introduced in D3.3, and the experimental PoC will be presented in D5.3.

4.4 INTRA-SUBNETWORK MACRO-DIVERSITY

4.4.1 GENERAL DESCRIPTION

In 6G-SHINE FHG contributes to TC8: Intra-subnetwork macro-diversity. In this context, methods to exploit spatial diversity via the PHY multi-links and via subnetwork devices in range by using cooperative mechanisms are investigated. This will be done in view of the extreme requirements regarding cycle time, latency and reliability for industrial subnetworks.

Cooperative communication relies on the overhearing capabilities of the devices, i.e. devices may overhear packets for other recipients, and use this information for retransmitting the packets. By using network coding these retransmitted packets are encoded in the SNE by combining multiple packets. Packets can then be transmitted either in their native form, or in a combined form. We expect that the introduction of network coding has a huge influence on reliability in wireless communication while keeping the latency low and will be a significant improvement compared to retransmission schemes.

4.4.2 ENHANCED/NEW FUNCTIONALITY

The key question in a subnetwork is, which devices can cooperate. FHG has developed in WP3 (based on D3.1 chapter 3.4.2. “Network Coded Operations” and on ongoing research work) an opportunistic coding and scheduling scheme. This method is based on an analysis of the received coded packets. Based on this, the coding vector of the own transmission is adapted dynamically. As this method looks promising in simulation we want to validate the improvement also with a real-time proof of concept system.

The PoC system will realize a TDMA/TDD communication with ultra-low cycle times (< 1 ms) between multiple devices with new overhearing capabilities on the PHY and MAC Layer and network coding capabilities on the MAC/LLC Layer. Furthermore, the devices have to support PHY multi-links, which allow simultaneous transmissions in two frequency bands.

4.4.3 HIGH LEVEL ARCHITECTURE OF THE IMPLEMENTED POC DEMONSTRATOR

Our PoC is a wireless mesh network of multiple devices which acts as a wireless bridge for UDP-based network traffic. It operates in the 5 GHz ISM band and optionally in the 3.7 GHz band. The PoC takes advantage of network coded cooperation as an efficient way of providing error correction by introducing redundancy on the packet level. Network coded cooperation also adds spatial diversity which should increase the robustness.

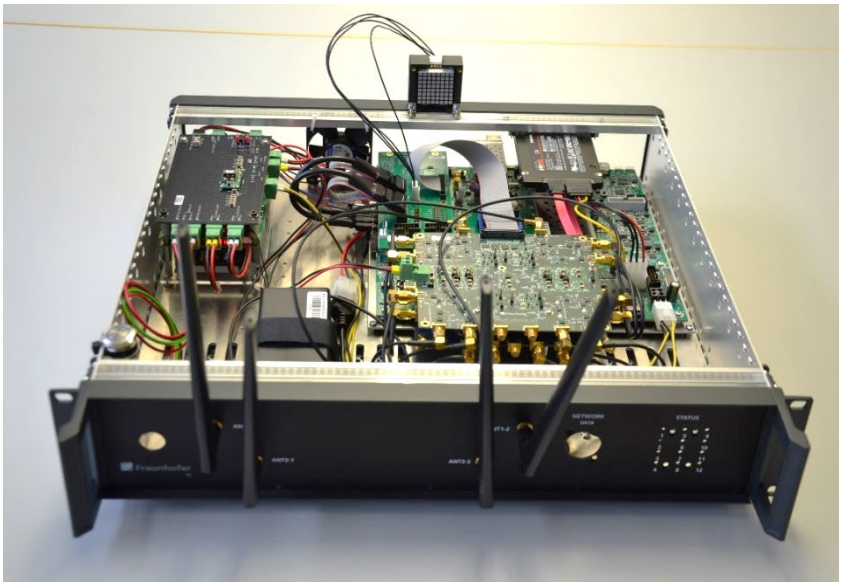

FIGURE 34. 6G-SHINE POC HARDWARE

The PoC consists of multiple devices as shown in Figure 34. Each device has an FMCOMMS5 dual tuner equipped with a wideband RF frontend. The tuner and front end are controlled by an AMD/Xilinx ZCU102 board. Figure 35 shows the internal structure of one device with all its components and mechanical supports.

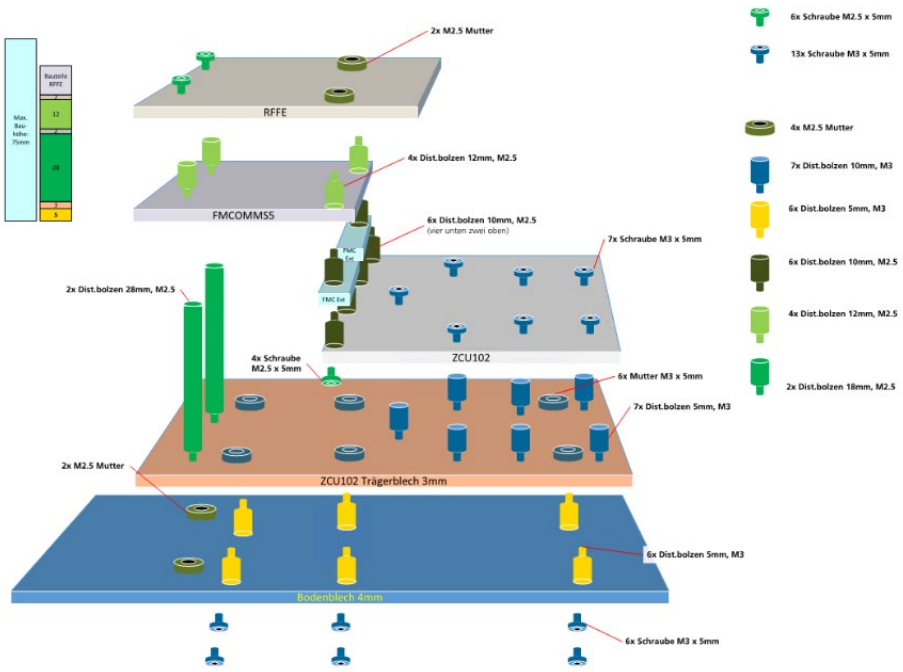

FIGURE 35. MODEL OF THE MECHANICAL STRUCTURE OF ONE DEVICE

The communication is controlled by the ZynQ UltraScale SoC on the ZCU102 board. The dual tuner gets its commands from the FPGA which handles all critical low-level processes such as channel estimation, forward error correction, and the timing for the communication slots.

Packet scheduling as well as network coded cooperation is performed by one Realtime Processing Unit (RPU), which is an ARM Cortex R5 core on the SoC.

4.4.4 DEMONSTRATOR SCENARIO DESCRIPTION

The PoC demonstrator will mainly address industrial use cases like robot control, unit test or visual inspection (defined in WP2 D2.2). The main requirements are:

- Cycle time below 100 µs up to 1 ms for communication in loops
- other communication cycles from 10 up to 100 ms
- Data packet size from 100 up to 300 Bytes
- Resulting data rate is approx. 1..2 Mbit/s (in case of video up to 80 Mbps)
- probability of having two consecutive errors < 10^{-6}
- 20 to 50 SNEs
- Movement speed of nodes none or up to 20 m/s

The PoC will comprise a central HC which controls the communication and up to 6 SNE, starting with 2 SNEs. KPI like packet errors, packet error rate, packet loss rate (after error control), latency or cycle time will be logged.

4.4.5 RESULTS

4.4.5.1 BASELINE RESULTS

The baseline test was performed by a previous release of the UWIN PoC. In this version the devices communicated in a cyclical TDMA scheme with one blind retransmission per link. The system communicates simultaneously on

two channels. Each retransmission is performed on the alternate channel in order to harness frequency and time diversity.

We performed a range test and multiple interference tests over the air. In each test we measured the CRC error rate and the telegram loss rate. Since we use blind retransmissions, a telegram is lost if and only if the first transmission and the retransmission fail.

4.4.5.1.1 Interference tests

All interference tests were performed in a shielded radio test chamber to avoid unaccounted interference from the environment. The network under test consisted of two nodes which communicated with each other continuously in a blind retransmission TDMA scheme with 125 µs cycle time and a packet size of 32 bytes. Interference was created using two PCs with WiFi cards, one as an access point and one as a station. The PCs were equipped with step attenuators to allow for different interference levels. Both PCs and attenuators were placed outside of the chamber; only the antennae were placed inside. Figure 36 shows the physical setup of the interference tests. The nodes and the antennae of the interferers inside of the chamber are arranged in a rectangle shape with an edge length of 150 cm.

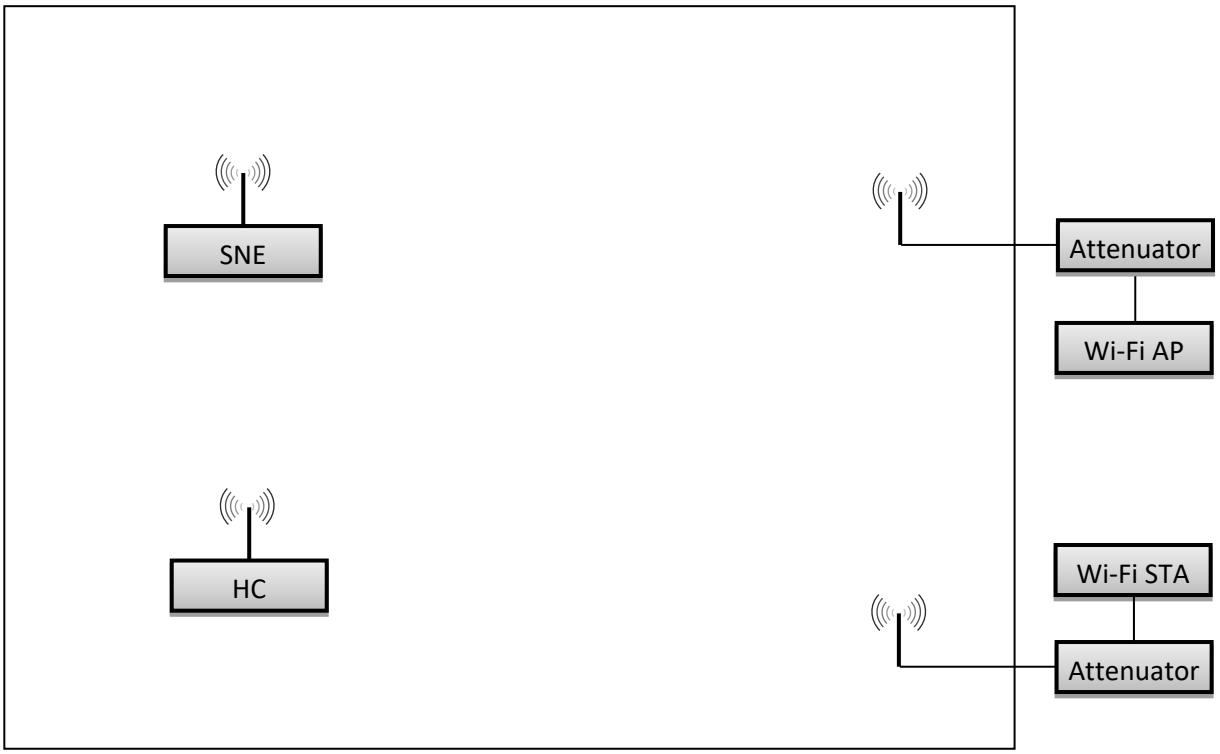

FIGURE 36. SETUP OF THE INTERFERENCE TESTS

During the tests interference is generated with iperf3 using two traffic models. Traffic model 1 (TM1) is modelled resembling the statistical properties of Wi-Fi traffic in an industrial environment which we captured in an earlier project. Traffic model 2 (TM2) is a stress test which transmits as many Wi-Fi packets as possible. Since the channel bandwidth of UWIN and the interfering Wi-Fi is both 20 MHz we used the channel raster of the Wi-Fi standard also for the UWIN system. The attenuation of the Wi-Fi interferers is varied symmetrical at the access point and the station. Each interference test is performed for exactly 17 minutes which allows for a minimum detected telegram loss rate of 10^{-7}.

4.4.5.1.2 Adjacent Channel Interference

In this test case the interferer is transmitting on a frequency close to but not overlapping the frequency of one of the two channels. Figure 37 shows the frequency band of this interference scenario.

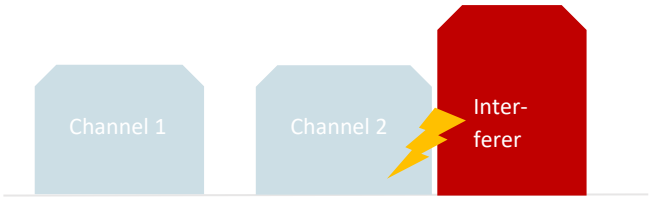

FIGURE 37. FREQUENCY BAND SETUP FOR ADJACENT CHANNEL INTERFERENCE TEST CASE

This test case resembles operation in a controlled environment with frequency band planning and only causes slight interference on one channel. Table 6 shows the resulting error rates for this test case.

TABLE 6. ERROR RATES FOR ADJACENT CHANNEL INTERFERENCE TEST CASE

Interferer attenuation in dB	TM1 CRC Error Rate	TM1 Packet Loss Rate	TM2 CRC Error Rate	TM2 Packet Loss Rate
0	0	0	9.3e-8	0
5	0	0	0	0
10	0	0	0	0
20	0	0	0	0

4.4.5.1.3 Dual adjacent channel interference

In this test case the interferer is transmitting on a frequency between both channels but not overlapping either of them. Figure 38 shows the frequency band of this interference scenario.

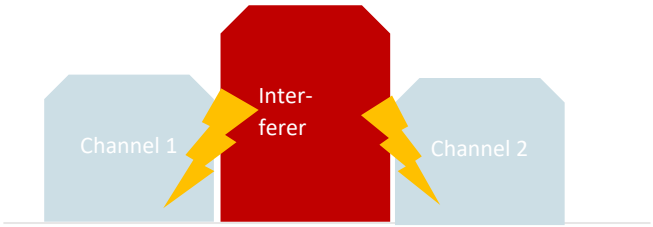

FIGURE 38. FREQUENCY BAND SETUP FOR DUAL ADJACENT CHANNEL INTERFERENCE TEST CASE

This test case resembles operation in a controlled environment with frequency band planning and only causes slight interference affecting both channels at the same time. Table 7 shows the resulting error rates for this test case.

TABLE 7. ERROR RATES FOR DUAL ADJACENT CHANNEL INTERFERENCE TEST CASE

Interferer attenuation in dB	TM1 CRC Error Rate	TM1 Packet Loss Rate	TM2 CRC Error Rate	TM2 Packet Loss Rate
0	1.1e-3	0	1.54e-5	0
5	0	0	0	0
10	0	0	0	0
20	0	0	0	0

4.4.5.1.4 Co-channel interference

In this test case the interferer is transmitting exactly at the frequency of one of the two channels completely overlapping it. Figure 39 shows the frequency band of this interference scenario.

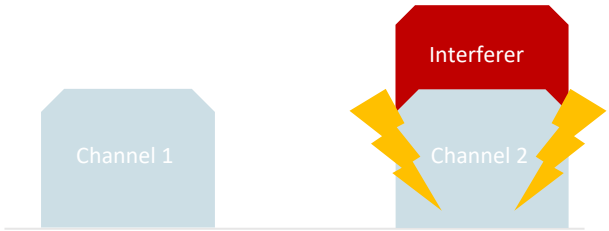

FIGURE 39. FREQUENCY BAND SETUP FOR CO-CHANNEL INTERFERENCE

This test case resembles operation in an uncontrolled environment with heavy interference on one of the two channels. It shows how well retransmissions on the second channel can mitigate packet losses on the primary channel. Table 8 shows the resulting error rates for this test case.

TABLE 8. ERROR RATES FOR CO-CHANNEL INTERFERENCE TEST CASE

Interferer attenuation in dB	TM1 CRC Error Rate	TM1 Packet Loss Rate	TM2 CRC Error Rate	TM2 Packet Loss Rate
0	6.7e-2	0	3.6e-1	0
5	1.0e-1	0	3.9e-1	0
10	1.5e-1	0	4.0e-1	0
20	2.6e-2	0	4.7e-1	0

4.4.5.1.5 Range Test

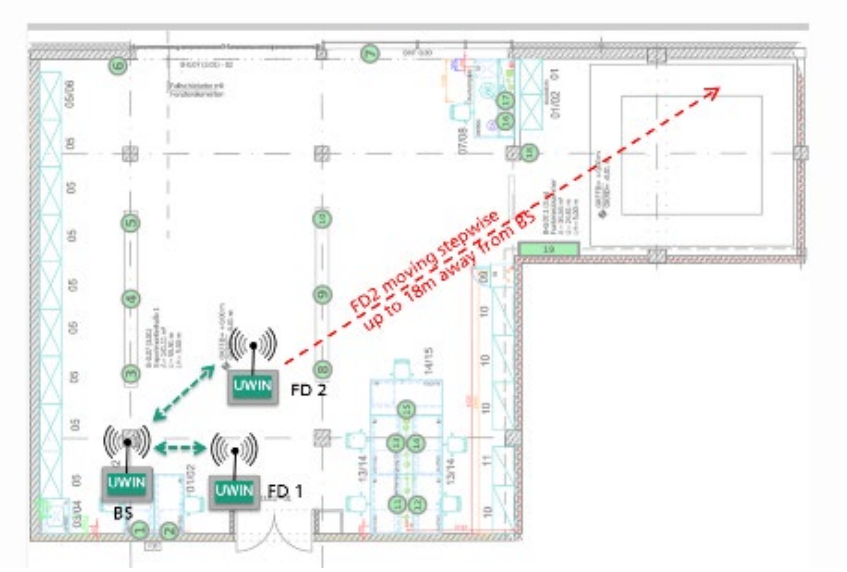

FIGURE 40. RANGE TEST SETUP IN THE RF LAB

The range test was performed in the RF lab to test the reliability of the communication over a greater distance. Since the maximum transmit power of the UWIN nodes is 10 dBm the maximum reliably usable distance between two UWIN nodes is specified as 20 m. The maximum usable distance in the lab was 17 meters. During the test two nodes communicated with each other. One node remained stationary while the other node was moved to specific distances. Figure 40 shows the test setup. At each distance CRC errors and packet losses were recorded for 17 minutes. Table 9 shows the resulting error rates.

TABLE 9. ERROR RATES FOR RANGE TEST

Distance in m	CRC Error Rate	Packet Loss Rate
1	0	0
2	0	0
5	0	0
10	4.7e-1	0
15	6.0e-5	0
17	2.8e-4	0

4.4.5.1.6 Conclusion

We could show that the system performs reliably up to a range of 17 meters and is robust against interference. KPIs are a cycle time of 125 µs, a telegram loss rate of 10^{-8}, and a payload size of 32 bytes. Since blind retransmissions are rather inefficient the number of devices is limited to 8 for the lowest latency.

4.4.5.2 PROPOSED TC RESULTS VS THE BASELINE

The most promising cooperative communication methods in terms of reliability were identified in WP3 (initial results in D3.1, section 3.4.2.1). For each communication scenario, which comprises the number of SNEs as well as the required traffic patterns, a distinct global resource allocation table is calculated. From this resource allocation table, a unique configuration is derived for each node. This configuration determines, e.g., in which slots a node transmits and from which packets it can choose for assembling a network encoded packet. To ensure that the PoC demonstrator behaves as similarly as possible to the simulated network, the individual nodes must be configured

as in the simulation environment. For this purpose, a flexible configuration interface is required for the nodes of the PoC demonstrator. A first version of this configuration interface was developed and is currently being tested.

We expect that the implemented TCs will increase the reliability in all communication scenarios compared to the baseline. Due to the simplifying assumptions made during modelling, it is difficult to predict the increase in reliability accurately. However, we expect that the increase in reliability is significant for communication scenarios in which obstacles are involved.

4.4.5.3 MAPPING OF ACHIEVED RESULTS TO RELEVANT USECASE

The PoC set up addresses industrial use cases like robot control. As soon as the PoC systems support multi-link transmission, the network-coded cooperation procedures developed in simulation (see WP3 D3.1 and ongoing research) will be implemented as real-time software and are to be tested in practice in the next step. We will evaluate situations in which a link is disrupted by obstacles, for example. For evaluation purposes, KPI will be collected and derived, which can show in particular the improvement in reliability.

4.4.5.4 CONCLUSION

FHG is currently developing a new hardware platform for the PoC system based on a Zynq UltraScale+ MPSoC ZCU102 and a dual tuner RF frontend to support multilink transmission. Hardware work is well advanced, and MAC and LLC implementation work is currently underway. MAC and LLC should support network coded cooperation (NCC) in the PoC, which has shown promising results in simulation in WP3.

As a basis for comparison, measurements were carried out on a precursor system. These show that blind retransmission, i.e. sending the packets twice, is generally suitable under LOS conditions. With the final PoC in D5.3 we will show opportunistic NCC, with which we expect reliable transmission even with disturbed single links between a HC and a SNE.

4.5 CENTRALIZED RRM

4.5.1 GENERAL DESCRIPTION

In the previous deliverable [30], we introduced concepts for a wireless-connected E/E architecture that operates as a subnetwork, such as within a vehicle. However, a new challenge has emerged: potential interference scenarios, particularly when multiple vehicles are in close proximity. To address this, we propose a centralized radio resource management approach to efficiently coordinate resources across multiple vehicles. In this deliverable, we delve deeper into this concept, introducing new architectural elements and presenting an initial implementation of the proposed framework. We share partial results from this implementation and outline future directions for the development of the final PoC.

This proposed PoC is structured into three key steps, which we elaborate upon in detail. First, we establish an in-vehicle communication infrastructure by adapting components of the Electric/Electronic (E/E) Architecture for wireless transmissions. This creates a dedicated in-vehicle subnetwork, managed by a Subnetwork Controller (SNC). Second, we integrate this short-range, low-power wireless connectivity into a broader, parent network. Finally, we develop methods within the parent network to dynamically manage communication resources across multiple subnetworks, utilizing contextual information such as vehicle positioning.

The scenario, as depicted in Figure 41, represents an environment where a parent 6G network manages interference across multiple in-vehicle subnetworks.

For the in-vehicle subnetwork, we adapted the automotive CAN protocol to Wi-Fi using Commercial Off-The-Shelf (COTS) hardware with OpenWRT [10]. The parent network setup leverages a 5G Open-RAN-based architecture [7]. In this configuration, latency performance may be affected due to the listen-before-talk (LBT) mechanism [8]. Ideally, optimal performance is achieved when vehicles approaching each other utilize orthogonal frequency resources, minimizing interference.

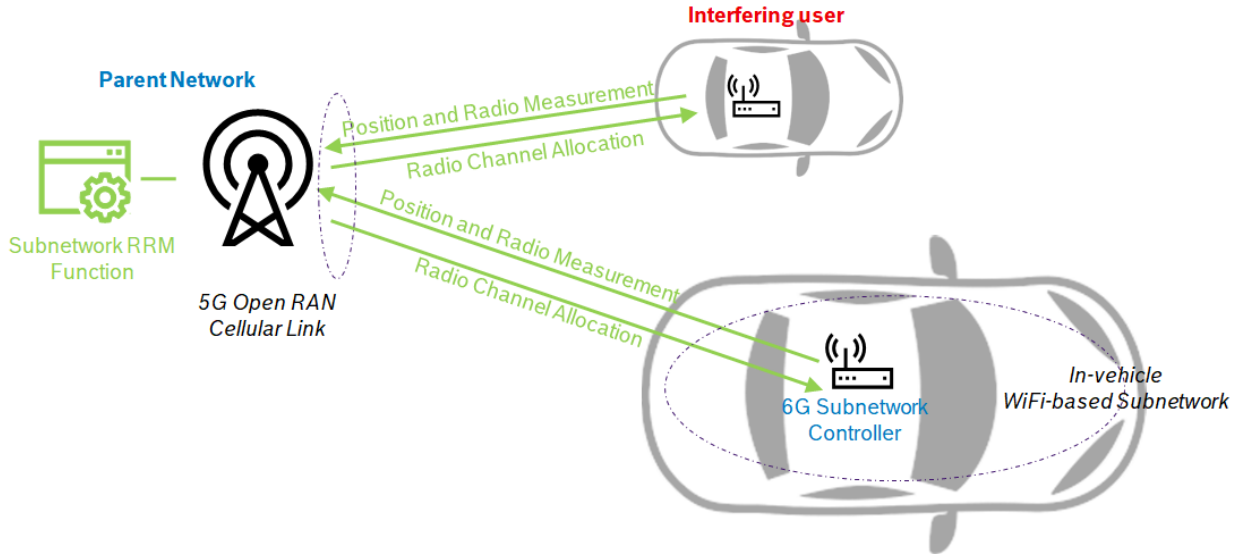

FIGURE 41. OVERALL POC DESCRIPTION

4.5.2 ENHANCED/NEW FUNCTIONALITY

This PoC introduces several novel functionalities, which can be outlined as follows:

1. **Parent Network RRM:**

To support the design outlined in Figure 41, the parent network introduces two key functionalities:

- Monitoring non-3GPP networks: This involves tracking the Wi-Fi network's performance metrics (e.g., SINR, channel utilization, signal strength) along with the vehicle's positioning.

- RRM of non-3GPP networks: The system provides commands, such as channel switching, to manage Wi-Fi resources when interference risks arise.

To achieve this, we introduced a new entity at the parent network, called the non-3GPP Subnetwork Management Function (N3SMF), as depicted in Figure 42. Unlike the existing N3IWF defined by 3GPP [13], our solution goes beyond enabling NAS services over WLAN. It actively monitors and manages Wi-Fi services through the 5G network, exposing key functions to the 3GPP architecture. This allows the 5G Core Network (CN), integrated into the 5G Service-Based Architecture, to take on the central RRM role for SNCs.

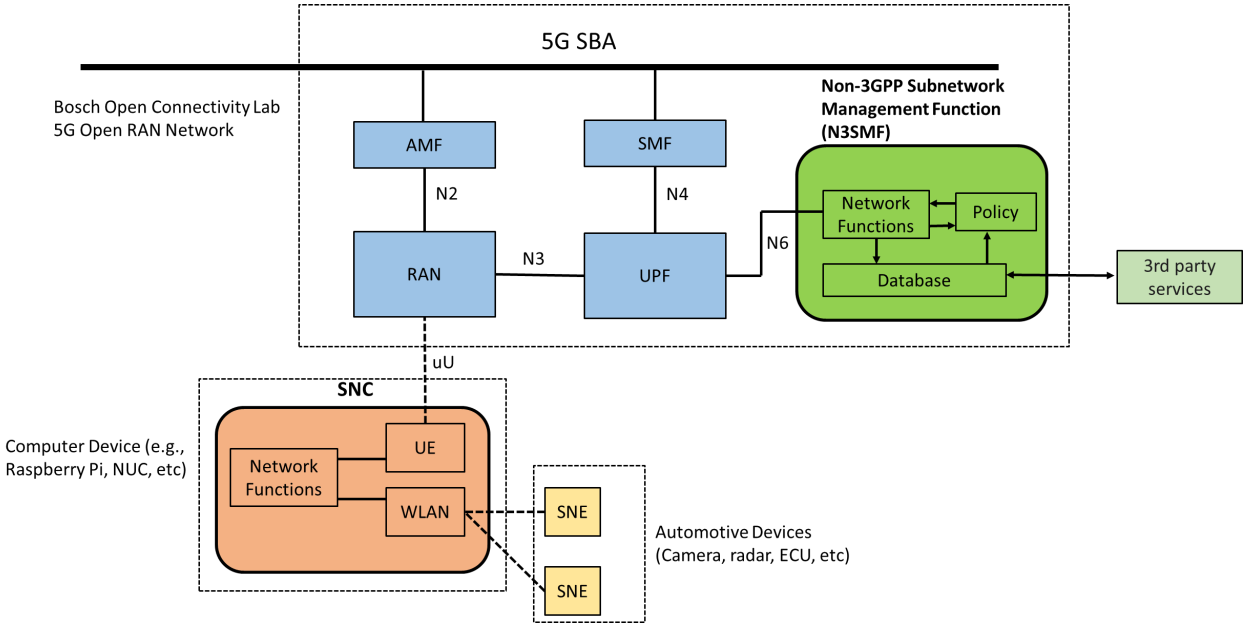

FIGURE 42. INTRODUCTION TO N3SMF AS A KEY ENTITY TO MANAGE NON-3GPP SUBNETWORKS FROM THE CORE NETWORK

2. Subnetwork Controller (SNC):

The SNC is designed to act as a 5G user equipment (UE) while providing short-range WLAN access point services, all managed by the parent network, as depicted in Figure 42. Implemented on a Raspberry Pi, the SNC incorporates service APIs to:

- Collect Wi-Fi modem status (e.g., signal strength, channel occupancy) periodically and report it to the 5G CN.
- Enable Wi-Fi channel reconfiguration through the 5G CN. The channel switch announcement functionality [9] is used to broadcast the new channel configuration via beacons from the SNC to all subnetwork elements connected, with the change scheduled for the next N beacons.

3. Indoor Positioning Service:

While GPS data is typically used for positioning in automotive applications, indoor environments such as factories require more precise localization. To address this, we implemented a solution based on Ultra-Wideband (UWB) technology, where positioning is determined using a Graph Neural Network (GNN). This approach provides sub-5 cm accuracy without the need for line-of-sight from all anchors. This method has been accepted for publication at IEEE Globecom 2024, where further details are depicted in Figure 43 and available in [15]. The calculated positions are then reported to the N3SMF at the parent network.

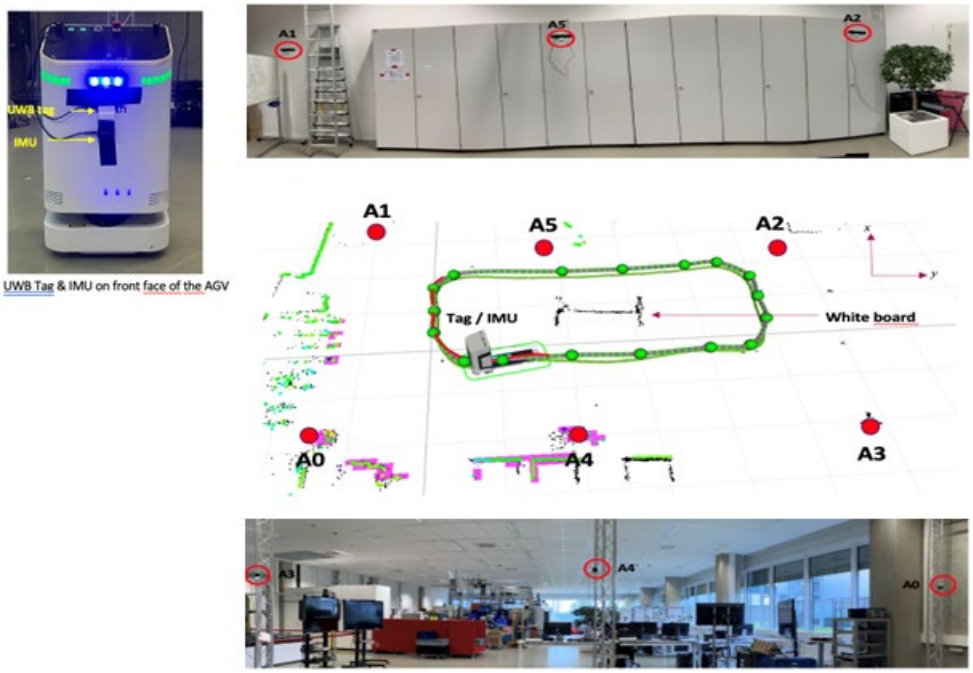

FIGURE 43. INDOOR POSITIONING ALGORITHM DEVELOPED FOR INDOOR SCENARIOS WHEN MANAGING IN-X SUBNETWORKS.

4.5.3 HIGH LEVEL ARCHITECTURE OF THE IMPLEMENTED POC DEMONSTRATOR

Details of the PoC setup are illustrated in Figure 44. In this setup, we integrate NXP Smart Radar (Cocoon) automotive radar sensors [12] as subnetwork elements The Subnetwork Controller manages the wireless communication between the SNEs and the vehicle's central computer, where the radar data is processed.

When other vehicles are nearby, the communication may face interference, potentially compromising the radar data processing on the vehicle computer, as the interference impacts the data transmitted from SNEs. To mitigate this, the SNC receives RRM commands from the parent network, triggered by the non-3GPP Sensing Management Function.

Automotive radar technology poses unique challenges for wireless communication due to its strict latency requirements, particularly in closed-control loops. This makes it an ideal domain for research and development on wireless communication performance and optimization. Additionally, the proposed methodology can be extended to other use cases, such as automotive wireless cameras and other relevant scenarios.

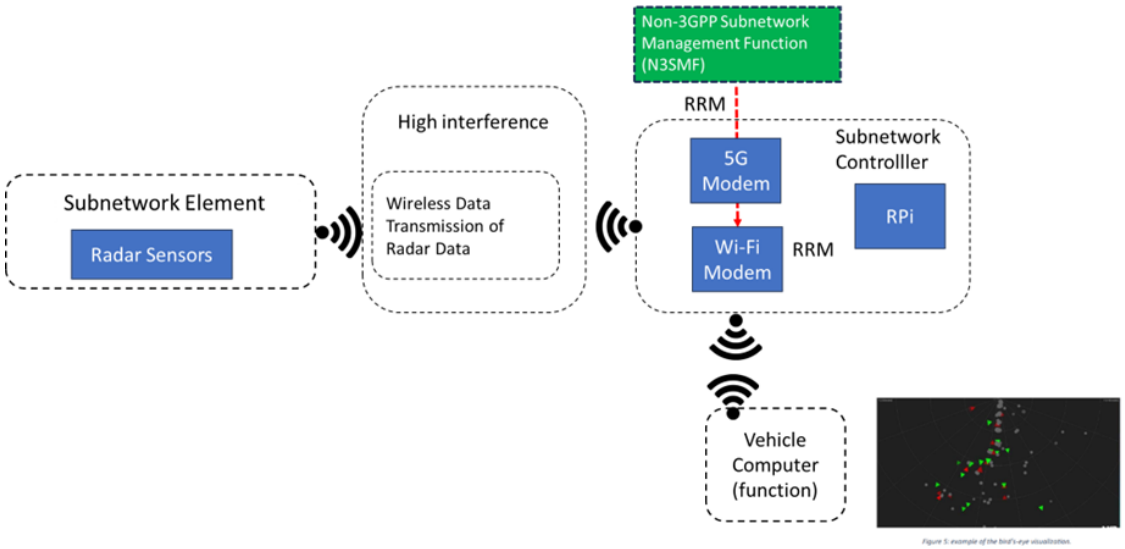

FIGURE 44. HIGH-LEVEL ARCHITECTURE OF THE PROPOSED POC.

4.5.4 DEMONSTRATOR SCENARIO DESCRIPTION

The scenario demonstration, as depicted in Figure 45, involves configuring automotive components on two adjacent moving tables, each representing the wireless in-vehicle application, which was initially illustrated in Figure 41. The demonstration of the parent network's RRM functionality is conducted in two main steps:

Initial Scenario (No RRM Enabled): The two tables are brought closer together, and their positions are evaluated at the parent network. At this stage, with no RRM enabled, two main effects are expected: At the parent network, the proximity of the tables and high latency will be reported by each SNC. On each table, the screens should display the impact of interference on the application's performance, such as lost video or radar frames.

Scenario with RRM Enabled: In the second step, the tables are again brought closer, but this time with RRM enabled. The system triggers the RRM command based on proximity, and we expect to see no interference effects as the tables approach each other. Additionally, the demonstration will highlight the reaction to the RRM decision

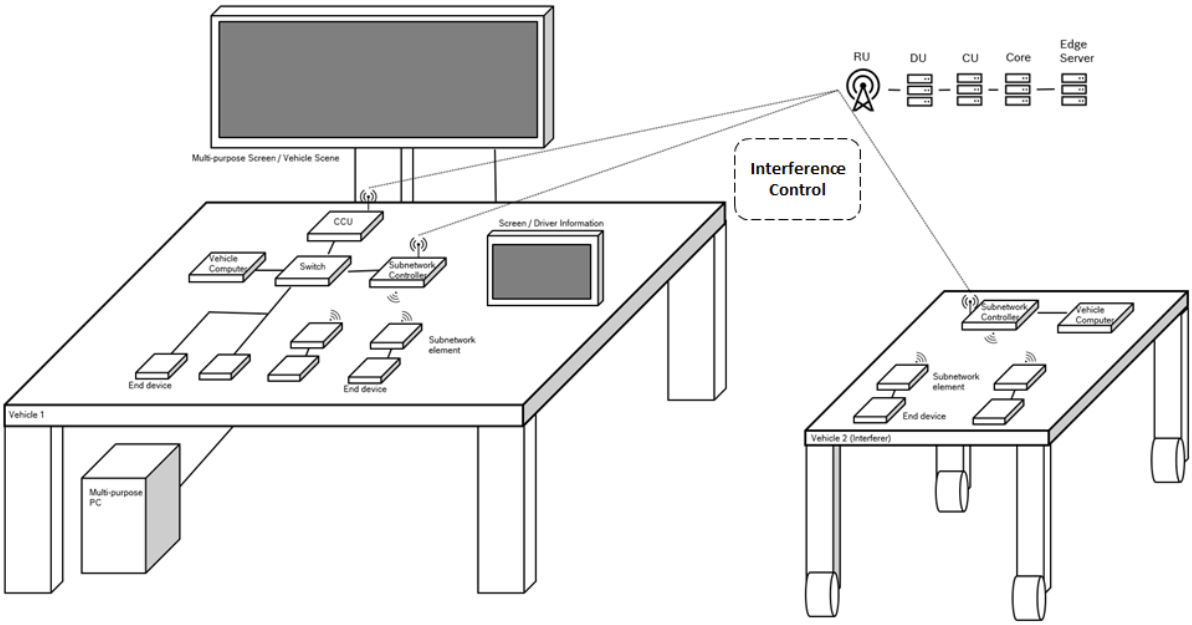

FIGURE 45. POC DEMONSTRATION SCENARIO AND SETUP.

from both the network and application perspectives, including whether any information is lost during the RRM procedure.

4.5.5 RESULTS

4.5.5.1 BASELINE RESULTS

The baseline for our comparison is a wired communication setup, specifically using automotive Ethernet under the TCP/IP protocol. Figure 46 and Figure 47 show results obtained by capturing traffic from the connected radar device using Wireshark [17]. Key outcomes in this scenario include an average packet rate of 150 packets per second and a round-trip time << 1 ms, with occasional peaks up to 1.5 ms. These measurements reflect the network path from the radar sensor to the central computing unit and back to the sensor, emulating a control loop scenario.

It is important to note that in this setup, the radar data is compressed at the hardware level. However, this may not always be feasible, particularly when aiming for sensor fusion, where data from multiple sources is aggregated. Without compression, radar data would require significantly higher network capacity — a consideration that will be addressed in the final deliverable.

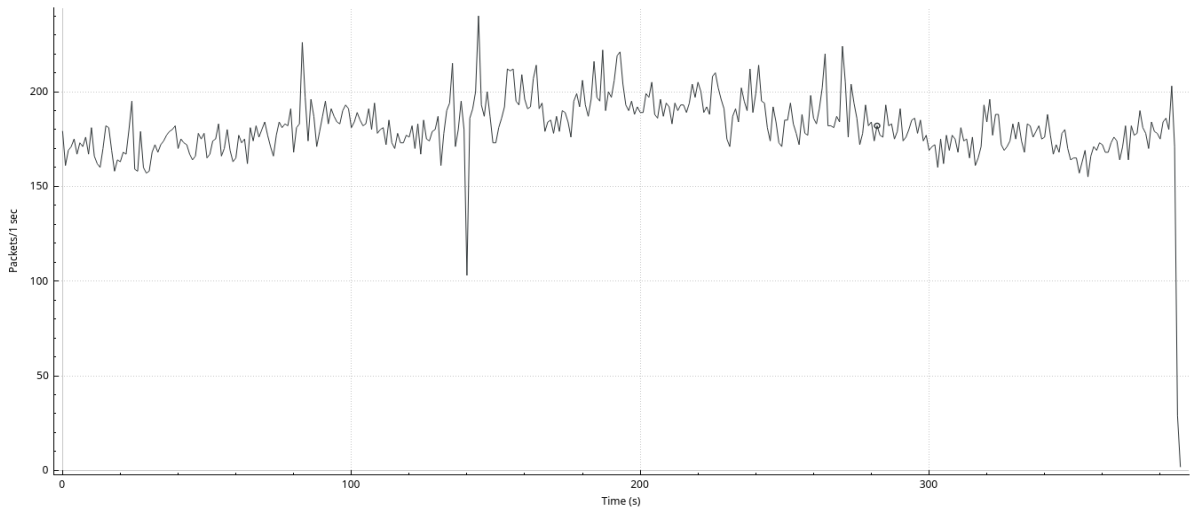

FIGURE 46. RADAR DATA THROUGH AUTOMOTIVE ETHERNET OVER TIME (BASELINE).

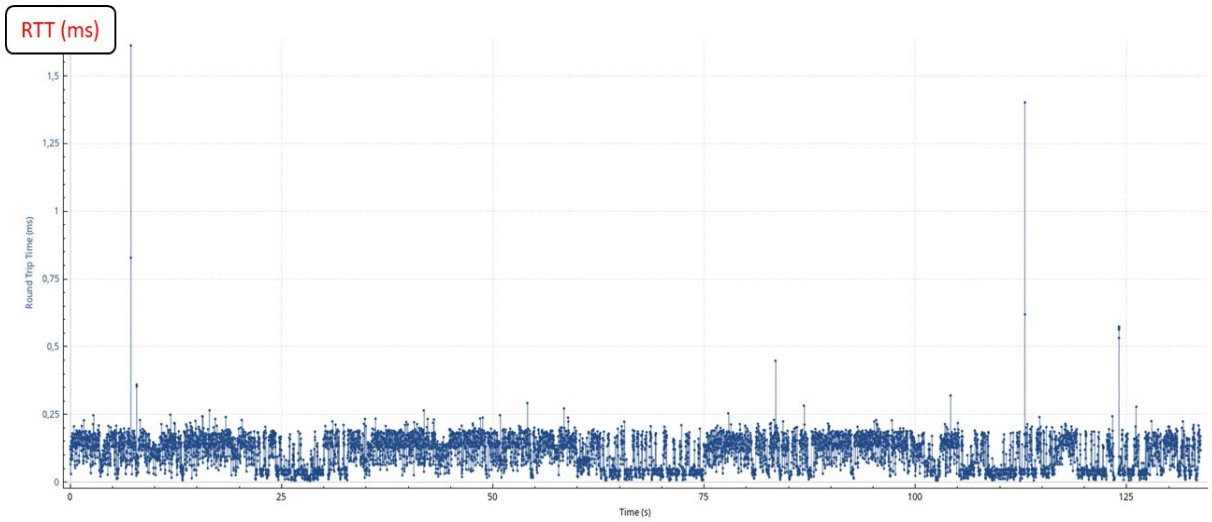

FIGURE 47. RTT OF RADAR DATA THROUGH AUTOMOTIVE ETHERNET OVER TIME (BASELINE).

4.5.5.2 PROPOSED TC RESULTS VS THE BASELINE

Figure 48 and Figure 49 summarize partial results from evaluating the proposed PoC. We tested a high-interference scenario, where two subnetworks are in close physical proximity, operating on the same Wi-Fi channel and running similar radar applications, as depicted in Figure 45. Our analysis focused on application and network behaviour before and after the RRM command from the 5G parent network. Three main aspects are highlighted:

1. **Pre-RRM Interference Effects:**

In Figure 48 , we observe frequent TCP retransmissions due to interference, which likely contribute to the round-trip time (RTT) peaks shown in Figure 49. The Subnetwork Controllers monitor this interference and relay network status updates to the parent network via the uU interface.

2. **Centralized RRM Command Processing:**

The non-3GPP Sensing Management Function aggregates information on channel conditions and subnetwork status (e.g., signal quality) and, as represented by the red vertical line in both plots, issues RRM commands to the SNCs to mitigate interference. Notably, the channel transition occurs without disrupting real-time data transmission, resulting in a seamless channel reconfiguration that does not adversely affect application performance.

Post-RRM Performance Improvement:

After the RRM command Figure 48 and Figure 49 indicate a reduction in TCP retransmissions and the elimination of RTT peaks. This achieves a performance level comparable to the wired baseline, meeting the target for reliable in-vehicle communication modules.

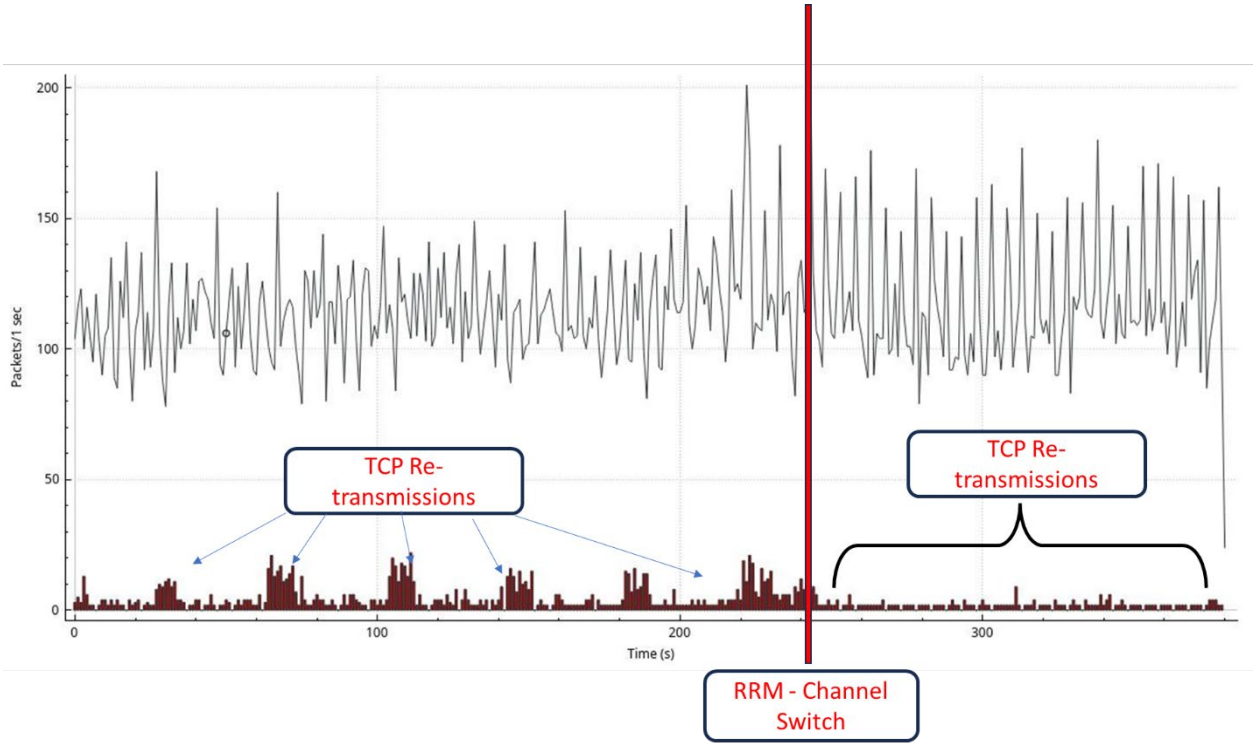

FIGURE 48. RESULTS FOR THE WIRELESS RADAR COMMUNICATION.

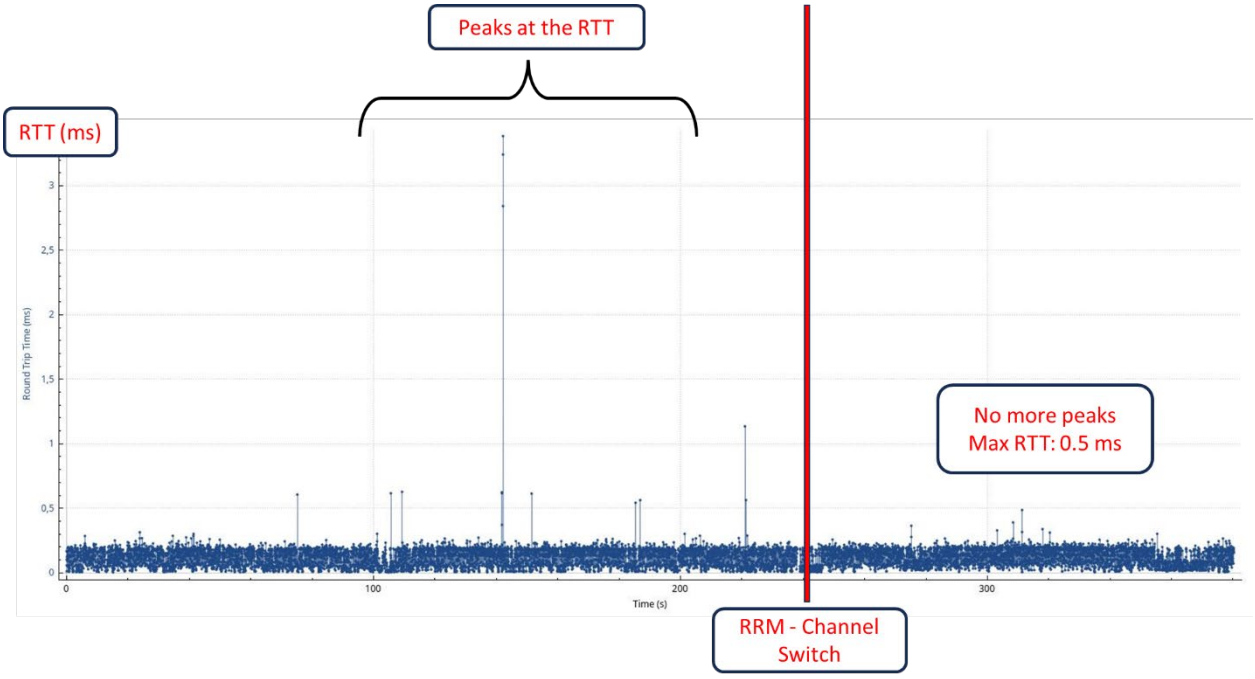

FIGURE 49. RTT RESULTS FOR THE WIRELESS RADAR COMMUNICATION. BEFORE AND AFTER RRM.

4.5.5.3 MAPPING OF ACHIEVED RESULTS TO RELEVANT USECASE

The obtained results align closely with the automotive use-case Inter-subnetwork Coordination, which involves collaboration between subnetworks in both intra- and inter-vehicle communications. This use-case is conceptually

illustrated in Figure 41. Our partial results are also consistent with Tables 9 and 10 in Deliverable D2.2 [28] where, under RRM conditions, the performance of domain functions - such as body electronics, infotainment systems, and the Human-Machine Interface (HMI) - achieves a level comparable to that of automotive Ethernet through wireless connectivity.

4.5.5.4 CONCLUSION

This PoC demonstrates the feasibility of establishing a reliable wireless in-vehicle E/E architecture using Wi-Fi-enabled subnetworks managed by a 5G Open-RAN-based parent network. Through a combination of monitoring, RRM commands, and centralized management via the non-3GPP Sensing Management Function, we successfully mitigated interference, maintaining application performance at levels comparable to wired automotive Ethernet. The results validate the effectiveness of our approach for real-time inter-subnetwork coordination, a foundational step toward enabling advanced automotive functions such as body electronics, infotainment, and Human-Machine Interface over wireless channels.

For deliverable D5.3, we plan the following steps:

1. **Integration of Indoor Positioning Services:**
   We will incorporate the developed indoor positioning service into the tabletop PoC setup, adding context-based RRM capabilities. This will involve optimizing the trained AI model to operate efficiently on IoT hardware with limited computing and energy resources, potentially by simplifying the neural network architecture.

2. **Dashboard for Enhanced Visualization:**
   To provide comprehensive insights into the system's performance, we will develop a dashboard to visualize the parent network's decision-making for each subnetwork. This dashboard will highlight the role of the N3SMF and display application behaviour under both RRM-enabled and RRM-disabled conditions.

3. **Inclusion of Automotive Camera Subnetworks:**
   We plan to expand the PoC by adding subnetworks that wirelessly connect automotive cameras. This addition will increase network requirements and introduce new challenges, further underscoring the advantages of the N3SMF's RRM functionality.

These next steps will be essential in refining and demonstrating our approach, forming a core part of the progress to be presented in the final deliverable.

4.6 CENTRALIZED/DISTRIBUTED INTERFERENCE MANAGEMENT

4.6.1 GENERAL DESCRIPTION

Apart from centralized radio resource management, where resources such as spectrum and power are governed under a 6G parent umbrella station, distributed radio resource management allows subnetworks to make autonomous decisions based on local learning or by exchanging information with neighbouring subnetworks.

This PoC builds upon the work initiated in WP4, where a distributed radio resource management solution based on Graph Neural Networks (GNNs) and message passing was explored through simulations. The solution relies on centralized training conducted by the 6G parent network to learn interference patterns and generate power control models. These models are then deployed in a distributed manner, enabling subnetworks to make autonomous decisions about their transmit power based on local information and limited message exchanges with neighbouring subnetworks. This approach allows for efficient power allocation and interference management without requiring constant coordination from a centralized controller while it remains adaptable to changes in network topology, such as the addition of a new subnetwork.

Unlike the simulation-based results, which are part of the WP4 deliverables, this PoC advances the work into a practical over-the-air setup, providing a real-world testing environment to validate the proposed scheme. Furthermore, while the previous WP5 deliverable, D5.1, focused on outlining the PoC design and its hardware/software requirements, the work presented here consists of the first set of results derived from the implementation, validating the scheme's practical feasibility.

4.6.2 ENHANCED/NEW FUNCTIONALITY

The PoC enables multiple subnetworks to coexist within the same frequency channel and bandwidth, achieving high overall throughput and minimal PER. This capability relies on controlling the power of data transmission, where power levels are adjusted based on the conditions of neighbouring networks. These conditions are a result of information exchange between networks and channel estimation.

An AI/ML process within the HC node makes the power transmission decisions, as shown in Figure 50. A centralized process hosted on the parent network coordinates these processes, determining when the HCs can transmit information with specific pilot transmit power. During this time, the SNEs conduct channel estimation and relay their results to their respective HC, enabling the AI/ML process to determine the optimal data transmission power.

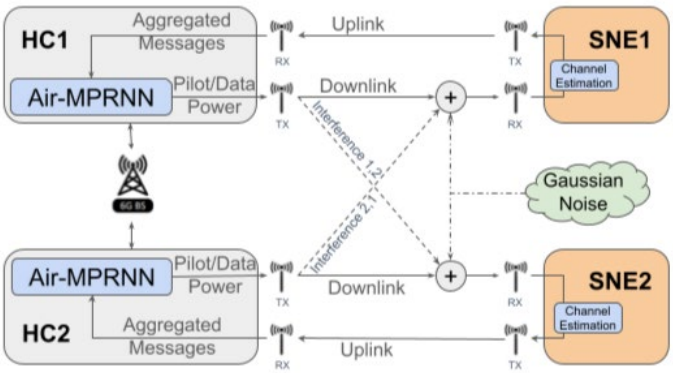

FIGURE 50. THEORETICAL PRESENTATION OF THE POC.

4.6.3 HIGH LEVEL ARCHITECTURE OF THE IMPLEMENTED POC DEMONSTRATOR

The PoC includes two pairs of an HC node and an SNE. Each pair has two USRP B210 SDR devices [19] , and a host machine connects to each device using USB3 data cables, as shown in Figure 51, and executes the srsRAN software,

an O-RAN open-source software suite [20]. Specifically, the setup virtualizes each HC node as a gNB and each SNE as a UE. The gNB application integrates the developed solution, which performs interference management.

This PoC places interference management on the downlink channels, so downlink communications occur over the air using omnidirectional antennas, while uplink communications run through shielded cables. This setup enables the pairs to experience interference and supports the message passing needed for interference management.

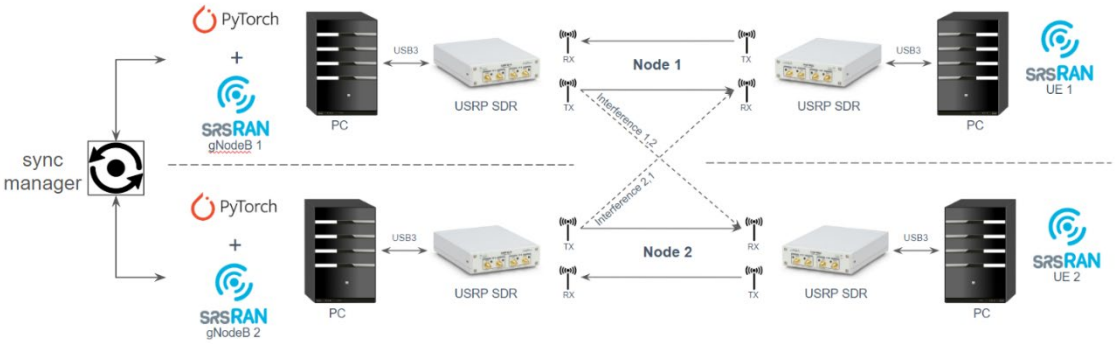

FIGURE 51. POC DEMONSTRATION CONSISTING OF 4 SDR DEVICES CONNECTED WITH HOST MACHINE

The algorithm used for interference management is the Air-MPRNN framework, presented in [21] . The framework is a graph neural network that utilizes message-passing mechanisms to exchange data between the graph's nodes. Each node represents a pair of HC/SNE, and each graph's edge is the interference between the pairs. Each node passes through four phases to calculate the optimal data transmission power that minimizes the interference to the neighbouring pairs, as shown in Figure 52.

The first phase is message generation, in which the node creates a message for the rest of the nodes depending on its previous state. Following is the message-passing phase, where each node receives the neighbouring messages and aggregates them. With the aggregated message, each node updates its internal state and uses them to perform recursively the next message generation. In the last phase, each node outputs the calculated optimal transmission power. The message generation, the state update, and the output calculation phases take place using small Multi-Layer Perceptron (MLP) networks.

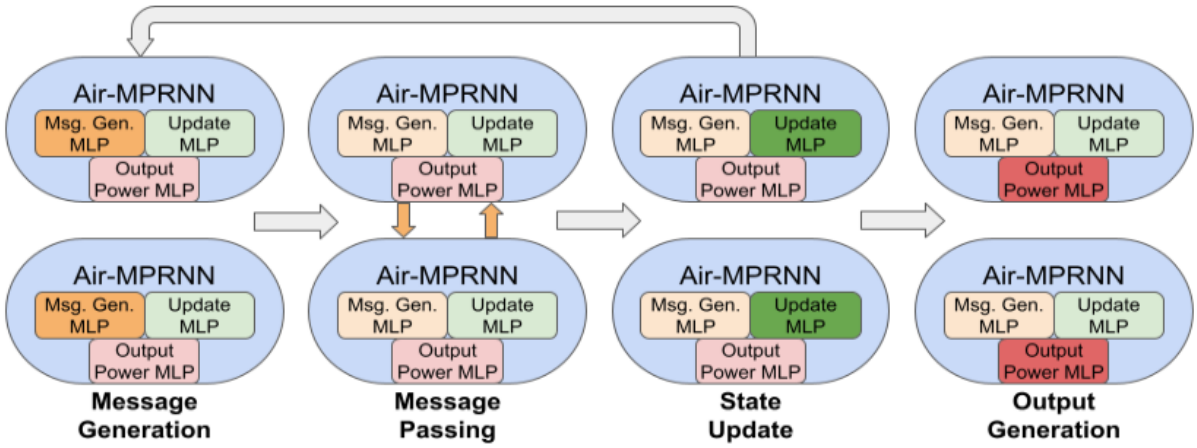

FIGURE 52. AIR-MPRNN FRAMEWORK'S PHASES.

The development of Air-MPRNN layers for each GNN node uses the PyTorch library [22]. A separate process executes the node implementation and exchanges data with the srsRAN software through interprocess communication using ZMQ sockets [23]. The GNN generates messages mapped as pilot transmit power, which controls the transmission power of the Synchronization Signal Block (SSB) [24]. All gNBs broadcast this block, allowing UEs from different pairs to receive it.

The SSB provides Synchronization Signals (SS), which let UEs synchronize over the air without additional time and frequency synchronization devices. This synchronization enables UEs to obtain the CSI along with the generated message. For this, the system uses a simple scheduling policy. The SSB signal's periodicity is set to 5 ms, meaning each frame broadcasts it twice, with each broadcast coming from a different gNB, as shown in Figure 53. This approach ensures the avoidance of a collision or interference during SSB transmission.

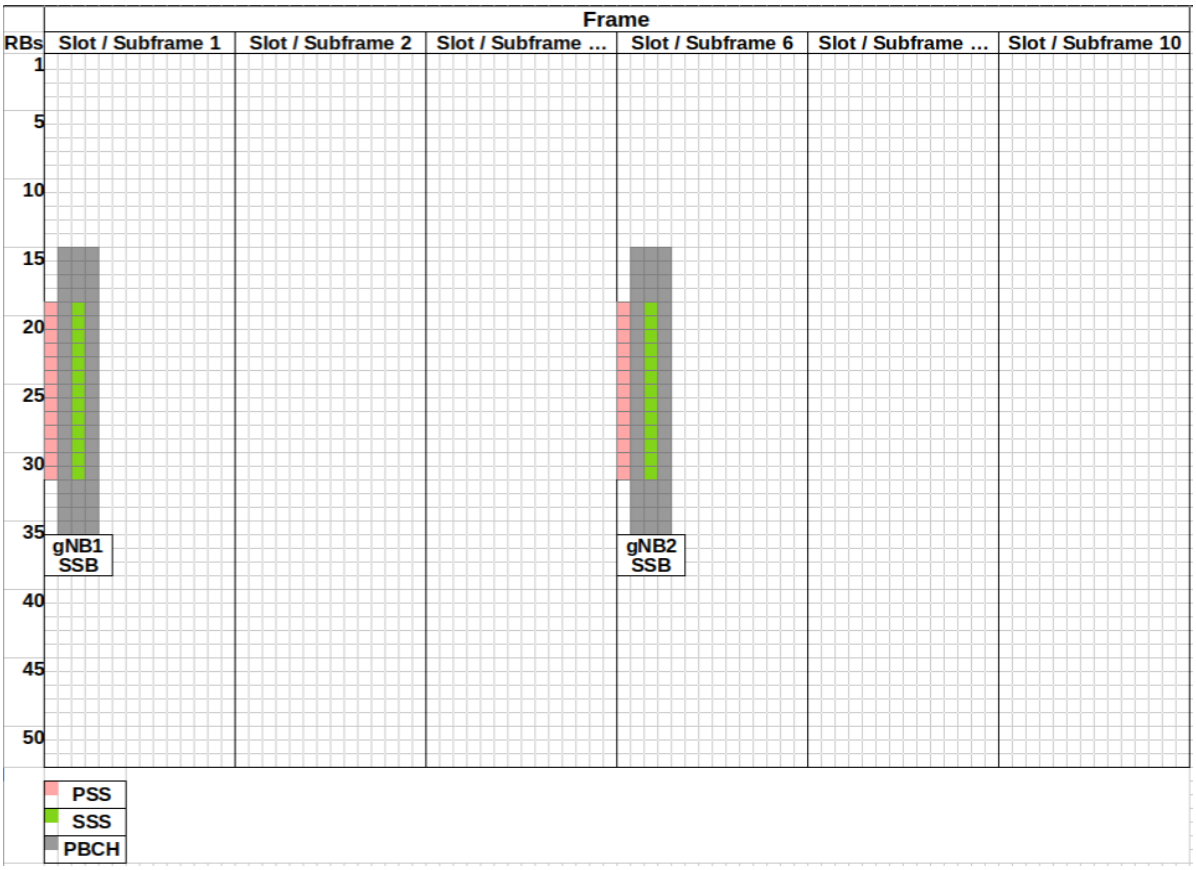

FIGURE 53. 5G DATA FRAME WITH TWO SCHEDULED SSBS ON DIFFERENT SLOTS OF THE RESOURCE GRID FOR DIFFERENT GNBS

A concurrent process, representing the sync manager shown in Figure 51, ensures proper coordination among all GNN nodes. This process acts as the centralized unit hosted on the parent network, dictating the specific frame on which the message passing phase should be scheduled and executed.

The information, containing the CSI and the received message, feeds back to the GNN node. This way, the node can pass to the consequential phases of its internal state update and the data transmission power calculation. The output controls the power of the PDSCH signal [24] , which carries the downlink data packets. After that, the overall process repeats itself to keep up to date with the optimal transmission power that minimizes the interference of the given channel condition.

4.6.4 DEMONSTRATOR SCENARIO DESCRIPTION

The iPerf3 tool [25] is responsible for data traffic generation and throughput, and PER measurement of the PoC setup. We set up a server on the UE side and a client on the core network. The client sends packets at a desired throughput, and the server listens to those packets and calculates the network metrics. Figure 54 shows a snapshot of two servers and clients performing measurements. The highlighted areas are the measurements of interest.

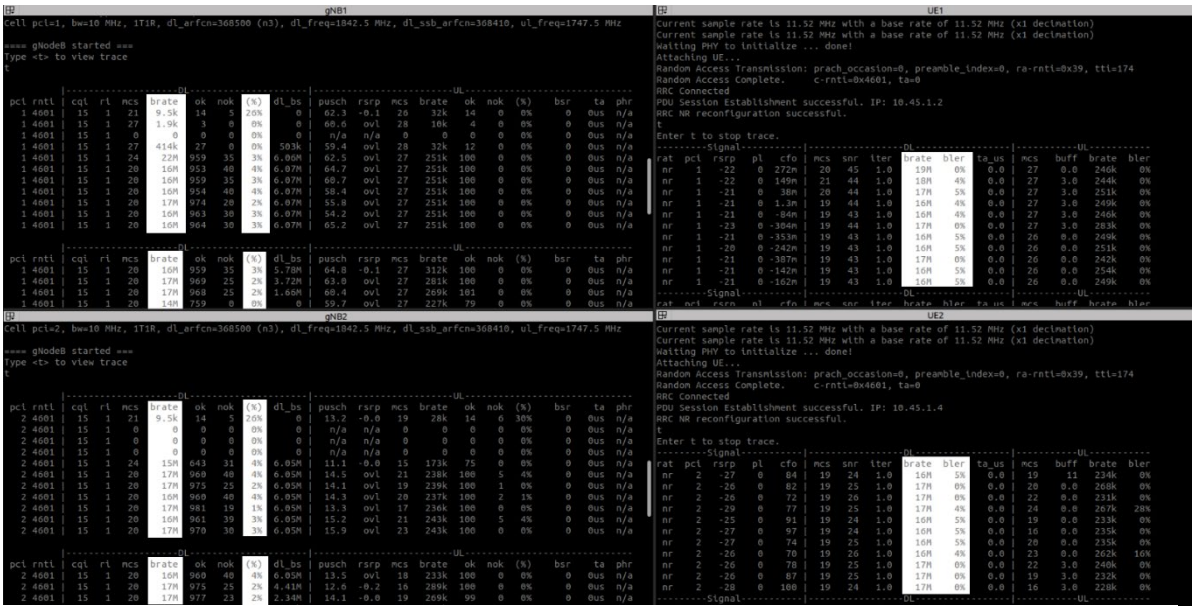

FIGURE 54. TWO PAIRS OF GNBS (LEFT) AND UES (RIGHT) REPORTED METRICS, THROUGHPUT AND PER HIGHLIGHTED.

The performance measurement process begins by starting the gNBs and synchronizing their timing roughly, so they refer to the same slot. Follows the UE's initiation, attaching each one to its corresponding gNB. After establishing all connections, we measure network performance using the specified tool. The desired throughput is the maximum theoretical throughput, around 45 Mbps.

Once the system stabilizes, we can export the metrics from the tool or the srsRAN software's metrics report. Additionally, the srsRAN software provides a real-time visualization of these metrics using the Grafana WebUI. Figure 55 presents a snapshot of the application's environment, showing graphs for downlink and uplink channels.

FIGURE 55. GRAFANA WEBUI DISPLAYING PLOTS OF DOWNLINK STATISTICS.

After completing the first set of measurements, we use them as a baseline. We then repeat the process, with the only difference being the start of the GNN node processes before starting the UE. This setup allows the new measurements to reflect the interference management of the developed implementation.

4.6.5 RESULTS

4.6.5.1 POC RESULTS VS THE BASELINE

In this section, measurement results of the proposed PoC are presented and compared with the bare metal setup where no power control is implemented for interference management. Ten setup scenarios were measured in total, each for different channel conditions of the two pairs. To set the desired channel condition, we observed the measured SNR reported from the srsRAN while slowly moving around each UE. To increase the SNR, we moved the UE closer to the serving cell, and to decrease it, we moved further away and closer to the interfering cell. The working range of SNRs was between 0 dB and 15 dB.

Figure 56 illustrates the network's rates when power control for interference management is applied and when both cells transmit equally with maximum power (Equal Power Allocation EPA). The network's rate is calculated as the Harmonic Mean of the individual SINRs reported by each pair. This choice ensures fairness in the network as lower rates influence more the final measure.

The measurements provide the following results and observations with respect to the experienced network data rate or throughput:

1. The proposed PoC for interference management outperforms the baseline by an average of 25% (with a range of 15-35%) across all scenarios.
2. Significant gain is displayed on channel conditions with low SINR.
3. As expected, the more unlike the conditions of the two pairs, the greater the gain, while with similar conditions, there is no benefit, as the best power control policy provides the Tx with equal power.

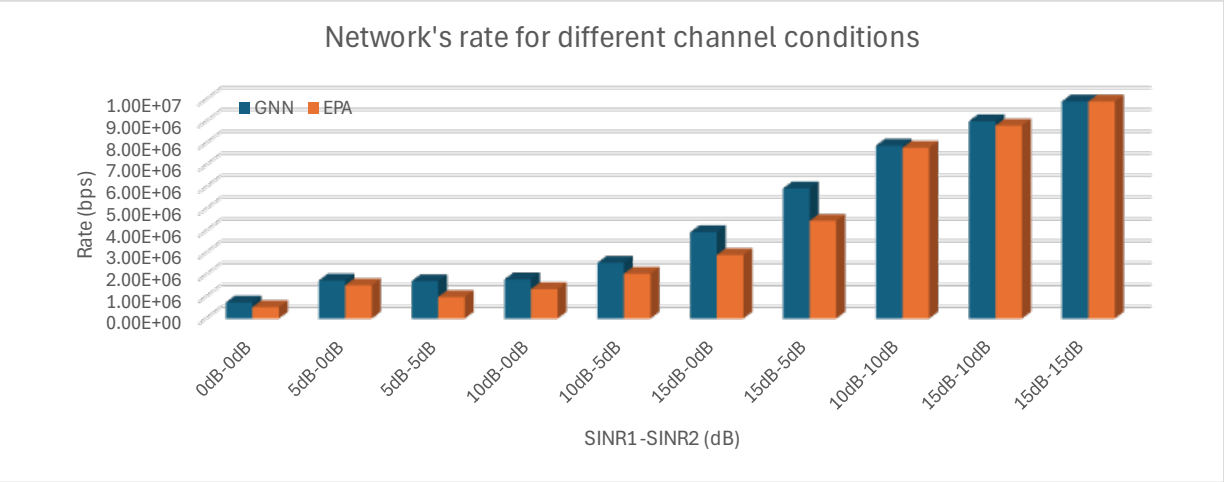

FIGURE 56. NETWORK THROUGHPUT AS THE HARMONIC MEAN OF THE RATES FOR DIFFERENT CHANNEL SCENARIOS.

4.6.5.2 MAPPING OF ACHIEVED RESULTS TO RELEVANT USECASE

A suitable use case for this PoC implementation is an Industrial Environment and specifically the “Subnetworks Swarms: Subnetwork Coexistence in Factory Hall” scenario as defined in deliverable D2.2. In this scenario multiple subnetworks operate wirelessly within the same factory hall, potentially sharing the same frequency bands and experiencing interference with one another. By applying a sophisticated power control policy, it is possible to minimize this interference and maximize the overall network's throughput.

4.6.5.3 CONCLUSION

Preliminary results and measurements of the implemented PoC display a significant improvement over baseline measurements. There is an average improvement of 25% of the network's throughput. For the moment, the results indicate a lack of performance gain at higher SINRs. This can be solved in two ways. One is to perform more aggressive power control when the channel conditions allow it. The other is to define more suitable parameters for dataset generation during the AI model's training phase. This way, the overall throughput could be improved, and the network's BLER could be minimized. Both proposed resolutions will be investigated and will be presented

in deliverable D5.3. Finally, it is known that the distributed power control solution based on GNN is applicable for a large number of subnetworks, and this is the objective of 6G-SHINE, that however are not possible to deploy with the existing infrastructure in our labs.

4.7 JAMMING DETECTION USING ANOMALY DETECTION METHODS (IDE)

4.7.1 GENERAL DESCRIPTION

This section provides details of the Jamming Detection using Anomaly Detection methods PoC, that is an extension of the work presented in [26]. In there, a framework topology was presented considering a jammer in a subnetwork, jamming the radio signal, and a compute topology within the parent network dealing with compute tasks required by the subnetwork. The result of the compute tasks is the objective and the end goal of the demonstration, without the presence of a jammer. Therefore, the Jamming Detection using Anomaly Detection methods PoC comprises anomaly detection methods that are used for a jamming event detection or determination, and subsequent subnetwork and compute management actions. These methods are integrated into a broader demonstration for a Collision Avoidance for Autonomous Vehicles use case.

Collision Avoidance use cases in the vehicular domain are supported by a variety of RF transmissions both within the vehicle and from/to the vehicle to its surroundings, i.e., intra-vehicle and inter-vehicle subnetworks. The transmissions can be both for the supporting of communications between vehicles, or for sensing related operations, e.g., radar functionality for obstacle on the road detection. They may involve one or more vehicles, as well as roadside infrastructure in place to support sensing functionalities.

Jamming of radio signals has negative consequences in both sensing and communication domains. If the jammed signal is being used for communications, traditionally affected KPIs include PER, throughput and latency. If used for sensing, affected KPIs include accuracy of position and velocity of e.g., a moving target detected via radar. The communications signal may also be used to carry sensing related data. In this case, if jamming on this signal occurs, both the sensing and communications will be affected as functionalities, and both sensing and communications KPIs will be negatively impacted. It is therefore fundamental to constantly monitor jamming events in such use cases, that cannot afford KPI degradation due their safety nature.

The scenario for the Collision Avoidance, illustrated in Figure 57, is about a robot autonomously operating in a Smart Factory. The robot is equipped with a mobile communication device and is remotely assisted by an application which obtains sensing results from an ISAC-enabled mobile network on any object on the factory floor. Based on the sensing results, the application can determine if the identified object is the robot or other objects the robot might collide with. If an object is identified as being on the robot's path, the application communicates with the robot on the factory floor via the mobile network to slow down or eventually stop the robot to avoid any collision.

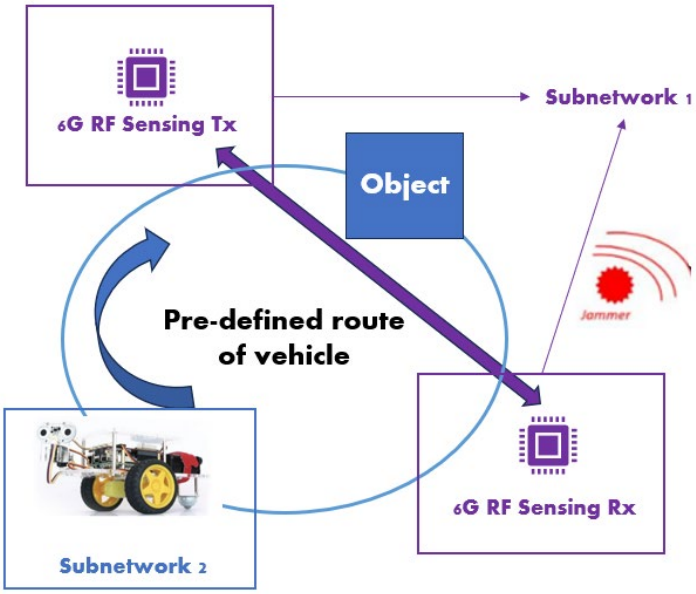

FIGURE 57. HIGH LEVEL COLLISION AVOIDANCE SCENARIO

In the figure, the blue circle represents a fixed circular path where the robot moves in the factory floor plan, and the blue arrow its direction of movement. A box "object" represents the obstacle that can be placed along the robot's path. In purple colour, there are two RF sensing capable nodes, one transmitter and one receiver. This means that the sensing transmitter will be emitting RF signals for the purpose of sensing and the sensing receiver will be in reception mode and capturing relevant sensing data for the obstacle detection. The sensing transmitter and receiver pair form one subnetwork in this setup, and the moving robot forms a second subnetwork. The jammer will be introduced as an element that degrades the signals transmitted within subnetwork 1.

4.7.2 ENHANCED/NEW FUNCTIONALITY

The parent 6G mobile network provides the RF Sensing Transmitter and a 6G RF Sensing Receiver as part of its radio deployment. An 802.11ad-compliant Single Carrier waveform and preamble is used as the Sensing Signal in the PoC, which operates in FR1. The Sensing Transmitter and Sensing Receiver are implemented on USRPs (N320) which provides a continuous stream of CIR measurements. These measurements are then placed on a messaging bus to be processed in a dedicated compute host outside the USRPs. This processing step is required to generate meaningful sensing related results (e.g., position/distance or velocity) starting from sensing raw data, collected from the antenna ports at the sensing receiver.

In this PoC, the messaging bus is the transport of raw sensing data resulting from the CIR at the sensing receiver in the subnetwork 1 and the output of the CIR processing is the relative distance and velocity between the identified objects and the sensing receiver. Figure 58 depicts an E2E flow for the generation of sensing results. The CIR at the sensing receiver is collected and aggregated, becoming raw sensing data, that is then transported to another location where compute resources are available via the messaging bus. At the compute resource location, this data can be transformed to extract the sensing results. The processing of the raw sensing data is implemented in hardware and represents an extension and enhancement of the emulated capabilities foreseen before and described in [26].

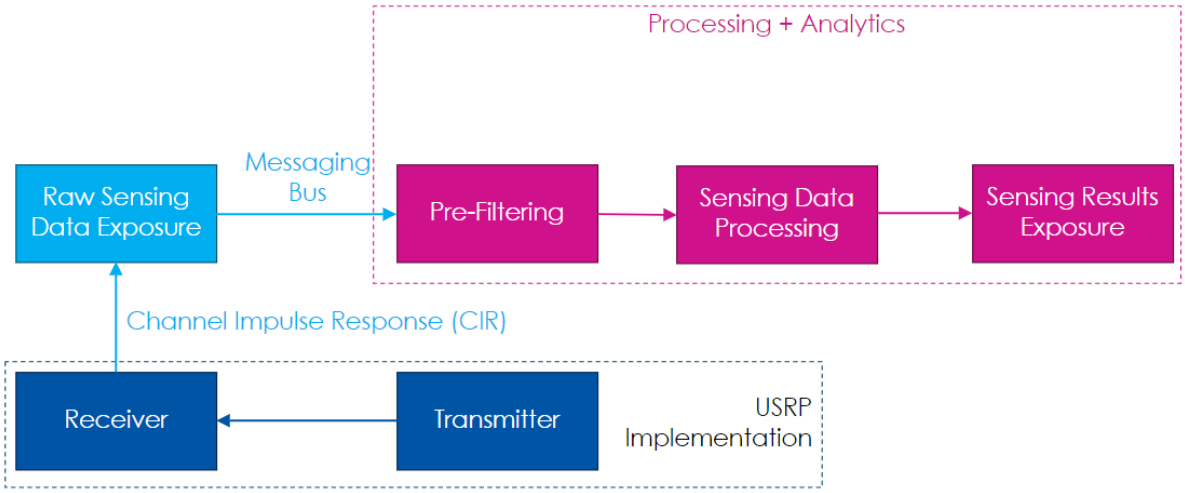

FIGURE 58. WORKFLOW JAMMING DETECTION USING ANOMALY DETECTION METHODS IN SENSING-ENABLED SUBNETWORKS

The jamming event determination via anomaly detection can be done in different ways. In the work carried out in WP4 [23,24], several options were presented for anomaly detection, including probabilistic, density, Kernel, ML and time series analysis, amongst others. One factor that is common across the presented methods is the computational complexity of the anomaly detection. Hence, piecewise functions have been introduced to represent an approximation of the response of the channel, so that computational complexity can be reduced, and the total delay of the anomaly detection can be therefore reduced. In sensing, when producing a result like a distance (or relative position between the receiver and the object/obstacle being sensed), LoS or NLoS condition of the radio link produces a significant degradation of the accuracy of that position. The NLoS condition represents a non-negligible decay of SNR at the receiver, and the sensing results are negatively impacted. It becomes therefore

straightforward that the anomaly detection can be executed utilizing these more complex methods applied to the CIR (or the raw sensing data), at the cost of the total delay for the anomaly detection or, by applying more simple methods (e.g., time series analysis) on the processed sensing results. While the former approach would allow for a faster detection of the anomaly, because it would be detected before the sensing result is generated, the latter is a better implementation option due to the need to constantly monitor the accuracy of the position and velocity measurements, i.e., the use cases linked with this PoC constantly require the usage of these results for further decision making and instructions to the actuators within the subnetworks, and therefore that part of the processing is required regardless of the presence of a jammer.

TABLE 10. SENSING RESULT KPIS FOR OBJECT DETECTION AND TRACKING (ADAPTED FROM [25])

Scenario	Confidence level [%]	Accuracy of positioning estimate by Sensing (for a target confidence level)		Accuracy of velocity estimate by Sensing (for a target confidence level)		Max Sensing service latency [ms]	Refreshing rate [s]	Missed detection [%]	False alarm [%]
		Horizontal [m]	Vertical [m]	Horizontal [m/s]	Vertical [m/s]				
Object detection and tracking	95	10	10	N/A	N/A	1000	1	5	2
	95	2	5	1	N/A	1000	0.2	0.1 to 5	5
	95	1	1	1	1	100, or 1000; 5000 for detection in highway	0.05 to 1	2	2
	99 for public safety, otherwise, 95	0.5	0.5	1.5 for pedestrian, 15 for vehicle, otherwise, 0.1	1.5 for pedestrian	100 to 5000	0.1	1	3

In Table 10. Sensing result KPIs for object detection and tracking (adapted from [25]), adapted from [25], KPIs for accuracy of position and velocity are presented, together with the respective confidence levels, missed detection and false alarm rates. The confidence level of each sensing result is therefore a direct estimate of the accuracy of position and velocity, and it is directly impacted by the presence of a jammer in or in the vicinity of the subnetwork, and its anomaly can be detected via distance and density methods [23].

Further, the max sensing service latency and refreshing rate represent the total delay for the transport of sensing data from the sensing receiver towards the compute node, and how often a sensing result needs to be generated from the raw sensing data, respectively. It is therefore straightforward that if the jammer impacts the communications link that serves as sensing data bus towards the compute node, both these KPIs will be impacted.

4.7.3 HIGH LEVEL ARCHITECTURE OF THE IMPLEMENTED POC DEMONSTRATOR

The high-level architecture of the jamming detection use case is illustrated in Figure 59 and depicts the Smart Factory floor with a robot (subnetwork 2) and the object, the Sensing Transmitter and Sensing Receivers (subnetwork 1), a Base Station the robot is connected to and a Sensing-Enabled 6G Core Network, implementing the coordination, storage and analytics of Sensing activities and the Sensing Data reported by the Sensing Receiver, respectively. The architecture also illustrates the application server consuming the Sensing Results and intervene with the autonomous operations of the robot when detecting a possible collision between the robot and an object.

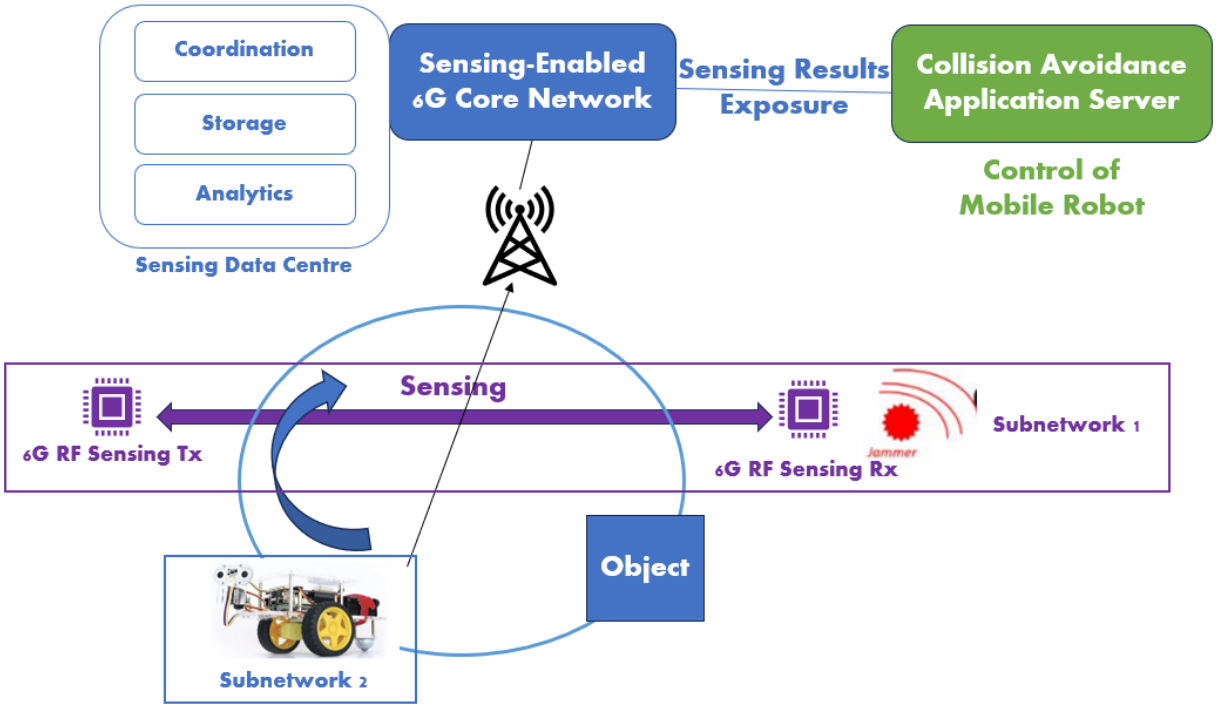

FIGURE 59. HIGH-LEVEL ARCHITECTURE OF THE JAMMING DETECTION USING ANOMALY DETECTION METHODS IN SENSING-ENABLED SUBNETWORKS POC

In addition to the RF sensing capabilities, the robot is equipped with a LiDaR sensor mounted at its front, providing distance measurements for object in front of it in the direction of travel. This sensor provides a maximum detectable distance of 3m with an accuracy of 0.1 cm. The figure depicts a jammer that can be seen as malicious or legitimate.

A full breakdown of all the components is as follows. Subnetworks 1 and 2 are both capable of sensing the object/obstacle. Subnetwork 1 uses a radio link for that purpose. Subnetwork 2 uses a LiDAR sensor and a radio link for communications towards the parent 6G network, via the Base Station. The collision avoidance application server receives sensing results from the Sensing enabled Core Network. This 6G CN has an in-built sensing data centre with a storage component for raw sensing data and for sensing results, an analytics component where processing of sensing data takes place, as well as the anomaly detection, and a coordination function capable of overseeing and coordinating the entire operation. This includes the management of the subnetworks, including the RRM functionalities, the participating node selection, participating subnetwork selection, and distributed compute coordination.

The selection of resources for computational efforts over the sensing data and the jamming detection over the sensing results is an important aspect, and the coordination component is capable of instantiating multiple compute resources for these purposes, e.g., in the case of the detection of an anomaly. The location of the compute resources can be within the subnetwork or the Core Network, and for this PoC, Core Network is chosen for simplicity purposes.

4.7.4 DEMONSTRATOR SCENARIO DESCRIPTION

The following step describe the demonstrator scenario. As an overall description, the subnetwork 1 is running and producing sensing data that is transmitted by the 6G RF Sensing receiver towards the Sensing data centre, where Sensing results are produced. This represents normal demonstrator operation. The jammer will then be then activated, resulting in a jamming detection event determination. As soon as this happens, decisions will be made to overcome the negative impact of the jammer, activating transmissions from subnetwork 2 towards the parent network, and instantiation of compute resources.

1) The 6G RF Sensing transmitter is configured to emit a sensing pilot signal towards the receiver

2) The 6G RF Sensing receiver is configured for the reception of the sensing pilot signal and convert the CIR into raw sensing data
3) The 6G RF Sensing receiver uses the communications link to the parent 6G network for the transmission of the sensing data
4) Sensing data centre stores and processes the sensing data, extracting meaningful results (position/velocity), and estimates delays and confidence levels
5) The jammer is activated by means of an attenuator on the communications channel between the sensing receiver and the Base Station
6) Sensing KPIs are being monitored in the sensing data centre and a sensing result KPI violation occurs
7) The coordination function in the sensing data centre requires the activation of the subnetwork 2, where the robot starts transport of LiDAR data via its communications link to the parent network
8) The coordination function instantiates new compute resources, to further process the incoming traffic from the subnetwork 2

4.7.5 RESULTS

4.7.5.1 BASELINE RESULTS

The processing of CIR requires the conversion into amplitudes over time, which is illustrated in Figure 60, and is based on the identification of the actual Sensing Signal. As the scenario is operating in a line-of-sight set-up of the Sensing Transmitter and Sensing Receiver, the strongest signal (highest amplitude) is identified first as the Sensing Signal itself. The reflections from objects are then lower amplitudes above the noise floor until the next Sensing Signal is measured. Knowing the sampling rate of the synchronized Sensing Transmitter and Sensing Receiver, the time between the high (Sensing Signal) and low (reflection) peak is the relative distance of an object to the Sensing Receiver.

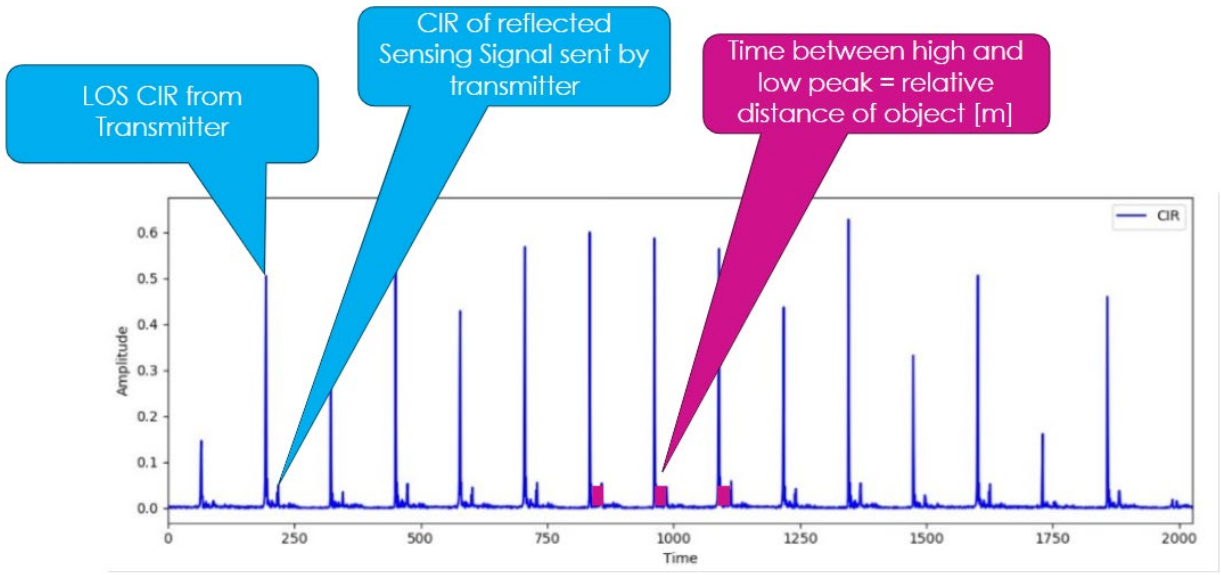

FIGURE 60. DETERMINATION OF RELATIVE DISTANCE USING CHANNEL IMPULSE RESPONSES

The process illustrated in the figure allows for the generation of the sensing results for position. Accuracies at the operating FR1 frequency band are around 50cm for estimated relative distances. This value is sufficient to meet the KPIs in Table 10. Sensing result KPIs for object detection and tracking (adapted from [25]), but it is borderline meeting the requirements for public safety use cases, as an example in the table. Therefore, the presence of a jammer might easily result in a degradation of the achieved results.

4.7.5.2 POC RESULTS VS THE BASELINE

To mitigate the presence of a jammer negatively affecting subnetwork 1, subnetwork 2 will transmit LiDAR data to the parent 6G network and its Sensing-enabled Core Network. Further results on the effect of the accuracy of position and velocity will be provided at a later stage, in Deliverable 5.3.

4.7.5.3 MAPPING OF ACHIEVED RESULTS TO RELEVANT USECASE

The PoC described has a very clear link and application to the automotive use cases. However, it is not exclusively useful for those. Industrial scenarios are good candidates as well for integration of the methods described in this section. As an example, the unit test cell use case [14] requires, for the factory production functionality, a set of RF sensors and a sensor aggregator. The sensor aggregator, as well as the AP (e.g., an HC node), are compute capable nodes that can be used for the processing and assessment of sensing related data. Hence, this use case also requires the assessment of sensing related KPIs to be performed after some rounds of processing. This is a fundamental step so that sensing data originated from sensing RF transmissions becomes something meaningful for the use case (e.g., a distance measured from the transmitter to the object being sensed in the unit test cell).

4.7.5.4 CONCLUSION

The presence of a jammer, malicious or legitimate, that produces an impact to the subnetwork operation are studied in this PoC. It is shown that anomaly detection methods presented in [23] can be used and the trade-off between their complexity and total anomaly detection delay should be addressed. The anomaly detection can be applied directly to the sensing result that needs to be generated constantly for the mentioned use cases, reducing its complexity and delay, at the cost of the impact of maximum sensing service latency or sensing result refresh rate KPIs. Another approach is to perform the jamming analysis directly to the sensing data, before converting it to a sensing result. This approach might incur in a different delay for jamming detection but would avoid the processing of the sensing data to convert it to a sensing result. The trade-off between the two approaches is a study that is planned for the next stage of this PoC, to be presented in Deliverable 5.3.

5 FINAL CONCLUSIONS

In this deliverable, we have presented our progress and initial results of the PoCs that are defined to be implemented in WP5 of 6G-SHINE. Specifically, we are targeting seven PoCs: Low latency channel emulator (addressing TC2), Latency aware MAC access (addressing TC11), Jamming resilient PHY (addressing TC6), Intra-subnetwork macro-diversity (addressing TC8), Centralized RRM (addressing TC13), Centralized/distributed interference management (address both TC12 and TC13), Jamming detection using anomaly detection (addressing TC15). For each PoC, we have presented the demonstrator scenario, a baseline which the PoC shall improve, a description of the PoC including its enhanced functionality and, if already present, preliminary results.

This deliverable reflects the work done in Task 5.2, where the initial implementation and evaluation of the PoCs is performed. Final implementation will continue in Task 5.3, and performance will be verified against the identified baseline KPIs. During this process the development of the PoCs may provide feedback for WP2-3-4. The work in Task 5.3 will be reported in deliverable D5.3, due by August 2025, which will include the full description of the developed PoCs and final results of the achieved performance enhancement.

REFERENCES:

[1] https://www.xilinx.com/products/boards-and-kits/ek-u1-zcu102-g.html
[2] ETSI EN 300 328 - V2.2.2 - Wideband transmission systems, https://www.etsi.org/deliver/etsi_en/300300_300399/300328/02.02.02_60/en_300328v020202p.pdf
[3] 6G-Shine D3.1 deliverable - Preliminary results on PHY and MAC enablers for IN-X subnetworks, https://6gshine.eu/wp-content/uploads/2024/11/D3.1-Preliminary-results-on-PHY-and-MAC-enablers-for-in-X-subnetworks_v1.0.pdf
[4] Ns-3 network simulator, https://www.nsnam.org/
[5] 6G-Shine D2.2 deliverable - Refined definition of scenarios, use cases and service requirements for in- X subnetworks, https://6gshine.eu/wp-content/uploads/2024/11/D2.2-Refined-definition-of-scenarios-use-cases-and-service-requirements-for-in-X-subnetworks-_v1.0.pdf
[6] https://www.analog.com/en/resources/evaluation-hardware-and-software/evaluation-boards-kits/eval-ad-fmcomms2.html
[7] https://www.intel.com/content/www/us/en/products/sku/189347/intel-wifi-6-ax200-gig/specifications.html
[8] https://www.nrl.navy.mil/Our-Work/Areas-of-Research/Information-Technology/NCS/MGEN/
[9] https://github.com/open-sdr/openwifi
[10] OpenWRT. "Welcome to the OpenWRT Project." Accessed October 28, 2024. https://openwrt.org/
[11] X. Lin, L. Kundu, C. Dick and S. Velayutham, "Embracing AI in 5G-Advanced Toward 6G: A Joint 3GPP and O-RAN Perspective," in *IEEE Communications Standards Magazine.*
[12] D. Bankov, E. Khorov, A. Lyakhov and M. Sandal, "Enabling Low Latency Communications in Wi-Fi Networks," *2018 IEEE 29th Annual International Symposium on Personal, Indoor and Mobile Radio Communications (PIMRC).*
[13] M. T. Lemes, A. M. Alberti, C. B. Both, A. C. De Oliveira Júnior and K. V. Cardoso, "A Tutorial on Trusted and Untrusted Non-3GPP Accesses in 5G Systems—First Steps Toward a Unified Communications Infrastructure," in *IEEE Access.*
[14] IEEE Standard for Information technology--Telecommunications and information exchange between systems Local and metropolitan area networks--Specific requirements Part 11: Wireless LAN Medium Access Control (MAC) and Physical Layer (PHY) Specifications," in *IEEE Std 802.11-2012 (Revision of IEEE Std 802.11-2007).*
[15] Bui, Van-Phuc, Daniel Abode, Pedro M. Ana, Karthik Muthineni, Shashi Raj Pandey, and Petar Popovski. "Digital Twin of Industrial Networked Control System based on Value of Information." *arXiv preprint arXiv:2404.14960* (2024).
[16] NXP Semiconductors. "Creating the 360-Degree Vehicle: Understanding Cocoon Radar Technology." Smarter World Blog. Accessed October 28, 2024. https://www.nxp.com/company/about-nxp/smarter-world-blog/BL-CREATING-THE-360-DEGREE-VEHICLE.
[17] Wireshark Foundation. "Wireshark Network Protocol Analyzer." Accessed October 28, 2024. https://www.wireshark.org/
[18] 6G SHINE D2.2. Refined definition of scenarios, use cases and service requirements for in- X subnetworks.
[19] USRP B210 USB Software Defined Radio (SDR), Ettus Research. Available at: https://www.ettus.com/all-products/ub210-kit/ (Accessed: 11 November 2024).
[20] srsRAN project. Available at: https://www.srsran.com/ (Accessed: 11 November 2024).
[21] Y. Gu, C. She, Z. Quan, C. Qiu and X. Xu, "Graph Neural Networks for Distributed Power Allocation in Wireless Networks: Aggregation Over-the-Air," in IEEE Transactions on Wireless Communications, vol. 22, no. 11, pp. 7551-7564, Nov. 2023, doi: 10.1109/TWC.2023.3253126.
[22] PyTorch. Available at: https://pytorch.org/ (Accessed: 11 November 2024).
[23] ZeroMQ. Available at: https://zeromq.org/ (Accessed: 11 November 2024
[24] 3GPP, "NR; Physical Channels and Modulation (Release 17)," 3rd Generation Partnership Project (3GPP), TS 38.211.
[25] iPerf3. Available at: https://iperf.fr/ (Accessed: 11 November 2024).
[26] "5G; Study on channel model for frequencies from 0.5 to 100 GHz," European Telecommunications Standards Institute, Technical Report 38.901, v18.0.0 2024. Available: https://www.etsi.org/.

[27] 6G SHINE D4.1. Preliminary results on the management of radio resources in subnetworks in the presence of legitimate and malicious interferers
[28] 6G SHINE D4.2. Preliminary results on the management of traffic, computational and spectrum resources among subnetworks in the same entity, and between subnetworks and 6G network
[29] 3GPP TS 22.137, "Service requirements for Integrated Sensing and Communication; Stage 1; (Release 19)," 3GPP, Mar. 2024.
[30] 6G SHINE D5.1. Description and methodology of evaluation of initial PoCs
[31] Erceg, V., L. Schumacher, P. Kyritsi, et al. TGn Channel Models. Version 4. IEEE 802.11-03/940r4, May 2004.